Pacific Northwest
NATIONAL LABORATORY

PNNL-32519 Rev. 1

Drones for Decommissioning

Proof-of-Concept

July 2022

Amoret Bunn
Katie Wagner
Deb Fagan
Harish Gadey
Tracy Ikenberry
Kameron Markham
Moses Obiri

Prepared for the U.S. Nuclear Regulatory Commission
Office of Nuclear Regulatory Research
Under Contract DE-AC05-76RL01830
Interagency Agreement: 31310019N0001
Task Order 31310019F0011

DISCLAIMER

This report was prepared as an account of work sponsored by an agency of the United States Government. Neither the United States Government nor any agency thereof, nor Battelle Memorial Institute, nor any of their employees, makes **any warranty, express or implied, or assumes any legal liability or responsibility for the accuracy, completeness, or usefulness of any information, apparatus, product, or process disclosed, or represents that its use would not infringe privately owned rights**. Reference herein to any specific commercial product, process, or service by trade name, trademark, manufacturer, or otherwise does not necessarily constitute or imply its endorsement, recommendation, or favoring by the United States Government or any agency thereof, or Battelle Memorial Institute. The views and opinions of authors expressed herein do not necessarily state or reflect those of the United States Government or any agency thereof.

PACIFIC NORTHWEST NATIONAL LABORATORY
operated by
BATTELLE
for the
UNITED STATES DEPARTMENT OF ENERGY
under Contract DE-AC05-76RL01830

Printed in the United States of America

Available to DOE and DOE contractors from the
Office of Scientific and Technical Information,
P.O. Box 62, Oak Ridge, TN 37831-0062;
ph: (865) 576-8401
fax: (865) 576-5728
email: reports@adonis.osti.gov

Available to the public from the National Technical Information Service
5301 Shawnee Rd., Alexandria, VA 22312
ph: (800) 553-NTIS (6847)
email: orders@ntis.gov <https://www.ntis.gov/about>
Online ordering: http://www.ntis.gov

Drones for Decommissioning

Proof-of-Concept

July 2022

Amoret Bunn
Katie Wagner
Deb Fagan
Harish Gadey
Tracy Ikenberry
Kameron Markham
Moses Obiri

Prepared for the U.S. Nuclear Regulatory Commission
Office of Nuclear Regulatory Research
Under Contract DE-AC05-76RL01830
Interagency Agreement: 31310019N0001
Task Order: 31310019F0011

Pacific Northwest National Laboratory
Richland, Washington 99354

Summary

The U.S. Nuclear Regulatory Commission has responsibility for regulating the safe decommissioning of facilities and sites to meet the License Termination Rule in Title 10 Code of Federal Regulations (CFR) Part 20, *Standards for Protection Against Radiation,* Subpart E "Radiological Criteria for License Termination." Decommissioning is performed in accordance with 10 CFR Part 50, *Domestic Licensing of Production and Utilization Facilities*, as part of license termination (§50.82) and release of the facility or site for unrestricted use (§50.83). The guidance currently demonstrates the minimum requirements and necessary conditions for conducting radiological surveys by a person carrying a radiation detector(s).

The Pacific Northwest National Laboratory (PNNL) evaluated the use of an unoccupied aerial vehicle (UAV) to conduct radiological surveys that could be used in decommissioning to reduce time, cost, and potential safety risks to humans compared to current survey methods. The objective of this project was to evaluate the performance and limitations of a UAV to support a decommissioning radiological survey and compare it to a radiological survey conducted by a human.

The primary research questions of interest evaluated were:

- Did observed UAV paths differ from human paths and, if so, by how much?
- Did survey path deviation affect survey results and, if so, how?
- Were radiological measurements from human and UAV surveys significantly different?

To answer these research questions, an experimental field was set up at PNNL's 3440 test track, and it included radiological sources commonly surveyed during decommissioning: cobalt-60 (Co-60), cesium-137 (Cs-137), and americium-241 (Am-241). Nine check sources (three each of Am-241, Cs-137, and Co-60) with activities ranging from 3.54 µCi to 39.34 µCi were set over a path that also included an area for measuring background radiation. An Aurelia X6 UAV coupled with a GPS and lidar unit was used to conduct the radiological surveys. UAV and human surveys were conducted using two different NaI(Tl) scintillation radiation detectors ([1] 2 in. × 2 in. Ludlum, Inc. and [2] 2 in. × 0.04 in. Alpha Spectra, Inc.) at a travel velocity of approximately 0.2 m/s at a low (15–40 cm median altitude) or high (87–105 cm median altitude) survey altitude. Since the survey velocity and altitude parameters were atypical for normal UAV operations, testing was done prior to conducting the radiological surveys to establish airworthiness, evaluate the navigation system, and establish flight control. Human and UAV surveys were paired according to the detector type and altitude regime to compare the survey data.

The results of this proof-of-concept research determined that the UAV and human surveys followed similar survey paths and detected the radiological sources with no significant statistical difference (in 33 out of 36 surveys). However, further research is needed prior to deploying UAVs for decommissioning surveys.

Acronyms and Abbreviations

Am-241	americium-241
CDF	cumulative distribution function
CFR	U.S. Code of Federal Regulations
Co-60	cobalt-60
cpm	counts per minute
CPMR	count-rate-to-exposure-rate ratio
Cs-137	cesium-137
CZT	cadmium (Cd) zinc (Zn) telluride (Te) semiconductor
DCGL	derived concentration guidance level
eCDF	empirical cumulative distribution function
ERC	exposure-rate-to-concentration ratio
FAA	Federal Aviation Administration
H-3	tritium
HPGe	high purity germanium (radiation detector)
kcpm	one thousand cpm
keV	one thousand electron volts
K-S	Kolmogorov-Smirnov (statistical test)
MDC	minimum detectable concentration
MDCR	minimum detectable count rate
NaI(Tl)	sodium (Na) iodide (I) thallium (Tl)-drifted
NRC	United States Nuclear Regulatory Commission
PMT	photomultiplier tube
PNNL	Pacific Northwest National Laboratory
SME	subject matter expert
Sr-90	strontium-90
Tl	thallium
UAS	unoccupied aerial system
UAV	unoccupied aerial vehicle
V	volts

Contents

Summary iii
Acronyms and Abbreviations iv
1.0 Introduction 1
2.0 Experimental Design 3
2.1 Radiation Detector and Data Logger 3
2.2 Radionuclides of Interest 5
2.2.1 Derived Concentration Guideline Limits 6
2.2.2 Minimum Detectable Concentration 6
2.3 Unoccupied Aerial Vehicle and Field Survey Cart 11
2.3.1 Unoccupied Aerial Vehicle and Payload 11
2.3.2 Field Survey Cart 13
2.3.3 Testing of the UAV for Airworthiness 13
2.4 Field Study 14
2.4.1 Field Setup 15
2.4.2 Radiological Survey Scenarios 16
2.5 Data Analysis Methods 18
2.5.1 Data Processing 19
2.5.2 Statistical Analysis Methods 25
3.0 Results 30
3.1 Comparison of Survey Paths by UAV and Human 30
3.2 Comparison of Radiological Measurement Data 33
3.2.1 Scenario 1 – Ludlum Detector at Low Survey Altitude (Survey 9 and 10) 33
3.2.2 Scenario 2 – Alpha Spectra Detector at Low Survey Altitude (Survey 11 and 6) 33
3.2.3 Scenario 3 – Ludlum Detector at High Survey Altitude (Survey 1 and 2) 33
3.2.4 Scenario 4 – Alpha Spectra Detector at High Survey Altitude (Survey 12 and 4) 34
4.0 Discussion 39
5.0 Conclusion and Recommendations 43
6.0 References 46
Appendix A – Radiation Detector Evaluation A.1
Appendix B – Activity of Radioactive Point Sources B.1
Appendix C – Radionuclide Exposure Rate-to-Concentration Ratios C.1
Appendix D – Background Measurements and Calculations D.1
Appendix E – Statistical Results E.1
Appendix F – List of Project Staff F.1

Figures

Figure 1. Setting Up the Aurelia X6 UAV 11
Figure 2. Rendering of the 3D Casing Used to Mount the Payload on the UAV 12
Figure 3. Aurelia X6 in Flight and with Payload 12
Figure 4. Modified Cart Used to Conduct Radiological Surveys by a Human 13
Figure 5. PNNL's 3440 Test Track Used for UAV and Human Radiological Surveys 14
Figure 6. Radiological Survey Field Setup at PNNL's 3440 Test Track 15
Figure 7. Spatial Data of Survey Paths for Surveys 1 (UAV, Ludlum, High) and 2 (Human, Ludlum, High) 21
Figure 8. Surveys 1 (UAV, Ludlum, High) and 2 (Human, Ludlum, High) Over the Source Transects 22
Figure 9. Observed Radiation Measurements for Survey 1 (UAV, Ludlum, High) and Survey 2 (Human, Ludlum, High) as a Function of Elapsed Time 23
Figure 10. Raw Lidar (Altitude) Data for the Source Transect from Survey 3 (UAV, Ludlum, High) is Illustrated 24
Figure 11. Check Source Locations by Longitude and Latitude in Meters, along with a Regression Line 25
Figure 12. UAV (Blue Line) and Human (Orange Line) Regression Lines for Surveys 1 (UAV, Ludlum, High) and 2 (Human, Ludlum, High) 26
Figure 13. Example of Count Rate vs. Time Elapsed for UAV Survey 9 (UAV, Ludlum, Low) and Human Survey 10 (Human, Ludlum, Low) 27
Figure 14. Empirical Cumulative Distribution Functions (eCDFs) of the Data Collected in Surveys 1 (Ludlum, UAV, High) and 2 (Ludlum, Human, High) Over Check Source 4 29
Figure 15. Position Data, with Corrected Offset, for Surveys 1 and 2 (left), and Surveys 9 and 10 (right) 31
Figure 16. The Lateral Distance (in Meters) of the Detector to the Location of a Check Source for a) Surveys 1 and 2, and b) Surveys 9 and 10 32
Figure 17. Comparison of Counts Rates for Scenario 2, the Alpha Spectra Radiological Detector for Surveys 6 (human) and Survey 11 (UAV), with Check Source 9 Highlighted in Red Box to Emphasize the Significant Difference in Results 40
Figure 18. Empirical Cumulative Distribution Functions (eCDFs) for the Two-Sample K-S Test Showing a Significant Difference in Values (p = 0.00002) for Human (Survey 4) and UAV (Survey 12) Radiological Count Rate at Check Source 4 41
Figure 19. Empirical Cumulative Distribution Functions (eCDFs) for the Two-Sample K-S Test Showing a Significant Difference in Values (p = 0.0008) for Human (Survey 4) and UAV (Survey 12) Radiological Count Rate at Check Source 5 41
Figure 20. Empirical Cumulative Distribution Functions (eCDFs) for the Two-Sample K-S Test showing the Similarity (p = 0.2030) for Human (Survey 4) and UAV (Survey 12) Radiological Count Rate at Check Source 8 42

Tables

Table 1. Sample of the Data Obtained from the Ludlum 3000 Data Logger 4
Table 2. Detector Response for the Am-241 and Co-60 Disk Sources 4
Table 3. Radionuclides of Interest for this Study 5
Table 4. Common Radionuclides at Decommissioned Sites Used for Selecting Isotopes for This Study 5
Table 5. CPMR Values Used for Am-241, Cs-137, and Co-60 7
Table 6. ERC Data Computed in Microshield™ for Radionuclides of Interest as a Function of Height 8
Table 7. Calculated MDC for Each Radionuclide of Interest as a Function of Detector Height 9
Table 8. Theoretical Check Source Activities Required to Collect the Minimum Gross Count Rate to Meet Project Objectives 11
Table 9. Layout of Check Sources and Associated Activity along the Survey Transect 15
Table 10. Radiological Survey Experimental Design 16
Table 11. Altitude and Velocity for Analyzed Surveys 17
Table 12. Summary of Regression Information Comparing the UAV and Human Surveys 30
Table 13. Latitude and Longitude for Each Radiological Source Location 33
Table 14. Scenario 1 Radiological Activity (kcpm) and Statistical Comparison for the Ludlum Detector at a Low Survey Altitude by Check Source and Surveyor 35
Table 15. Scenario 2 Radiological Activity (kcpm) and Statistical Results for the Alpha Spectra Detector at a Low Survey Altitude by Check Source and Surveyor 36
Table 16. Scenario 3 Radiological Activity (kcpm) and Statistical Results for the Ludlum Detector at a High Survey Altitude by Check Source and Surveyor 37
Table 17. Scenario 4 Radiological Activity (kcpm) and Statistical Results for the Alpha Spectra Detector at a High Survey Altitude by Check Source and Surveyor 38

1.0 Introduction

The U.S. Nuclear Regulatory Commission (NRC) has responsibility for regulating the safe decommissioning of facilities and sites to meet the License Termination Rule in Title 10 Code of Federal Regulations (CFR) Part 20, *Standards for Protection Against Radiation,* Subpart E, "Radiological Criteria for License Termination." Decommissioning is performed in accordance with 10 CFR Part 50, *Domestic Licensing of Production and Utilization Facilities*, as part of termination of license (§50.82) and release of the facility or site for unrestricted use (§50.83). Key guidance for demonstrating a facility or site meets these regulations—including radiological surveys—is provided in NUREG-1507, Revision 1, *Minimum Detectable Concentrations with Typical Survey for Instruments for Various Contaminants and Field Conditions* (Abelquist et al. 2020), NUREG-1575, Revision 1, *Multi-Agency Radiation Survey and Site Investigation Manual (MARSSIM)* (NRC 2000), and NUREG-1757, *Consolidated Decommissioning Guidance* (Banovac et al. 2006; Barr et al. 2020). The guidance currently demonstrates the minimum requirements and necessary conditions for conducting radiological surveys by a person carrying a radiation detector(s).

In the past few years, significant effort has been put into studying the use of unoccupied aerial vehicles (UAVs) in the nuclear industry. There are prototype unoccupied aerial systems (UASs) with gross count radiological detectors (e.g., NaI) as well as with gamma-spectrometers for many types of evaluations but not necessarily for detecting low levels of radiation necessary for a decommissioning plan (Lee and Kim 2019). UAVs equipped with radiological detection systems are currently being used to evaluate radiation for incident response and cleanup. In addition, this technology is being used in various capacities for developing contamination maps at legacy uranium sites, monitoring and detection of radiation leaks, visual inspections at nuclear facilities, unsupervised radiological measurements, high-accuracy 3D mapping using lidar in conjunction with radiation detection, and to assess the condition of the Fukushima Daiichi nuclear power plant. It is worth mentioning that the area of low-level radiation monitoring for decommissioning purposes has not been extensively explored and none of the NRC guidance explicitly considers the use of UAVs for decommissioning and radiological surveys.

Decommissioning surveys target a range of radionuclides of concern, depending on site missions (e.g., Aker and Wood 2005, McGrath 2007, Battelle 2002, Entergy 2014, Yankee Atomic Electric Co. 2004, CYAPCO 2006). Radionuclides include beta emitters and gamma emitters; however, cobalt-60 (Co-60), cesium-137 (Cs-137), americium-241 (Am-241), strontium-90 (Sr-90), and tritium (H-3) have been shown to be some of the most commonly surveyed radionuclides during decommissioning (O'Malley and Bunn 2021). Gamma-emitting radionuclides are most suitable for surveys because the photon energies can be detected without performing any chemical analysis (soil sample studies). Conversely, radionuclides emitting only an alpha or beta particles would require sampling and additional lab analysis. UAVs are expected to be most effective for surveys of gamma-emitting radionuclides because of their ability to fly low and slow without coming in contact with the ground, thereby increasing detection sensitivity.

The Pacific Northwest National Laboratory (PNNL) evaluated the use of a UAV to conduct a radiological survey that could be used in decommissioning. The objective of this project was to evaluate the performance and limitations of a UAV to support a decommissioning radiological survey and compare it to a radiological survey conducted by a human. This work has the potential to benefit decommissioning planners, licensees, and the regulatory community as the use of UAVs in decommissioning surveys has the potential to reduce time, cost, and potential

safety risks to humans, and to survey areas that are inaccessible or difficult to access by typical survey methods.

This report is organized as follows:

- Section 2.0 provides an overview of the experimental design used for evaluating the feasibility of using a UAV for decommissioning surveys for unrestricted use.
- Section 3.0 presents the results of the feasibility study.
- Section 4.0 briefly discusses the results.
- Section 5.0 briefly discusses the conclusions of the study and next steps.
- Section 6.0 lists references to supporting documents.
- Appendix A discusses and evaluates the use of various detector options for the study.
- Appendix A discusses radionuclides of interest and calculates the derived concentration guideline limits and point source activity.
- Appendix C discusses and presents the exposure rate-to-concentration ratios for the radionuclides of interest.
- Appendix D discusses the background radiation calculations.
- Appendix E presents figures from data analysis.

2.0 Experimental Design

This section describes the characteristics of the surveys performed. Section 2.1 covers the activity calculations that are key to selecting the radiological detector for the surveys. Section 2.2 includes the radionuclides of interest. Section 2.3 discusses the survey systems: UAV and the control survey system (a human pushing a cart with the survey instrument). The characteristics of the field study are included in Section 2.4. Finally, Section 2.5 provides an overview of the data analysis for the surveys.

2.1 Radiation Detector and Data Logger

Several radiation detector options were considered and evaluated for this work (Appendix A). Based on this evaluation, a scintillation media was selected because of its response time, detection efficiency, robustness, weight, and size compared to gas- or semiconductor-based systems.

In the class of scintillation technologies, sodium iodine (NaI) doped (activated) with thallium (Tl), or NaI(Tl) (herein referred to as NaI), was chosen because of its ease of use, availability in relatively large sizes, and extensive technical expertise in the research and development community. NaI scintillation detectors are commonly used for outdoor scans (Abelquist 2014). Two NaI detectors were chosen for this application:

- Ludlum, Model 44-10 Gamma Detector, 2 in. diameter × 2 in. thickness NaI(Tl) scintillation crystal coupled with a photomultiplier tube (PMT) was used for detecting high energy photons (e.g., Cs-137, and Co-60) (Ludlum Measurements, Inc., Sweetwater, Texas; https://ludlums.com/products/health-physics/product/model-44-10).
- Alpha Spectra, Model 8TI040A1/2B (9266) Thin-Open Face Gamma Detector, 2 in. diameter × 0.04 in. thickness NaI(Tl) scintillation crystal coupled with a PMT was used for detecting the low energy gamma photons (e.g., Am-241) (Alpha Spectra, Inc., Grand Junction, Colorado; https://alphaspectra.com/products/thin-window/).

Two different detectors were used in order to maximize the detection efficiency over a broad photon energy range. The 2 in. × 0.04 in. scintillator has a relatively high detection efficiency for the low energy 59 keV photons emitted by Am-241; this scintillator is unable to achieve a high detection efficiency for Cs-137 and Co-60 because of its low interaction cross section. The 2 in. × 2 in. scintillator is best suited to detect the high energy photons emitted by Cs-137 and Co-60. The window at the end of the 2 in. × 2 in. detector attenuates the low energy photons significantly, resulting in low photon interactions with the scintillator volume.

The Ludlum and Alpha Spectra radiation detectors were connected to the modified custom built Ludlum data logger for collecting detector response (counts per minute) in one second intervals (Ludlum Model 3000 Digital Survey Meter; Ludlum Measurements, Inc., Sweetwater, Texas; https://ludlums.com/products/all-products/product/model-3000). A custom modification by the manufacturer was made to accommodate a flash storage drive to accumulate data files that represent several hours of operation as opposed to less the stock system that can store approximately 30 minutes of data collection (at one record per second). This storage drive converts into a USB device when needed to facilitate data transfer from the data logger to the laptop/PC in the form of a text file. The data collected is presented in the form of a timestamp and corresponding cpm in one second intervals. Table 1 shows a snippet of the data collected

from the Ludlum data logger while the radiological detector was stationary at PNNL's 3440 test track. The data logger usually scales the counts to cpm based on data collected each second.

Calibration of these radiation detectors was performed using the Lumic calibration kit provided by Ludlum. A radiological source was placed in contact with the end of the probe and the software recorded the counts per second data as a function of voltage, resulting in the generation of a plateau curve that assisted in selecting the operating voltage. This test was conducted using both the Ludlum (Co-60) and Alpha Spectra (Am-241) detectors. Based on the results, a voltage of 1050 V with a threshold of 30 mV (one thousandth of a volt) for operation of both detectors was selected since the maximum efficiency was obtained at these operating parameters and used for all experimental surveys. Since the Ludlum data logger can accept only a single input, it was required to fly two independent routes for each height and velocity to capture the response from both detectors.

Table 1. Sample of the Data Obtained from the Ludlum 3000 Data Logger

Date	Time	Counts (kcpm)
2021/11/13	18:03:59.426	1.09
2021/11/13	18:04:00.247	1.09
2021/11/13	18:04:01.247	1.08
2021/11/13	18:04:02.247	1.08
2021/11/13	18:04:03.247	1.17
2021/11/13	18:04:04.247	1.17
2021/11/13	18:04:05.247	1.31

After calibration and setting the voltage for each detector, an investigation was performed to study the differences in response between the Ludlum and Alpha Spectra detectors when exposed to Am-241 and Co-60. Table 2 shows the radiological properties of the source and the response from the detectors. These measurements were carried out with the source in contact with the detector surface (on contact measurements).

Table 2. Detector Response for the Am-241 and Co-60 Disk Sources

Radionuclide	Initial Activity (µCi)	Half-life (y)	Corrected Activity (µCi)	Detector	Counts (kcpm)
Am-241	6.2	432.2	5.87	Ludlum	~290
Am-241	6.2	432.2	5.87	Alpha Spectra	~725
Co-60	9.982	5.3	1.422	Ludlum	~610
Co-60	9.982	5.3	1.422	Alpha Spectra	~170

The Ludlum 2 in. × 2 in. NaI detector is better equipped to detect high energy photons (e.g., from Co-60 or Cs-137 sources) because of its higher count rate compared to the 2 in. × 0.04 in. Alpha Spectra detector. The Alpha Spectra 2 in. × 0.04 in. has a higher sensitivity and is suitable for the detection of low energy gamma photons (e.g., from an Am-241 source) compared to the 2 in. × 2 in. Ludlum detector.

2.2 Radionuclides of Interest

For this research, the radionuclides of interest were limited to prominent photon emitters, specifically Am-241, Cs-137, and Co-60 (Table 3). These sources were selected because they are predominantly found in decommission sites (Table 4) and represent a wide range of energies from 60 keV to 1.3 MeV (Wood 1998; Battelle 2002; Yankee Atomic Electric Co. 2004; Aker and Wood 2005; CYAPCO 2006; McGrath 2006; Entergy 2014). The broad term of decommissioning surveys can be conducted at several types of facilities or sites, including refining, enrichment, fuel fabrication, nuclear reactor, and spent fuel facilities and sites. Strontium-90 (Sr-90) was initially considered for this work; however, as discussed in Appendix A, the dose rates at agricultural resident derived concentration guideline limit (DCGL) levels for Sr-90 were found to be about 1,000 times lower than other photon sources considered in this work, and thus would be indistinguishable from detector background. Tritium (H-3) was also considered but differences in decay mode (beta) and the detection technology used compared to other radionuclides of interest resulted in excluding H-3 from this study. Sr-90 (beta) and H-3 (beta) activities are generally hard to detect and are measured in a laboratory or estimated based on surrogate relationship with other radionuclides rather than being evaluated using field measurement devices.

Table 3. Radionuclides of Interest for this Study

Radionuclide	Half-life (years)	Radiation Type	Yield (%)	Energy (keV)
Am-241	432.2	Gamma	35.9	59
Cs-137	30.1	Gamma	85.1	662
Co-60	5.3	Gamma	99.97	1173
			99.99	1332

Table 4. Common Radionuclides at Decommissioned Sites Used for Selecting Isotopes for This Study

Site	Radionuclides Evaluated [a]	Reference
Yankee Rowe Decommissioning	Co-60, Ag-108m, Cs-137	Wood 1998
Yankee Nuclear Plant Historical Site Assessment	H-3, C-14, Fe-55, Co-60, Ni-63, Sr-90, Nb-94, Tc-99, Ag-108m, Sb-125, Cs-134, Cs-137, Eu-152, Eu-155, Pu-238, Pu-239, 240, Am-241, Pu-241, Cm-243, Cm-244	Yankee Atomic Electric Co. 2004
Maine Yankee Decommissioning	Fe-55, Co-60, Ni-63, Sb-125, Cs-137	Aker and Wood, 2005
Connecticut Yankee Decommissioning	H-3, Co-60, Sr-90, Cs-137, Am-241	McGrath 2006
Connecticut Yankee Final Status Survey	Co-60, Ni-63, Cs-137	CYAPCO 2006
Vermont Yankee Radiological Historical Site Assessment	H-3, Mn-54, Fe-55, Co-60, Zn-65, Sr-90, Cs-134, Cs-137	Entergy 2014
West Jefferson North Facility	Co-60, Sr-90, Sb-125, Cs-134, Cs-137, Eu-154, U-234, Np-237, Pu-238, U-238, Pu-239/240, Am-241, Cm-244	Battelle 2002

[a] Highlights added to emphasize radionuclides common to all or most of the decommissioned sites.

2.2.1 Derived Concentration Guideline Limits

DCGLs are radionuclide specific values that are calculated to establish a relation between the residual radioactivity in an area to the regulatory limit or risk criteria. In this work, DCGLs are calculated considering the License Termination Rule dose criterion of 25 mrem/year above background (§20.1402). Appendix A provides the calculated DGCL values for the three radionuclides used in this work. It is worth mentioning that, from a conservative standpoint, it was decided to use agriculture DCGL values.

2.2.2 Minimum Detectable Concentration

As part of the decommissioning process, a licensee evaluates the residual radioactivity from the land areas and building surfaces with radiation detection devices. NRC defines the minimum detectable concentration (MDC) in NUREG-1507 as “the a priori level that a specific instrument and technique can be expected to detect 95 percent of the time” (Abelquist et al. 2020). NUREG-1507 provides guidance on selecting radiation detectors and how to calculate the MDC of the device with site-specific characteristics. This section describes the a priori MDCs for the surveys conducted.

2.2.2.1 Factors Contributing to the MDC

The MDC is the radiological contaminant detectability level, or minimum concentration of a radionuclide that can be detected above a predetermined confidence level. To calculate the MDC, one of the first steps is to estimate the background count rate. Next, several other factors are incorporated to arrive at the MDC equation.

The MDC for a survey is estimated using Equation 1. The parameters for calculating the MDC are described below.

$$MDC\ (pCi/g) = \frac{d' \times \sqrt{b_i} \times (60/i)}{\sqrt{p}\ \times CPMR\ \times ERC} \qquad \text{Equation 1}$$

Index of Sensitivity (d’)

During field surveys, the surveyor is responsible for identifying the differences in response from background and background plus signal. The background and the source (background plus signal) are assumed to be two normal distributions with equal variances. The index of sensitivity is defined as the difference in the distributions in units of their standard deviation (Equation 2).

$$d' = z\ (\text{false positive}) - z\ (\text{true positive}) \qquad \text{Equation 2}$$

The probability of false positives and true positives are sometimes also referred to as α and (1−β), respectively. For this work, the acceptable probability of a true positive and false positive was set at 95 and 5 percent, respectively. This gives a d’ value of 3.28. These probabilities result in confidence levels that are consistent with most radiation detection work and result in establishing a conservative discrimination limit between the background and background plus the source signal.

Surveyor Efficiency (p)

The surveyor efficiency is the efficiency of the surveyor in identifying radioactive hotspots above the MDC. The surveyor efficiency is often compared to an ideal observer whose efficiency is considered to be unity. Under ideal survey conditions, the efficiency of the human is not 100%; moreover, while performing a gamma survey without any additional assistance, the efficiency is further reduced. Based on NUREG-1507 (Abelquist et al. 2020), the surveyor efficiency in most cases is between 0.5 and 0.75. Therefore, from a conservative standpoint, a surveyor efficiency (p) of 0.5 was assumed.

Observation Interval (i)

The observation interval (i) is the amount of time the detector is present over the source/hotspot, and NUREG-1507 (Abelquist et al. 2020) provides specific guidance in calculating its value. It is assumed that the area of the contaminant hotspot is 0.25 m^2 (28 cm in radius or 56 cm in diameter). The observation interval is the amount of time it would take the detector to traverse through the hotspot across its diameter. At the velocity the human/drone surveys are expected to traverse (0.2 m/s), the approximate observation interval in this study was determined to be about 2.8 s (US Army Corps of Engineers 2006; Millsap and Brush 2015; Ramos Pinto et al. 2021).

Count-Rate-to-Exposure-Rate Ratio (CPMR)

In the process of estimating the MDC, a relationship between the radiological properties of the source and the response of the detector needs to be established. In most outdoor surveying activities, NaI scintillation crystals are used for detectors (Abelquist 2014). The manufacturers generally provide the response of the detector at 662 keV; for example, for a 2 in. × 2 in. NaI detector, the expected count rate is 900 counts per minute per µR/hr. At low energies, most of the interactions are dominated by the photoelectric effect, where the entire energy of the photon is deposited in the crystal. As the energy increases, Compton scattering becomes dominant. In this mechanism, only partial energy is deposited in the crystal. If the energy of the photon is increased further, the detector will record fewer counts as the interaction cross sections decrease. NUREG-1507 (Abelquist et al. 2020) provides the CPMR for a 2 in. × 2 in. NaI detector for Cs-137 and Co-60. In addition, the response of a 2 in. × 0.04 in. NaI crystal was evaluated analytically as prescribed in NUREG-1507 (Abelquist et al. 2020) to arrive at a CPMR value for Am-241 (Appendix A describes radiation detectors often used in decommissioning surveys). Table 5 provides the CPMR values used for the radionuclides of interest in this work.

Table 5. CPMR Values Used for Am-241, Cs-137, and Co-60

Radionuclide	CPMR (cpm per µR/hr)
Am-241	11,400
Cs-137	900
Co-60	429

Exposure-Rate-to-Concentration Ratio

The exposure-rate-to-concentration ratio (ERC) provides the exposure in terms of µR/hr for a given specific activity (pCi/g) as a function of distance. NUREG-1507 (Abelquist et al. 2020)

provides guidance for calculating this value using the software, Microshield™. ERC is defined for a specific distance, source geometry, and gamma-emitting radionuclide. A cylindrical volume is initially modeled measuring 28 cm in radius (0.25 m^2 area) and 15 cm in depth (~37,500 cm^3). This volume is assumed to be a hotspot filled by a soil-like medium with a density of 1.6 g/cm^3 and has a specific activity of 1 pCi/g for any radionuclide of interest. A point is selected above the center of the hotspot to obtain the ERC as a function of height. Appendix C further describes these calculations for the ERC.

It is worth noting that the model suggested in NUREG-1507 (Abelquist et al. 2020) could not be recreated in the experimental domain for this proof-of-concept project; thus, disk sources were used. However, an attempt was made to simulation the equivalent amount of activity in a cylindrical hotspot using a disk source. The volume of the hot spot is approximately 37,500 cm^3. Multiplying this by the density (1.6 g/cm^3) results in the total mass of about 60,000 grams. The specific activity was assumed to be 1 pCi/g. Therefore, the total activity in this cylindrical hotspot is about 60,000 pCi or 0.06 µCi. This activity was modeled in a disk source measuring 0.02 cm thick and a radius of 0.1 cm. The density of the disk source was assumed to be 1.6 g/cm^3. Exposure rates in µR/hr were calculated at the periphery of the cylindrical hotspot (dispersed source) and compared against the exposure rates at the same distance from the center (28 cm) using a disk source (Appendix C).

Nevertheless, from a conservative standpoint, it was decided to use the dispersed cylindrical model for both ERC and observation interval (i) calculations. The ERC values calculated for Am-241, Cs-137, and Co-60 as a function of height from the center are presented in Table 6.

Table 6. ERC Data Computed in Microshield™ for Radionuclides of Interest as a Function of Height

Radionuclide	Height (cm)	ERC (µR/hr per pCi/g)
Am-241	10	4.67E-3
Am-241	20	2.87E-3
Am-241	30	1.83E-3
Am-241	100	2.53E-4
Cs-137	10	2.47E-1
Cs-137	20	1.42E-1
Cs-137	30	8.90E-2
Cs-137	100	1.29E-2
Co-60	10	1.01E0
Co-60	20	5.79E-1
Co-60	30	3.59E-1
Co-60	100	5.23E-2

2.2.2.2 Background Measurements and Calculations

Background measurements were recorded in an indoor lab environment and at PNNL's large detector array facility (3440 facility and test track). The background measurements and calculations are further described in Appendix D.

For the MDC calculations, a velocity of 0.2 m/s was assumed, which gives an observation interval (i) of 2.8 seconds. The surveyor efficiency (p) and index of sensitivity (d') was assumed to be 0.5 and 3.28, respectively. A background count rate of 7870 cpm was used for the Ludlum 2 in. × 2 in. detector. For the Alpha Spectra 2 in. × 0.04 in. detector, a background count rate of 1290 cpm was used. The CPMR and ERC values representative of each scenario as described in section 2.2.2.1 were used. Table 7 presents the calculated MDC values.

Table 7. Calculated MDC for Each Radionuclide of Interest as a Function of Detector Height.

Radionuclide	Height (cm)	CPMR (cpm per µR/hr)	ERC (µR/hr per pCi/g)	DCGL (pCi/g) [a, b]	MDC (pCi/g)
Am-241	10	11,400	4.67E-3	370	14.5
Am-241	20	11,400	2.87E-3	370	23.6
Am-241	30	11,400	1.83E-3	370	37.0
Am-241	100	11,400	2.53E-4	370	267.4
Cs-137	10	900	2.47E-1	13	8.6
Cs-137	20	900	1.42E-1	13	14.9
Cs-137	30	900	8.90E-2	13	23.9
Cs-137	100	900	1.29E-2	13	164.1
Co-60	10	429	1.013E0	3.8	4.4
Co-60	20	429	5.789E-1	3.8	7.7
Co-60	30	429	3.58E-1	3.8	12.4
Co-60	100	429	5.225E-2	3.8	85.0

[a] DCGLs are described further and assessed for this study in Appendix B

[b] For comparison purposes, NUREG-1757, Table H.2 (Barr et al. 2020), provides the following surface soil screening values equivalent to 25 mrem/yr for unrestricted release: 2.1 pCi/g Am-241; 11 pCi/g Cs-137; and 3.8 pCi/g Co-60. The calculated values for the DCGLs provided in this table are slightly different as they are based on an agricultural resident, which is different from the scenario considered in NUREG-1757. The differences for the DCGLs in NUREG-1757 and this table for Am-241 is associated with differences in the inhalation factors for Am-241 with the different scenarios. The DCGLs calculated for the purposes of this study only consider the external dose pathways. The screening values in NUREG-1757, volume 2, Table H.2 for surface soils are based on a number of pathways including plant, animal/product, and drinking water pathways that lead to significantly lower screening values for certain radionuclides dominated by internal or groundwater dependent pathways.

Comparing the MDC values for Am-241 with the DCGL values, it was observed that the survey using the Alpha Spectra 2 in. × 0.04 in. detector would be successful in meeting the requirements in 10 CFR 20.1402, "Radiological criteria for unrestricted use."

For Cs-137, at 10 cm the MDC was under the DCGL, while at 20 cm the detector no longer met the requirements of 10 CFR 20.1402. For Co-60, the MDC was observed to be above the DCGL at 10 cm. Therefore, to improve the MDC of a scan, one or more of the following can be implemented while using a NaI detector:

- Reduce the distance between the ground and the face of the detector. Note, for decommissioning activities, surveyors generally scan at about 5 cm above the ground (King et al. 2012; Abelquist 2014). Reducing the distance helps in increasing the ERC.
- Increase the size of the scintillation crystal. This helps in increasing the CPMR.
- Reduce the velocity of the scan, resulting in an increase in observation interval (i).

To improve the MDC and satisfy the DCGL requirements to meet 10 CFR 20.142 regulations, the experimental design of the evaluation tried to address these points by evaluating two heights with two detectors at the lowest scan velocity.

2.2.2.3 Radiological Check Sources

This section covers the general procedure followed to select the ideal source activities for the radiological surveys. For this evaluation, radiological check sources are a known quantity of a radionuclide in a secured medium (e.g., a plastic disk). Several steps were taken in the selection of check sources for the experimental design:

- Estimate the background count rate as a function of distance from the ground (step 1).
- Based on the index of sensitivity (d'), surveyor efficiency, and the survey velocity, compute the MDCR (step 2).
- Calculate a minimum gross count rate. This is the sum of the background and the minimum detectable count rate (step 1 + step 2).
- Use a source of known activity to record the gross count rate (cpm) as a function of distance (step 4).
- Subtract the background count rate from the gross count rate to obtain the net count rate from the source (step 4 − step 1). Use this information to compute the count rate per unit activity as a function of distance (step 5).
- Calculate the minimum activity required to successfully detect a source at a given distance by dividing the MDCR by the count rate per unit activity as a function of distance (i.e., step 2 ÷ step 5).

It must be noted that these calculations were performed using a stationary detector and source configuration. Therefore, to represent real-life situations where the detector is in motion, it is appropriate to modify the activities by a scaling factor. For this work, a scaling factor of 20% was used. For example, if the theoretical activities were calculated to be 10 µCi, an activity of 12 µCi is recommended. These factors can be appropriately chosen by performing several trial runs. Some corrections might require using the inverse square law rather than the 20% scaling factor because the sources used in this study are not point sources.

A total of nine sources (three sources of each radionuclide) were used on the source transect in the surveys on PNNL's 3440 test track. The count rate per unit activity as a function of distance was experimentally recorded at 20 and 50 cm. A value for 100 cm was calculated using the inverse square rule. A source scaling factor of 20% was used to account for the detector moving over a radiological source. The radiological check source selection was based on meeting the detection count rate requirements shown below:

- Source detected at least 100 cm from the ground.
- Source detected at 20 cm but not at 100 cm.

- Source not detected at 20 cm from the ground.

Table 8 summarizes the theoretical activities for the check sources based on the radionuclide and altitude of the detector over the check source.

Table 8. Theoretical Check Source Activities Required to Collect the Minimum Gross Count Rate to Meet Project Objectives

Altitude (Distance between Detector and Check Source)	Activity Am-241 (μCi)	Activity Cs-137 (μCi)	Activity Co-60 (μCi)
Below 20 cm	< 0.17	< 0.32	<0.17
Above 20 cm; below 100 cm	> 0.17; < 4.5	> 0.32; <6.41	>0.17; <3.18
Above 100 cm	>4.5	> 6.41	>3.18

2.3 Unoccupied Aerial Vehicle and Field Survey Cart

2.3.1 Unoccupied Aerial Vehicle and Payload

The Aurelia X6 (UAV Systems International) was selected as the UAV for radiological survey testing (Figure 1) for several reasons. The Aurelia X6 is a hexacopter (six propellers) and can accommodate a heavy payload (up to 5 kg [11 lb.]). There is space below the battery platform and above the landing gear to accommodate a bulky payload as well as provide protection for the delicate radiation detectors. Finally, PNNL owns more than one of these UAV models, which allows for backup of spare parts and familiarity of the navigation system and other features.

Figure 1. Setting Up the Aurelia X6 UAV

A customized payload was developed to attach to the UAV to conduct the radiological surveys. The payload included a data logger (Ludlum 3000), a radiation detector (Alpha Spectra or Ludlum), and lidar (Garmin LidarLite V3, Garmin® Ltd., Olathe, Kansas). Customized 3D printed casings were used to attach the components securely in a configuration to maintain the center

of gravity for the Aurelia X6. (Note, adjusting attachments to the Aurelia X6 such that the weight of the components was equal around the center of gravity for the overall UAV is critical for stable flight and maintaining a vertical axis of the detector in relation to the ground.) For airworthiness testing of the Aurelia X6 prior to experimental surveys, a surrogate payload was also developed that had the same weight, approximate dimensions, and center of gravity for preliminary UAV testing. Blender software (version 2.82, Blender Foundation) was used to design the 3D casing (Figure 2). The casing was made of polylactic acid filament (Hatchbox) that was printed using a 3D printer (Ender 3, Creality Experts).

Figure 3 shows the Aurelia X6 in flight, with the payload attached. The batteries were located above the payload mount. Below the payload mount was the Ludlum data logger and the radiological detector. Behind the Ludlum data logger mount was the Garmin LidarLite V3 for collecting altitude data during the UAV and human surveys.

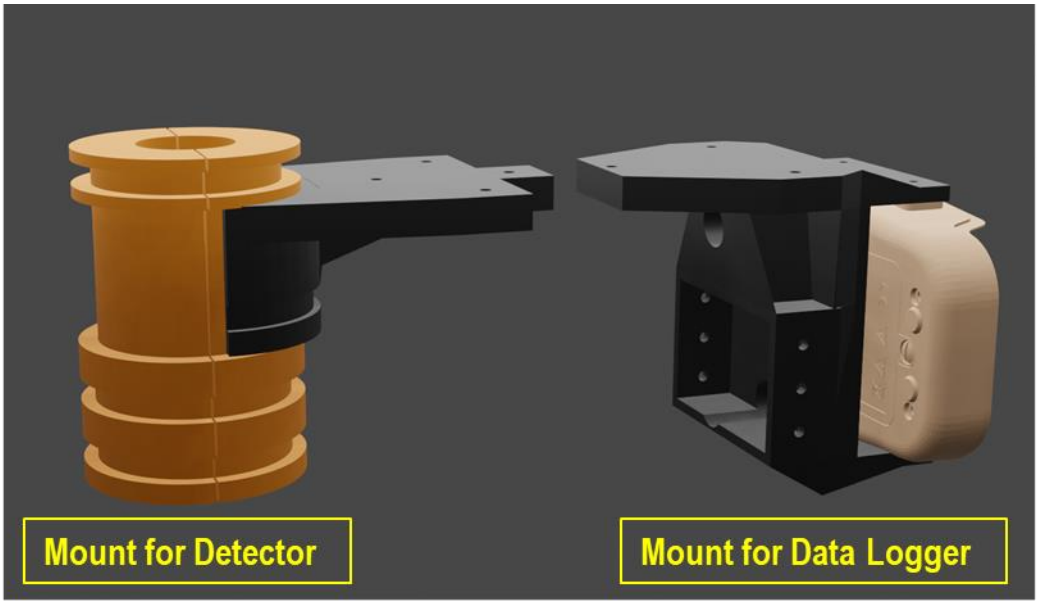

Figure 2. Rendering of the 3D Casing Used to Mount the Payload on the UAV

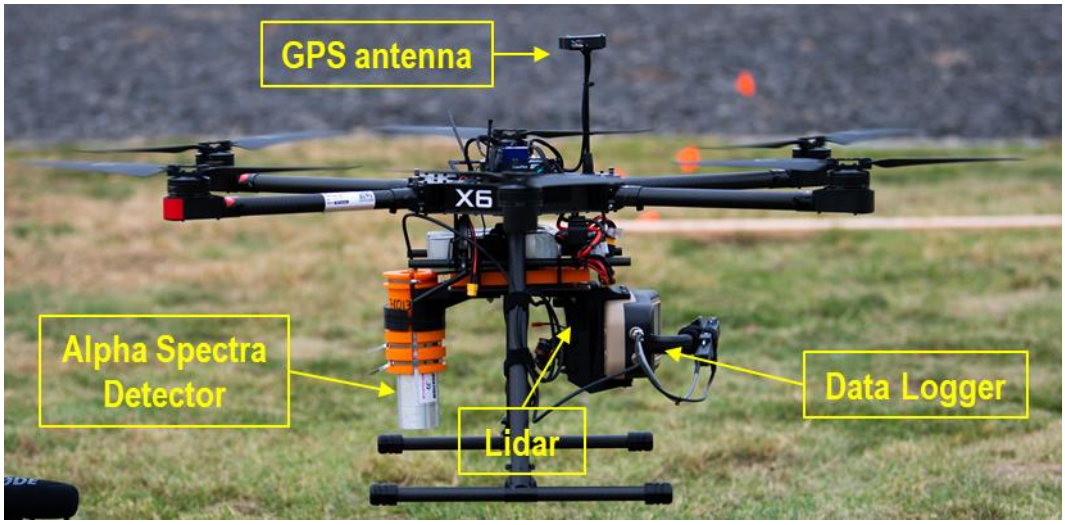

Figure 3. Aurelia X6 in Flight and with Payload.

2.3.2 Field Survey Cart

The cart was modified to include an adjustable cantilever to extend the detector and lidar over the survey area at preset distances above the ground (Figure 4). The UAV was placed on the cart so that all the instruments were consistent between the UAV and human surveys and also to record the position information (GPS) in the human surveys.

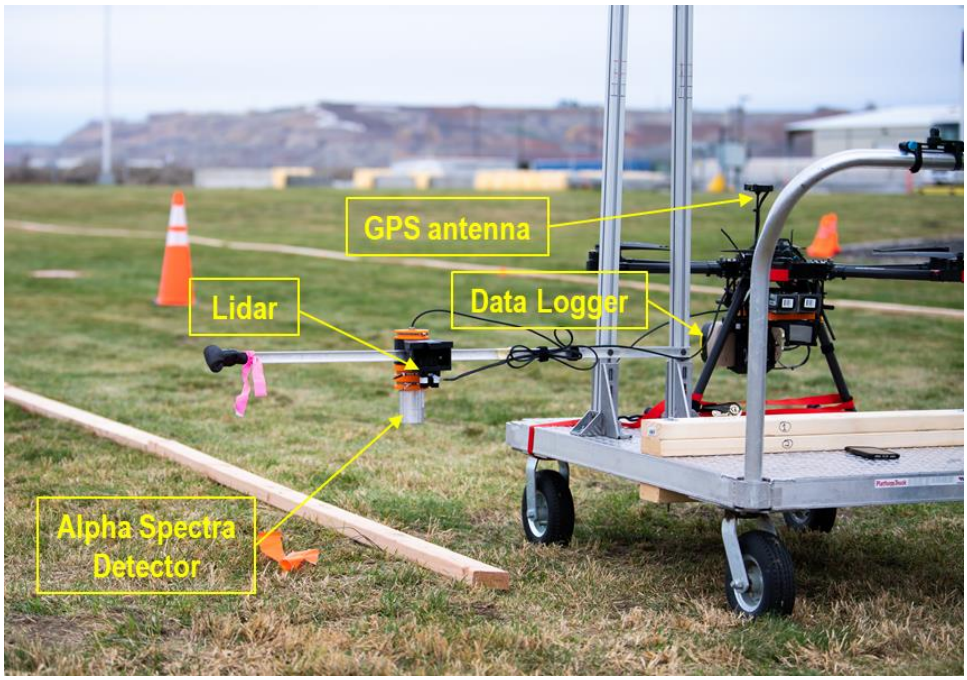

Figure 4. Modified Cart Used to Conduct Radiological Surveys by a Human.

2.3.3 Testing of the UAV for Airworthiness

Prior to conducting the radiological surveys, the modified UAV went through a series of pre-survey airworthiness tests on November 10, 2021. These tests were required to meet the policies for flying a UAV for PNNL and U.S. Department of Energy, Office of Aviation Management. The following tests were conducted at the Tri Cities R/C Modelers field in Richland, WA (3430 Beardsley Rd, Richland, WA 99354):

- Ground test for vibration and structural integrity of the new UAV, without the payload.
- Navigational system evaluations, without the payload:
  - Hop test: flight with the UAV tethered to the ground and maximum height set for the UAV control.
  - Navigation test: flight to a specified height to confirm navigation is operational.
  - Low altitude flights (2 m, 1 m, 50 cm, 20 cm).
- Navigational system evaluations with surrogate payload (i.e., similar weight and configuration to the data logger and radiation detector):
  - Hop test.
  - Navigation test.

- Low altitude flights (2 m, 1 m, 50 cm, 20 cm).

Additional tests with the UAV and surrogate payload were conducted on November 13, 2021, at PNNL's 3440 test track to evaluate the navigation system over the field study flight paths (called transects). Controlling the UAV to fly low and slow requires practice by the pilot and visual observer. A removable 3D printed spacer was installed on the battery platform during testing to replace a foam spacer, which was degrading due to repeated battery changes.

2.4 Field Study

Radiological surveys were conducted on November 13, 2021, at PNNL's 3440 test track after appropriate permits[1] were in place to use the Aurelia X6 and radiological sources (Figure 5).

Figure 5. PNNL's 3440 Test Track Used for UAV and Human Radiological Surveys

[1] Along with having PNNL management approvals, all equipment were required to meet Executive Order 13891, and pilots and visual observers were required to be licensed as per the Federal Aviation Administration Part 107. Additional permits and requirements may be necessary for use of UAVs during decommissioning considering site specific conditions.

2.4.1 Field Setup

Two parallel survey transects, one for radiological sources and one for background, were marked with 2 in. × 4 in. lumber to provide a visual pathway for the human surveyor and UAV pilot to follow (Figure 6). The radiological check sources for Co-60, Cs-137, and Am-241 were randomly placed and secured 6 m apart onto the lumber lined down the west survey transect (herein referred to as source transect) (Table 9), except for the last source, source 9, which was 8 m away from source 8. The east survey transect (herein referred to as background transect) was free of radiological check sources and was representative of background radiological activity.

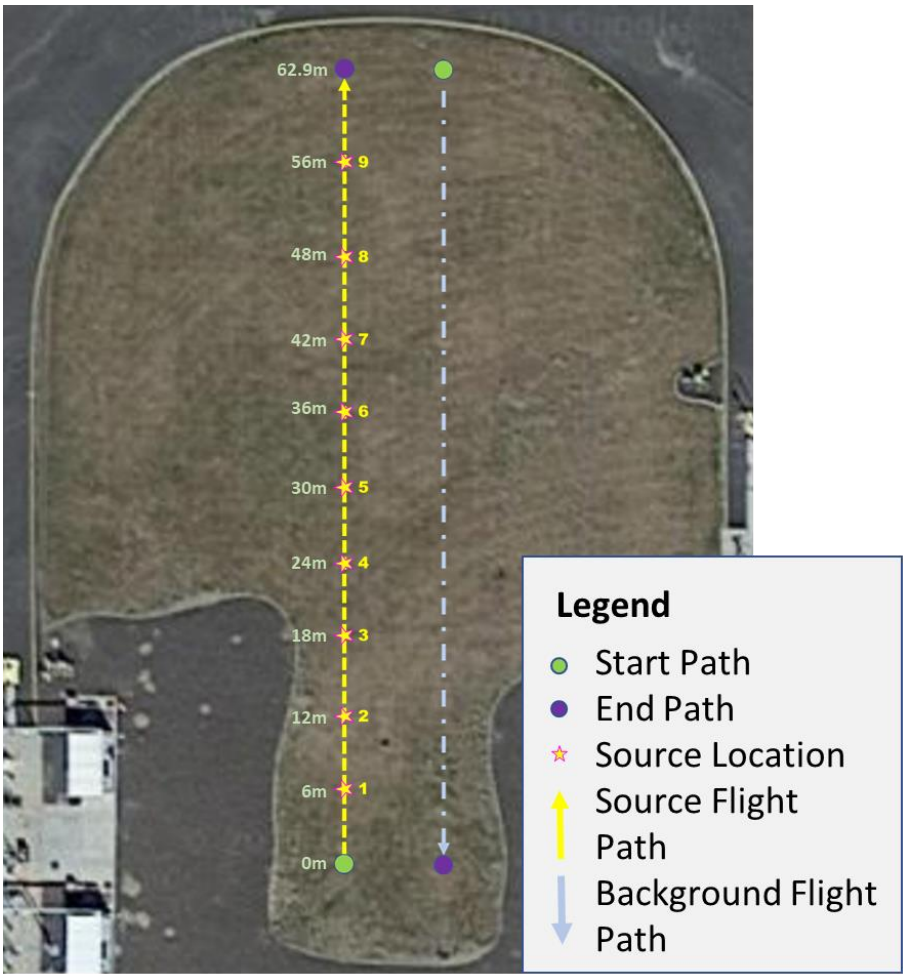

Figure 6. Radiological Survey Field Setup at PNNL's 3440 Test Track

Table 9. Layout of Check Sources and Associated Activity along the Survey Transect

Check Source Number	Radionuclide	Activity (µCi)	Distance from Start of Transect (m)
1	Cs-137	13.24	6
2	Am-241	25.19	12
3	Cs-137	3.54	18

Check Source Number	Radionuclide	Activity (µCi)	Distance from Start of Transect (m)
4	Cs-137	6.88	24
5	Co-60	5.39	30
6	Co-60	10.28	36
7	Am-241	16.97	42
8	Co-60	3.63	48
9	Am-241	39.34	56

2.4.2 Radiological Survey Scenarios

A total of 12 radiological surveys were conducted on November 13, 2021; four surveys were conducted by a human, and eight surveys were conducted by the UAV. Table 10 summarizes the conditions of each radiological survey. Of the replicate UAV surveys, the surveys with the best performance (four of the eight UAV surveys) were analyzed further; the surveys where environmental conditions (e.g., wind above 7–10 mph sustained or moderate gusts) altered the flight were excluded from further proof-of-concept analyses (Table 10 and Table E.1). Table 11 summarizes the experimental conditions for the surveys evaluated and organizes the surveys into scenarios for further comparison. For the UAV, the low altitude ranged from 2.3 to 201.3 cm, and the high altitude ranged from 72.1 to 298.1 cm. For the human surveys, the low altitude ranged from 26.4 to 51.5 cm, and the high altitude ranged from 97.6 to 130.6 cm (Table 11). These altitude values were mainly obtained using the lidar on board the UAS. There was only one regime evaluated for travel velocity of the UAV and human surveys, and the target was 0.2 m/s (Table 11). For the UAV surveys, travel velocities ranged from 0.19 to 0.26 m/s. For the human surveys, travel velocities ranged from 0.18 to 0.21 m/s (Table 11). For further analyses, the following pairs (re: scenarios) of UAV and human surveys were compared for performance:

- Scenario 1: Surveys 9, and 10, low altitude, Ludlum detector.
- Scenario 2: Surveys 11, and 6, low altitude, Alpha Spectra detector.
- Scenario 3: Surveys 1, and 2, high altitude, Ludlum detector.
- Scenario 4: Surveys 12, and 4, high altitude, Alpha Spectra detector.

Table 10. Radiological Survey Experimental Design

Survey	Surveyor	Survey Altitude	Detector	Analyzed?
1	UAV	High	Ludlum	Yes
2	Human	High	Ludlum	Yes
3	UAV	High	Alpha Spectra	No
4	Human	High	Alpha Spectra	Yes
5	UAV	Low	Alpha Spectra	No
6	Human	Low	Alpha Spectra	Yes
7	UAV	Low	Ludlum	No
8	UAV	High	Ludlum	No
9	UAV	Low	Ludlum	Yes
10	Human	Low	Ludlum	Yes
11	UAV	Low	Alpha Spectra	Yes
12	UAV	High	Alpha Spectra	Yes

Table 11. Altitude and Velocity for Analyzed Surveys

Scenario	Survey	Surveyor	Survey Altitude	Detector	Transect	Minimum Altitude (cm)	Maximum Altitude (cm)	Average Altitude (cm)	Median Altitude (cm)	Average Velocity (m/s)
1	9	UAV	Low	Ludlum	Source	2.3	201.3	18.6	15.3	0.20
					Background	-	-	19.3	16.3	0.20
	10	Human	Low	Ludlum	Source	26.4	46.4	32.5	30.4	0.20
					Background	-	-	31.5	30.4	0.20
2	11	UAV	Low	Alpha Spectra	Source	4.2	51.2	27.1	26.2	0.19
					Background	-	-	26.8	25.2	0.19
	6	Human	Low	Alpha Spectra	Source	28.5	51.5	40.2	39.5	0.21
					Background	-	-	35.7	33.5	0.20
3	1	UAV	High	Ludlum	Source	72.1	298.1	91.3	87.1	0.23
					Background	-	-	84.4	81.1	0.26
	2	Human	High	Ludlum	Source	101.5	127.5	108.7	108.5	0.20
					Background	-	-	107.2	107.5	0.18
4	12	UAV	High	Alpha Spectra	Source	84.6	130.6	96.9	96.6	0.19
					Background	-	-	100.5	100.6	0.20
	4	Human	High	Alpha Spectra	Source	97.6	130.6	104.3	105.4	0.20
					Background	-	-	104.1	104.6	0.19

Before each survey commenced, several steps were taken to set up the UAV (Figure 3) and cart (Figure 4) to ensure optimal data collection:

- Setting up instrumentation to record position of detector:
  - GPS measurements were collected with the Aurelia X6 for the UAV flights and for the human surveys (by loading the Aurelia X6 on the cart).
  - Lidar instruments collected altitude information. Two Garmin LidarLite V3 were used. One was mounted on the back of the data logger as part of the Aurelia X6 payload (Figure 3). The other was mounted on the back of the detector holder on the cart (Figure 4). The cable from the lidar unit to the Aurelia X6 was reconnected before the UAV or human survey. In early evaluations of the lidar units, there was a drift in the altitude data over time, for ~ 15 minutes after turning on the instrument. Therefore, before each survey, the lidar unit was turned on (re: warmed up) for at least 15 minutes before the survey commenced.
- Setting up radiation detector and data logger:
  - The cable attachment from the detector (either the Ludlum or Alpha Spectra) to the data logger was adjusted. For all the surveys, the data logger remained attached to the Aurelia X6. In early evaluations of the data logger, there was a drift in background data over time, for ~ 5 minutes after turning on the instrument. Therefore, before each survey, the data logger was turned on (re: warmed up) for at least 5 minutes before the survey commenced.
  - A reference source was placed at the bottom of the radiation detector (on contact) as the lidar was being warmed up as well as at the end of the survey (after completing the background transect). The reference source was Co-57 with an activity of 6.162 µCi (as of October 1, 2020). The reference source created a high activity reading compared to background and was visible on the data logger display, confirming the data logger was functional for field measurements. The high activity reading of the reference source was valuable for the data analysis and for aligning information from the Ludlum data logger of radiological values to the position information of the radiological detector (i.e., GPS and lidar data).
- UAV batteries were replaced before each survey to ensure there was enough power for flight and/or collection of GPS measurements.

2.5 Data Analysis Methods

As a proof-of-concept project, the field setup and analysis were designed to compare data collected by UAV and human surveys, including radiological detection of check sources as well as the survey paths covered by the detectors. Survey paths included lateral information (latitude and longitude coordinates) and altitude (vertical measurement between instrumentation and ground or lumber to which check sources were attached). Statistical tests were used to determine whether the human and UAV surveys were statistically (significantly) different, and if so, to determine the factors that might have contributed to the differences. The primary research questions of interest were:

- Did observed UAV paths differ from human paths, and if so, by how much?
- Did survey path deviation affect survey results, and if so, how?
- Were radiological measurements from human and UAV surveys significantly different?

First, an analysis dataset was created from these four independent data streams. The four independent data streams were:

- Metadata including source location information (GPS information from Aurelia X6 collected over each check source) and field data sheet with survey start time and survey end time.
- Radiological measurements collected by the Ludlum or Alpha Spectra detector and recorded by the data logger (in kcpm).
- GPS data (latitude and longitude coordinates) collected by the Aurelia X6 during each survey.
- Altitude data collected by the Garmin LidarLite V3 lidar units mounted on the AureliaX6 or on the cart.

Section 2.5.1 discusses the data processing steps to create an analysis dataset. Section 2.5.2 discusses the statistical tests and how they were applied to the analysis dataset. Section 3.0 discusses the results.

2.5.1 Data Processing

This section describes the various types of data processing methodologies applied in this work.

2.5.1.1 Time Intervals

Each instrument collected data in unique time intervals, which required alignment of the data to that collected by other instruments. Radiation measurements from the radiological detectors were collected in 1-second intervals with the data logger as shown in Table 1. GPS (latitude and longitude coordinates) data were collected by the Aurelia X6 approximately every 0.2 seconds, and the lidar (altitude) data were collected approximately every 0.05 seconds. Alignment was performed by averaging GPS and lidar observations within each 1-second (longest) interval. The resulting dataset included count, GPS, and lidar observations, each measured at 1-second intervals.

As described in section 2.4.2, a reference source was placed at the bottom of the detector before and after each survey. The reference source confirmed the functionality of the data logger by providing a high activity reading in the dataset at the start and end of each survey. Appendix E.1 shows the radiological measurements vs. elapsed time for all the surveys.

Time was manually recorded on field data sheets when the survey started and ended over the source and background transects. These notes were used to denote the actual start and end times for each transect in the radiation measurements from the data logger, the coordinates from the GPS, and the altitude measurements from the lidar.

2.5.1.2 Position Offsets

Additional offsets were calculated to account for the heights and relative location of each instrument on the Aurelia X6 and the cart. Figure 3 shows the instrument configuration on the UAV and Figure 4 shows the instrument configuration on the cart. The bottom of the detector and the lidar were offset by approximately 15.5 cm on the UAV and 11 cm on the cart. Lidar altitudes were corrected for detector offsets and calculated ground level for each survey. On the cart, the GPS system was located 106 cm away from the detector (lateral distance). GPS coordinates were corrected to account for this offset.

For example, Figure 7 shows the GPS data for surveys 1 (UAV, Ludlum, high) and 2 (human, Ludlum, high) prior to correcting for the GPS offset for the distance between the detector and the GPS system on the cart. Data from the human survey was captured on the “inside” of the UAV data due to the cart configuration. Figure 8 shows the data after considering the offsets for survey 1 (UAV) and survey 2 (human) over the source transect (with the nine check sources).

2.5.1.3 Time Offsets

Time offsets were required for data processing to complete alignment of the position data and radiation measurements. Section 2.4.2 described the “warm-up period” for instruments prior to each survey. In the data processing, the warm-up times for each instrument were used to validate start and end of each survey, indicating which data points to include in the survey analysis dataset for comparison of the UAV and human surveys. The beginning and ending positions of the source and background transects were determined using the start and stop times recorded on the field data sheets, which were then cross-checked with the source locations and the observed paths. Figure 9 shows the observed radiation measurements vs. elapsed time.

2.5.1.4 Transect Identification

Since the surveys were performed using continuous collection of information (i.e., continuous survey) over the source transect and then onto the background transect, and due to background signal in the collected data, there was no clear marker to identify the end of one transect and the beginning of the other (Figure 7 and Figure 8). The times recorded on the field data sheets were used to identify the position and radiation counts for the transects analyzed for each survey. This resulted in an additional variable in the data processing to identify the transect for each observation. The analysis of the background transect data has not been included in this report.

2.5.1.5 Source Segments

Once the source and background transect were isolated for each survey, the source transect were further divided into segments for each of the check sources. Source locations were measured with the GPS post-experiment, for approximately 1 minute per source (allowing numerous coordinate recordings from as many as 29 satellites), which provided both source location (latitude and longitude coordinates) and a measure of uncertainty for the GPS system. The midpoint between the location of each check source serves as the cutoff to create check source segments. The number of data points collected within each source segment is represented by *n* in Table 13 through Table 16. Figure 9, shows an example of the source locations (bottom image) and resulting source segments for each check source. These segments are used to compare the UAV and human radiation measurement distributions (in kcpm) as well as the lateral and vertical deviations of the surveyor from the check sources.

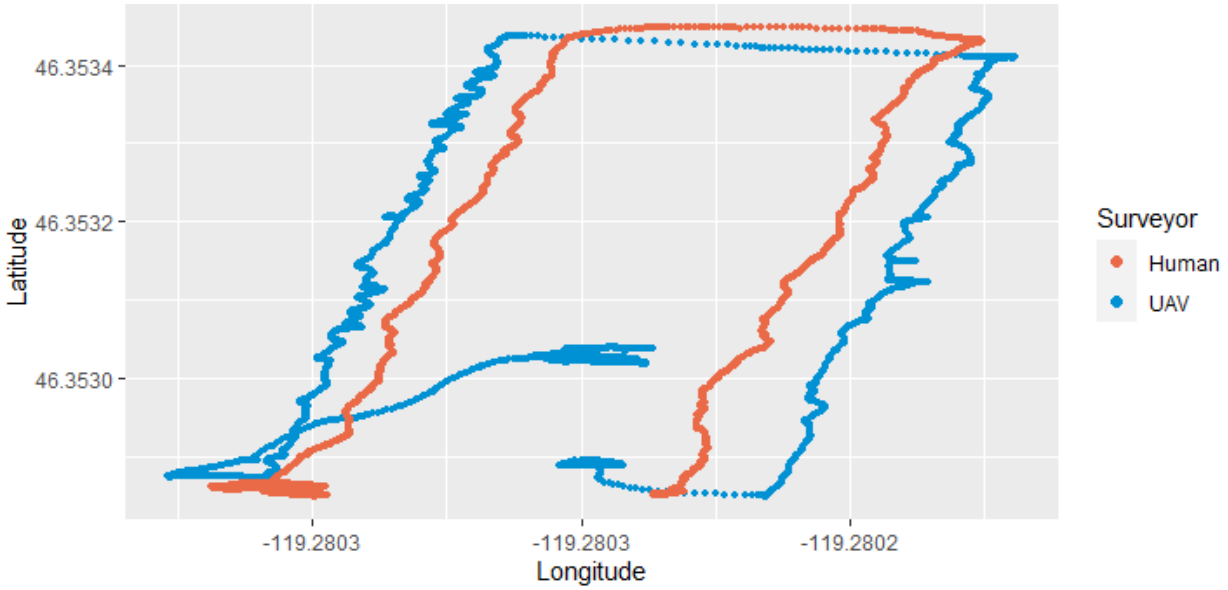

Figure 7. Spatial Data of Survey Paths for Surveys 1 (UAV, Ludlum, High) and 2 (Human, Ludlum, High). These paths have not been corrected for offsets, and the human survey path is “inside” the UAV survey path (as discussed in section 2.3.2). The clustered points near the beginning and end of each transect represent data collected pre-survey and post survey.

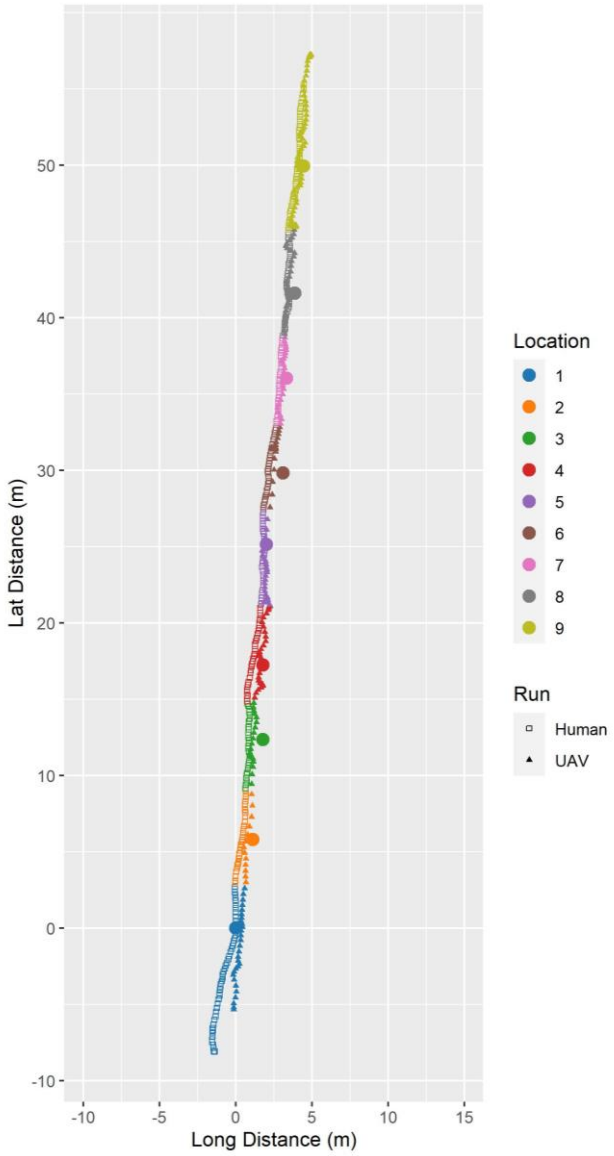

Figure 8. Surveys 1 (UAV, Ludlum, High) and 2 (Human, Ludlum, High) Over the Source Transects. The offset for survey 2 was corrected. Segments of the surveys are color coded based on the source locations 1 through 9.

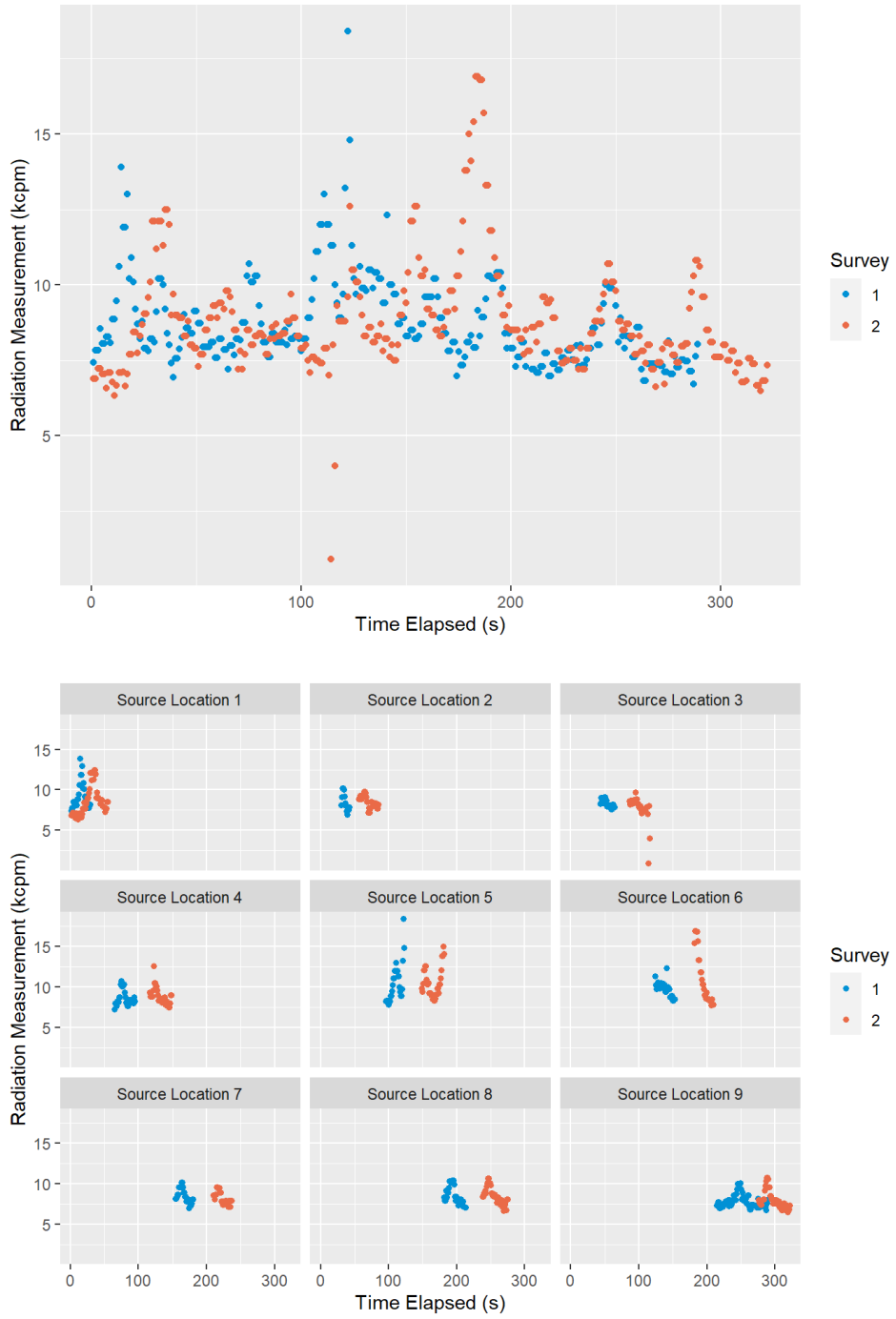

Figure 9. Observed Radiation Measurements for Survey 1 (UAV, Ludlum, High) and Survey 2 (Human, Ludlum, High) as a Function of Elapsed Time. (Top) shows the observed results of the source transect radiation measurements. (Bottom) shows the observed measurements for each check source evaluated along the source transect. Survey 2 shows two anomalous values just after 100 s, which were discovered to be data logging errors and were corrected prior to analysis.

2.5.1.6 Anomalous Data

Throughout data processing, several anomalous data values were discovered, investigated, and either corrected or allowed to be incorporated in the analysis. The percentage of anomalous values was less than 0.02% per transect, so their impact on the summary statistics and the analysis was expected to be minimal because the lidar data were collected at such a high rate. Further, due to the data frequency, true altitude changes were observed with numerous data points forming peaks rather than as instantaneous changes from one time point to the next. In cases when investigating anomalous values indicated data logging errors, the observations were corrected. Anomalous values that could not be attributed to a data logging error were included for further analysis.

As an example, consider the lidar (height) data from survey 1 (UAV) in Figure 10; the transect includes 5,779 data values with a single anomaly (zero value at approximately 08:39:00), which represents 0.017% of the data. This value was anomalous because there was only one point among others that was consistently around 1.5 m; the zero-value had minimal impact on the results.

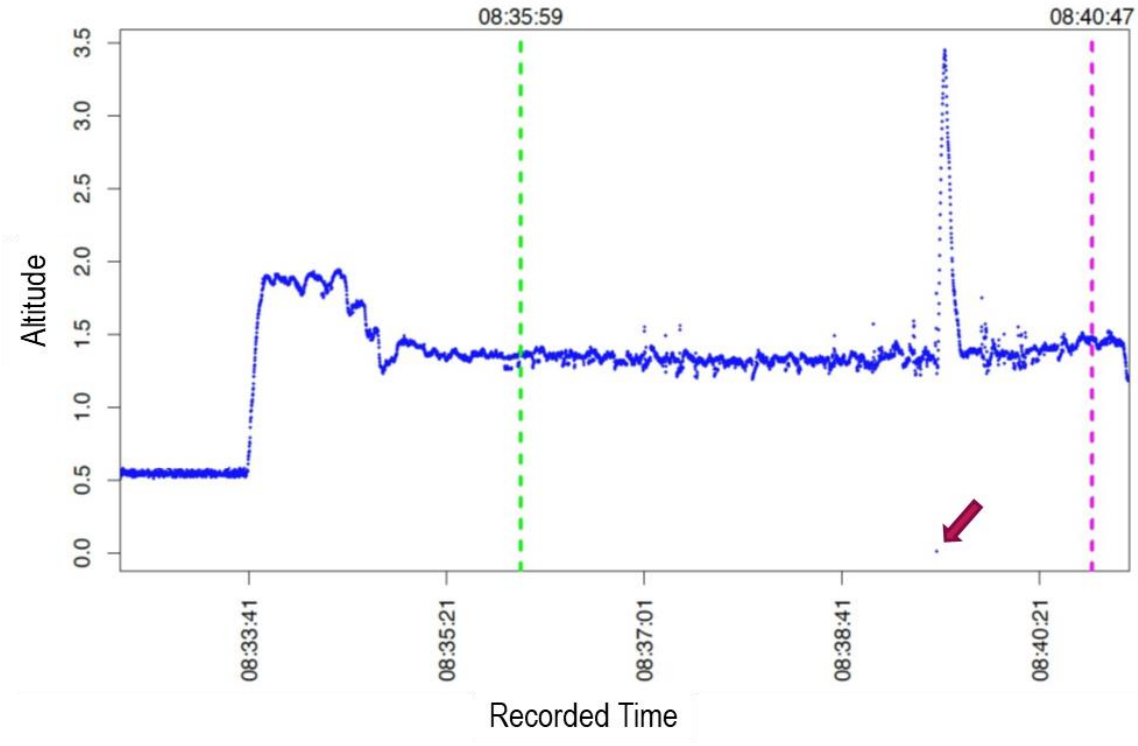

Figure 10. Raw Lidar (Altitude) Data for the Source Transect from Survey 3 (UAV, Ludlum, High) is Illustrated. The altitude data for the survey of the source transect is between the green and magenta lines (start and end times of the source transect, respectively). At the start of the recorded time (x-axis), values of ~ 0.5 m represent the lidar “warm-up” period, and these were used to calculate the height offset for this survey. The points between the warm-up period and the green line represent the time the UAV was flying and approaching the start of the survey transect. Notice the anomalous point of 0.0 m at approximately 08:39:00 (arrow added for emphasis).

2.5.2 Statistical Analysis Methods

The statistical questions posed at the beginning of section 2.5 are systematically answered in this section using a combination of graphical data analysis, statistical tests, and subject matter expert evaluations.

Question 1: Did observed UAV paths differ from the human paths, and if so, by how much? This question addresses any deviation between the UAV and human survey paths as a function of the GPS coordinates.

The approach to answer question 1 was to estimate regression parameters that describe the source transects for the human and UAV survey paths. Consider Figure 11 where the check sources were aligned as straight as possible, but slight east-west (longitudinal) variation is evident, and the check sources were not laid exactly in a north-south line. The slope of a regression line through these points smooths out the lateral deviations and the y-intercept establishes the origin for the north-south orientation.

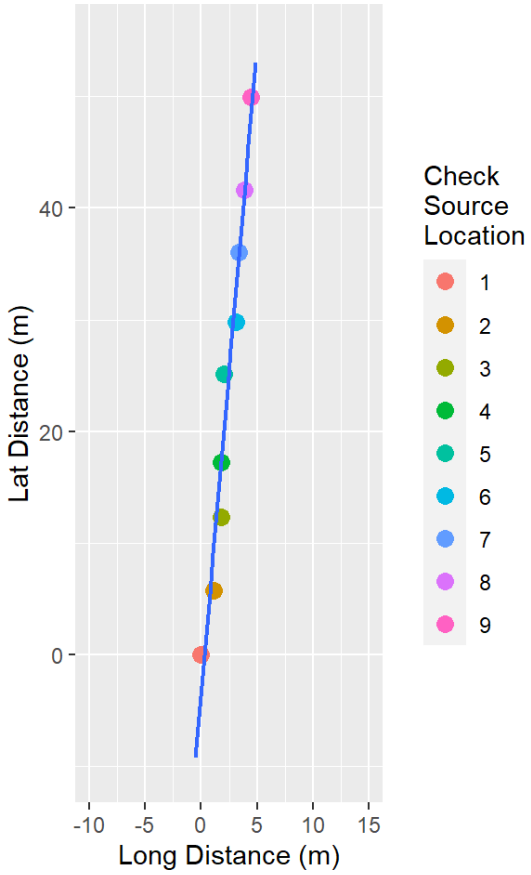

Figure 11. Check Source Locations by Longitude and Latitude in Meters, along with a Regression Line

Similarly, estimating a regression line through the human and UAV survey paths provides a smooth line through the points of each check source. The processed data includes different numbers of observations at different GPS coordinates that were collected at different velocities in the two survey paths (see an example in Figure 12), so a point-by-point comparison was not

possible. The regression line provides a method to directly compare the radiation measurements from survey paths: equivalent slopes and intercepts of the human and UAV regression lines indicate the human and UAV survey followed the same path. In this analysis, equivalence was evaluated relative to the uncertainty in the GPS instrumentation, which at 98% confidence was approximately +/- 36 cm as determined by field analysis prior to surveys.

Question 1 is addressed qualitatively by visually observing the uncertainty of latitude and longitude coordinates at approximately +/- 36 cm, and the graphical results are included in Appendix E for each survey and discussed further in section 3.1. This qualitative approach identifies the survey location closest to the check source location and plots it as a function of time elapsed.

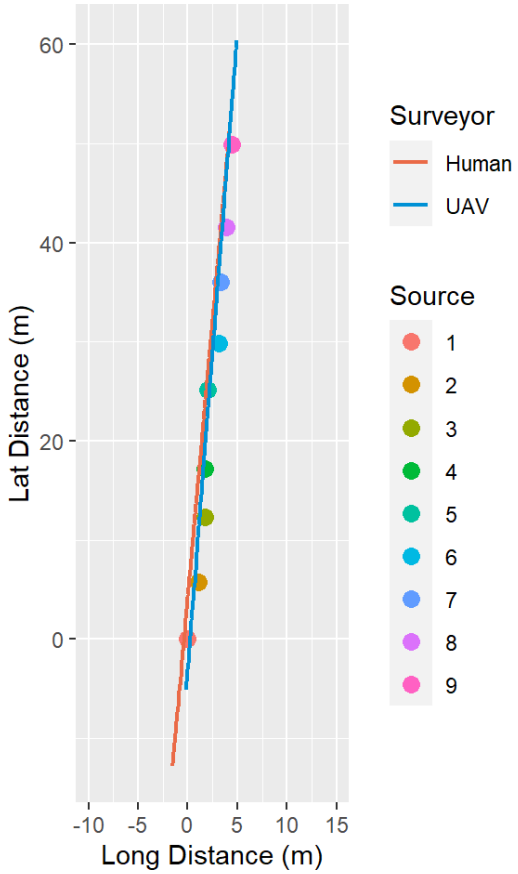

Figure 12. UAV (Blue Line) and Human (Orange Line) Regression Lines for Surveys 1 (UAV, Ludlum, High) and 2 (Human, Ludlum, High). Check source 1 is identified as the origin for converting the latitude and longitude from degrees to meters.

Question 2: Did survey path deviation affect survey results, and if so, how? This question addresses any deviation between the UAV and human survey paths as a function of the altitude (lidar data).

This question was qualitatively evaluated by examining the altitude data and determining if the detectors had the sensitivity to record reliable radiological measurements at the altitudes for the human and UAV surveys. All evaluations were completed on the data corrected for offsets in the instrumentations. The MDCs (Table 7) and the theoretical source activities based on the

distance from the source to the detector (Table 8) indicate that some of the check sources would be challenging for the detectors to record reliable radiation measurements since the count rate is not significantly different from background. Specifically, check sources 3 and 4 (both Cs-137) as well as check source 8 (Co-60) (Table 9) were close to the theoretical limit for the high-altitude surveys (Table 8). While the NaI crystal characteristics of the Ludlum detector were expected to be adequate for this evaluation, the NaI characteristics of the Alpha Spectra detector were not. When the statistical testing for question 3 determined there was a significant difference in the human and UAV count rates results, then the results from questions 1 and 2 (survey path coordinates and altitude) should be considered as possible contributing factors.

Question 3: Were radiological measurements from human and UAV surveys significantly different? This question evaluates the count rate measurements from the detector over the check sources.

If the human and UAV surveys are the same, considering velocity, path, and height differences, their statistical distributions will be statistically equivalent. On a source-by-source basis, then, the cumulative distributions are evaluated using the Kolmogorov-Smirnov (K-S) test. All evaluations were completed on the data corrected for offsets in the instrumentations. The survey-pairs comparisons are shown in Table 10, i.e., scenarios for consideration of paired UAV and human surveys: scenario 1 for surveys 9 and 10; scenario 2 for surveys 11 and 6; scenario 3 for surveys 1 and 2; and scenario 4 for surveys 12 and 4. Figure 13 shows an example of the radiation measurements vs. elapsed time of the UAV and human surveys for surveys 9 and 10, respectively.

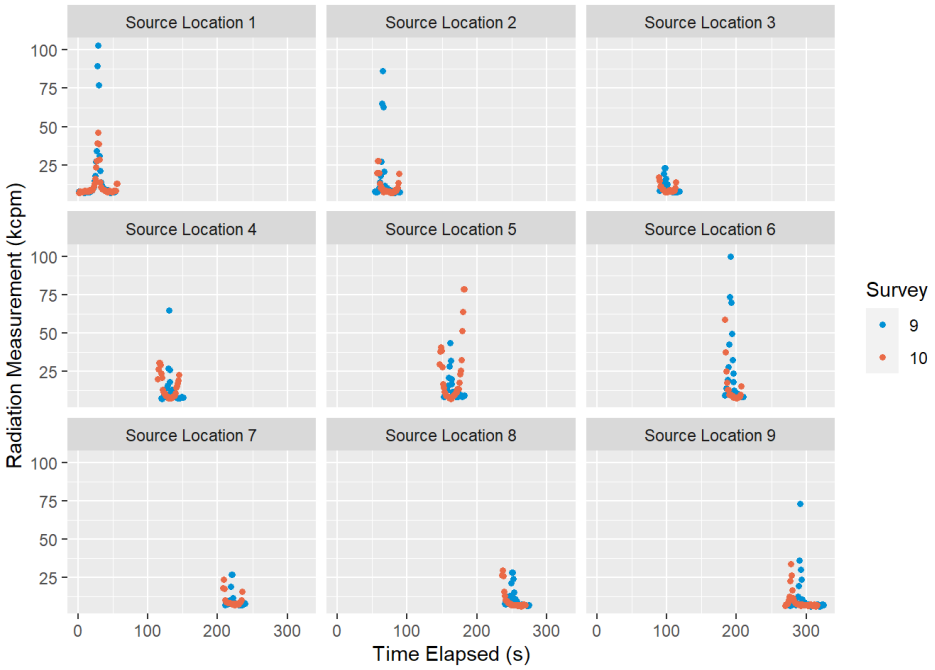

Figure 13. Example of Count Rate vs. Time Elapsed for UAV Survey 9 (UAV, Ludlum, Low) and Human Survey 10 (Human, Ludlum, Low)

The two-sample K-S test is a nonparametric test that is used to test the equivalence of two sample distributions. It is nonparametric in the sense that the test statistic is not formulated on the assumption that the data belong to any particular parametric family of probability

distributions. Nonparametric does not imply the absence of assumptions. The K-S test is based on the assumption that the data consist of two independent random samples measured on at least an ordinal scale (Daniel 1990). The statistical computing software, R (R Core Team 2021) was used to perform the K-S test, and the summaries below are in the notation of Daniel (1990).

The K-S test measures the differences between cumulative distribution functions (CDFs) of two samples. The theoretical CDF of observation y is written as $F(y) = \Pr(Y \leq y)$, where F is unknown. The empirical CDF (eCDF) is observed from the data as the proportion of observations that are less than a particular count value *y* and is defined as:

$$S(y) = \frac{(number\ of\ observed\ counts\ [kCPM] \leq y)}{m} \qquad \text{Equation 3}$$

where y is an observed count value (in kcpm) and m is the number of observations in the sample. As an example, Figure 14 shows the two empirical eCDFs for the source transects from surveys 1 (UAV, Ludlum, high) and 2 (Human, Ludlum, high) for check source 4.

The hypothesis being tested by the K-S test is

$$H_o: F_{UAV}(y) = F_{Human}(y) \text{ for all } y \qquad \text{Equation 4}$$

versus

$$H_a: F_{UAV}(y) \neq F_{Human}(y) \text{ for some } y \qquad \text{Equation 5}$$

where H_o is the null hypothesis and H_a is the alternative hypothesis.

The test statistic for the K-S test is the maximum distance between the two CDFs, depicted as a two-sided arrow in Figure 14. The formula for the test statistic is

$$D_{n,m} = maximum|S_{UAV}(kCPM) - S_{Human}(kCPM)|. \qquad \text{Equation 6}$$

Sufficiently small D corresponds to a small p-value and Ha is supported. Sufficiently small is determined by selecting a false rejection rate of $\alpha = 0.05$. Because we are performing one test per source for each survey (for a total of 9 tests per survey), we applied the Bonferroni correction to the α level by using

$$\alpha^* = \frac{0.05}{9} = 0.0056 \qquad \text{Equation 7}$$

Thus, the overall α^* level per source for each survey was 0.0056.

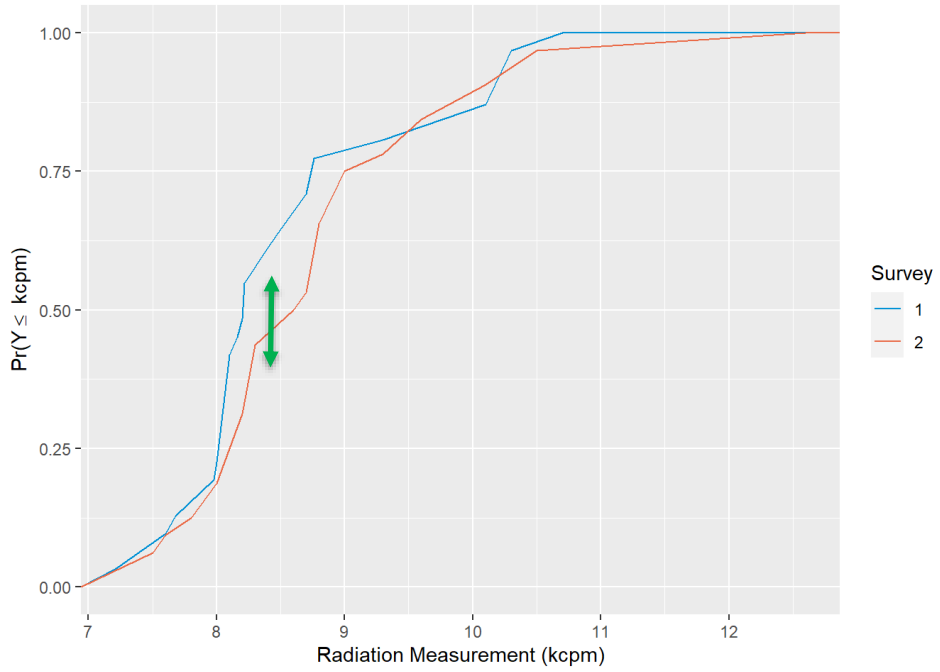

Figure 14. Empirical Cumulative Distribution Functions (eCDFs) of the Data Collected in Surveys 1 (Ludlum, UAV, High) and 2 (Ludlum, Human, High) Over Check Source 4. The two-sided arrow represents the maximum distance between the two empirical CDFs and is the test statistic for the K-S test for these two surveys.

The KS test is an acceptable test for final status surveys as provided in both NUREG-1575 and NUREG-1505 guidance. Because of the nature of continuously collected surveys and the possibility contamination might occur in contiguous areas (hot spots), the data from a site area could be correlated in time and/or space, and so are not strictly independent, as is evident in the peaked behavior of the source transect data (Figure 13; similar results for all evaluated scenarios are included in Appendix E). The KS test can be performed under more general conditions that allow for dependence and heterogeneity between samples; thus, dependence between count rate by UAV and human surveys from the same path is not a concern (Naaman 2021). Appendix E includes similar analyses for all the scenarios.

3.0 Results

Section 3.1 compares the UAV and human survey paths over the source transect for experimental conditions represented by each scenario, while section 3.2 compares the count rate distributions for each testing scenario by check source. If, for a given scenario, the UAV and human paths are equivalent, but the count rate distributions are different, the differences are the result of something other than survey path. Possible differences and considerations are discussed in section 4.0. All eCDFs are shown in Appendix E, but only those with either significant findings or that elucidate discussion are presented below.

As discussed in section 2.5.2, an α error of 0.05 was selected for statistical testing and a Bonferroni correction was applied. That is, the cutoff for statistical significance is α*, or 0.0056 (see equation 7 above for α*), and a p-value less than this number results in the finding that the two distributions are statistically different.

3.1 Comparison of Survey Paths by UAV and Human

The statistical analysis results indicate that the UAV and human paths are statistically equivalent. The observed paths are also equivalent to the check source transect. When considered on a check source by check source basis, some of the UAV and human path segments exceed the GPS uncertainty. Although not statistically significant, similar and dissimilar survey pairs are discussed here to highlight considerations for future UAV survey planning.

The survey path slopes (in m) for the UAV and human surveys are summarized in Table 12. The slope of a path is defined in this context as the upward movement along a path per one meter of lateral deviation. As a result, for all surveys, for a lateral movement of 1 m, the upward movement along a path was between 11 and 12 m. The paths for surveys 12 and 4 had the greatest slope difference (absolute difference = 1.8682), while the paths for surveys 9 and 10 had the smallest slope difference (absolute difference = 0.3605). The slopes of UAV and human surveys were found to be statistically indistinguishable for all four scenarios.

Table 12. Summary of Regression Information Comparing the UAV and Human Surveys

Scenario	Survey	Vehicle	Instrument	Slope	Absolute difference in slope	p-value	Are the Surveys Statistically Different?
1	9	UAV	Ludlum	11.6442	0.3605	0.5679	No
	10	Human	Ludlum	12.0047			
2	11	UAV	AS	12.6255	0.9123	0.5169	No
	6	Human	AS	11.7132			
3	1	UAV	Ludlum	12.7976	1.6598	0.1179	No
	2	Human	Ludlum	11.1378			
4	12	UAV	AS	13.3101	1.8682	0.0529	No
	4	Human	AS	11.4419			

α* = 0.0125, level of statistical difference for comparison to p-value using equation 7 and a total of 4 tests.

Figure 15 depicts the survey paths for surveys 1 and 2, as well as surveys 9 and 10 and the nine check source locations. Note that surveys 9 and 10 both deviate from the source transect in a systematic way, with the survey paths located east of the source transect. So, although the survey paths are equivalent, there is a potential bias in their locations. This is discussed more in section 4.0.

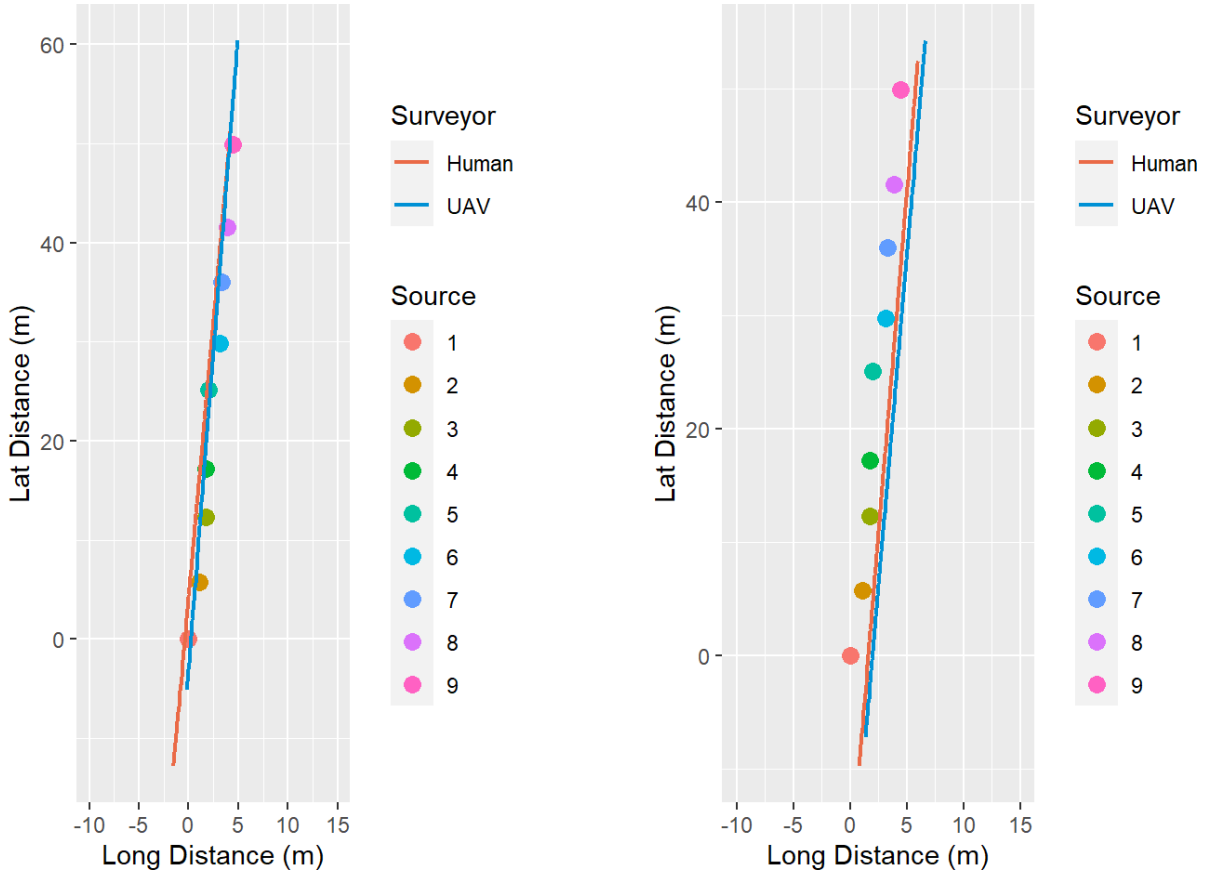

Figure 15. Position Data, with Corrected Offset, for Surveys 1 and 2 (left), and Surveys 9 and 10 (right). Check sources are depicted as dots, and survey paths for the human and UAV surveys are shown as lines.

Figure 16 also shows the lateral distance from the survey path to a check source location for surveys 1 and 2, as well as surveys 9 and 10. For UAV survey 1, two out of the nine (22%) survey path-check source distances exceeded the GPS uncertainty threshold of +/- 36 cm (the blue reference line in Figure 16); the comparative human survey 2 shows a four out of nine (44%) exceedances. For surveys 9 and 10, all (100%) of the surveys exceeded the GPS uncertainty threshold. The patterns indicate that the detector may not have traversed directly over each of the check sources in both the UAV and human surveys, the consequence being that the count rate difference observed between the two surveys can be partially attributed to this factor. This is discussed in section 4.0. The other four surveys in this study followed a pattern similar to surveys 1 and 2.

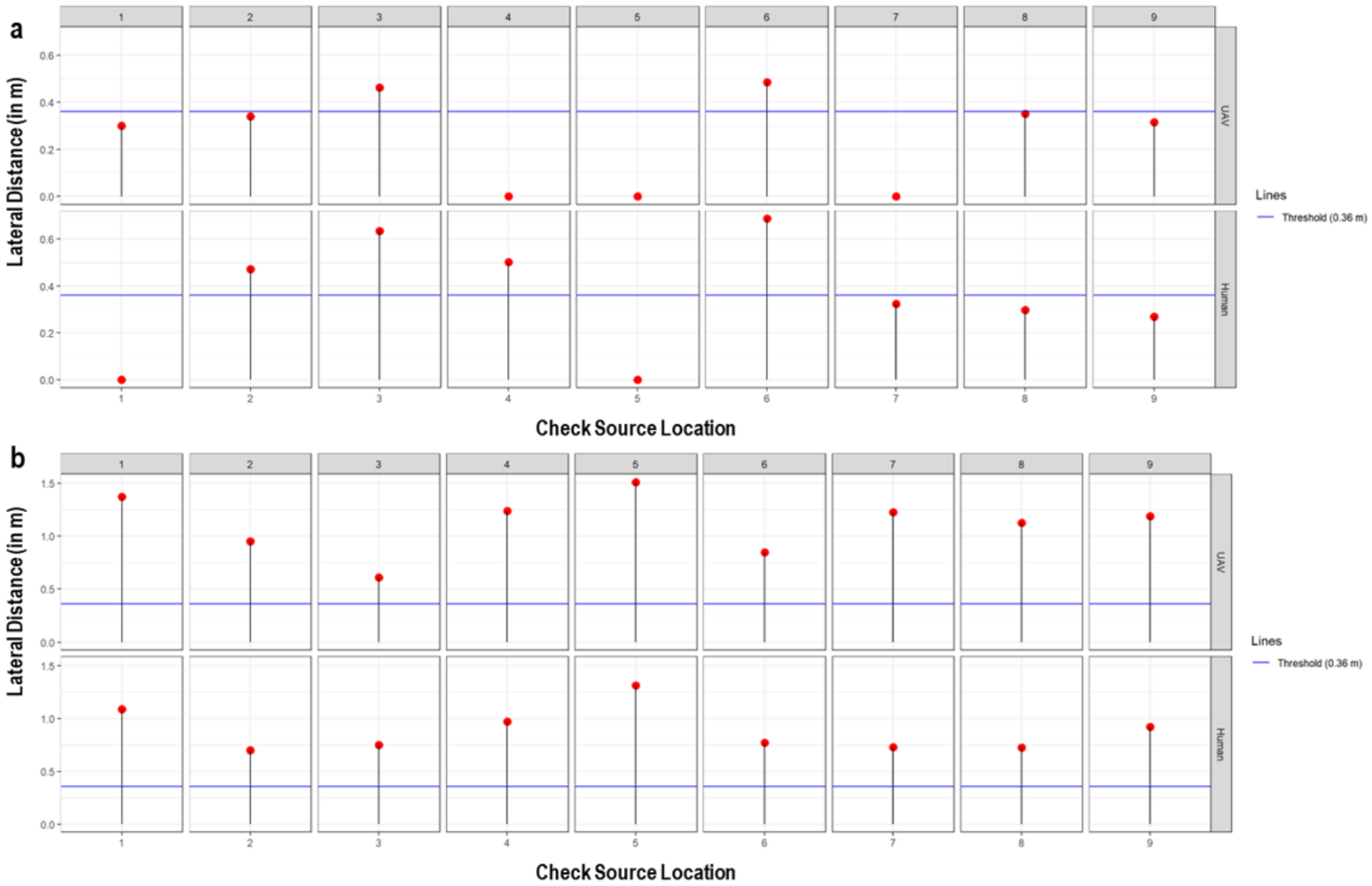

Figure 16. The Lateral Distance (in Meters) of the Detector to the Location of a Check Source for a) Surveys 1 and 2, and b) Surveys 9 and 10. An arbitrary threshold value of 0.36 m is depicted by the blue horizontal line.

3.2 Comparison of Radiological Measurement Data

Radiological measurements were compared for each testing scenario by source. Table 13 summarizes the latitude and longitude coordinates for each of the radiological check sources located on the source transect. Information was collected using the GPS on the Aurelia X6 and was smoothed over several data points collected for several minutes. Figure 12 and Figure 15 illustrate the deviation in distance between sources, representing the uncertainty in GPS measurements and the field variability (e.g., the uneven surface under the boards over the 63 m of the transect).

Table 13. Latitude and Longitude for Each Radiological Source Location. Distance (m) from the previous source is also indicated.

Source Number	Latitude	Longitude	Distance (m)
1	46.352923	−119.280307	NA
2	46.352975	−119.280297	5.83
3	46.353034	−119.280291	6.57
4	46.353078	−119.280291	4.89
5	46.353149	−119.280289	7.89
6	46.353191	−119.280279	4.73
7	46.353247	−119.280277	6.23
8	46.353297	−119.280272	5.57
9	46.353372	−119.280267	8.34

NA = Not applicable

3.2.1 Scenario 1 – Ludlum Detector at Low Survey Altitude (Survey 9 and 10)

Table 14 shows the results for the UAV and human radiological surveys conducted using the Ludlum detector at a low survey altitude. For all check sources, results were not statistically different between the UAV and human.

3.2.2 Scenario 2 – Alpha Spectra Detector at Low Survey Altitude (Survey 11 and 6)

Table 15 shows the results for the UAV and human radiological surveys conducted using the Alpha Spectra detector at a low survey altitude. For most of the check sources, results were not statistically different between the UAV and human. However, for check source 9, Am-241 (with an activity of 39.34 µCi), there is a significant difference between the UAV and the human surveys of that check source.

3.2.3 Scenario 3 – Ludlum Detector at High Survey Altitude (Survey 1 and 2)

Table 16 shows the results for the UAV and human radiological surveys conducted using the Ludlum detector at a high survey altitude. For all check sources, results were not statistically different between the UAV and human.

3.2.4 Scenario 4 – Alpha Spectra Detector at High Survey Altitude (Survey 12 and 4)

Table 17 shows the results for the UAV and human radiological surveys conducted using the Alpha Spectra detector at a high survey altitude. For most of the check sources, results were not statistically different between the UAV and human. However, for check source 4 (6.88 µCi Cs-137) and 5 (5.39 µCi Co-60), there was a significant difference between the UAV and the human surveys of that check source.

Table 14. Scenario 1 Radiological Activity (kcpm) and Statistical Comparison for the Ludlum Detector at a Low Survey Altitude by Check Source and Surveyor. Radiological activities by the UAV and human surveys were compared using the K-S test.

Check Source Number	Isotope	Survey	Surveyor	*n*	Average Activity (kcpm)	Standard Deviation (kcpm)	Minimum (kcpm)	Maximum (kcpm)	p-value	Are the Surveys Statistically Different?
1	Cs-137	9 10	UAV Human	53 56	14.63 11.36	19.64 8.48	6.74 6.61	103 46	0.0677	No
2	Am-241	9 10	UAV Human	36 32	14.79 10.68	18.02 5.72	6.88 6.9	86.1 27.6	0.9972	No
3	Cs-137	9 10	UAV Human	29 25	10.02 9.24	4.55 2.56	7.1 7.2	22.9 17.1	0.9821	No
4	Cs-137	9 10	UAV Human	33 32	12 14	10.68 7.58	7.1 7.2	64.9 30.6	0.1194	No
5	Co-60	9 10	UAV Human	31 37	13.01 21.27	8.14 19.43	8.1 7	43.4 78.4	0.2018	No
6	Co-60	9 10	UAV Human	28 25	22.9 13.36	23.52 11.62	8.1 7.5	100 58.8	0.1184	No
7	Am-241	9 10	UAV Human	29 28	9.74 9.83	5.33 4.04	6.86 7.2	27.1 23.9	0.1591	No
8	Co-60	9 10	UAV Human	35 34	10.48 9.7	5.98 5.94	6.41 6.36	28.3 29.7	0.1478	No
9	Am-241	9 10	UAV Human	51 46	10.35 9.18	10.73 5.42	6.16 6.17	73.4 33.8	0.7421	No

α* = 0.0056, level of statistical difference for survey comparison to p-value, using equation 7 and a total of 9 tests.
n was determined based on the transect identification methodology covered in section 2.5.1.4.

Table 15. Scenario 2 Radiological Activity (kcpm) and Statistical Results for the Alpha Spectra Detector at a Low Survey Altitude by Check Source and Surveyor. Radiological activities by the UAV and human were compared using the K-S test.

Check Source Number	Isotope	Survey	Surveyor	*n*	Average Activity (kcpm)	Standard Deviation (kcpm)	Minimum (kcpm)	Maximum (kcpm)	p-value	Are the Surveys Statistically Different?
1	Cs-137	11 6	UAV Human	60 53	1.71 1.99	1.45 1.67	1 1.14	8.76 10.2	0.2073	No
2	Am-241	11 6	UAV Human	36 28	6.73 8.97	11.99 15.35	0.35 1.39	52.6 54.7	0.0604	No
3	Cs-137	11 6	UAV Human	31 28	1.48 1.64	0.19 0.45	1.27 1.22	1.92 2.65	0.1609	No
4	Cs-137	11 6	UAV Human	34 32	1.9 2.17	0.84 1.22	1.27 1.26	4.19 5.76	0.2620	No
5	Co-60	11 6	UAV Human	34 30	1.78 1.87	0.41 0.63	1.3 1.31	2.71 3.31	0.7168	No
6	Co-60	11 6	UAV Human	30 27	2.89 2.94	1.99 2.59	1.34 1.31	7.56 9.72	0.9141	No
7	Am-241	11 6	UAV Human	32 35	4.98 4.33	7.84 6.61	1.24 0.66	33.1 29	0.7809	No
8	Co-60	11 6	UAV Human	38 35	1.73 1.59	0.76 0.51	1.31 1.07	5.46 2.88	0.0276	No
9	Am-241	11 6	UAV Human	54 46	4.65 4.22	11.71 7.94	1.12 1.05	72.6 38.4	**0.0014**	**Yes**

α* = 0.0056, level of statistical difference for survey comparison to p-value, using equation 7 and a total of 9 tests.
n was determined based on the transect identification methodology covered in section 2.5.1.4.

Table 16. Scenario 3 Radiological Activity (kcpm) and Statistical Results for the Ludlum Detector at a High Survey Altitude by Check Source and Surveyor. Radiological activities by the UAV and human were compared using the K-S test.

Check Source Number	Isotope	Survey	Surveyor	*n*	Average Activity (kcpm)	Standard Deviation (kcpm)	Minimum (kcpm)	Maximum (kcpm)	p-value	Are the Surveys Statistically Different?
1	Cs-137	1 2	UAV Human	29 55	9.21 8.58	1.69 1.76	7.42 6.32	13.9 12.5	0.00750	No
2	Am-241	1 2	UAV Human	13 30	8.5 8.56	1.12 0.72	6.93 7.2	10.2 9.8	0.5143	No
3	Cs-137	1 2	UAV Human	22 31	8.28 7.73	0.46 1.58	7.58 0.9	9.13 9.7	0.1909	No
4	Cs-137	1 2	UAV Human	31 32	8.61 8.83	0.94 1.06	7.21 7.5	10.7 12.6	0.3106	No
5	Co-60	1 2	UAV Human	28 33	10.49 10.52	2.41 1.85	7.8 8.3	18.4 15	0.3408	No
6	Co-60	1 2	UAV Human	30 28	9.76 11	0.9 3.27	8.3 7.7	12.3 16.9	0.0917	No
7	Am-241	1 2	UAV Human	27 28	8.52 8.2	0.89 0.8	6.98 7.2	10.2 9.6	0.1372	No
8	Co-60	1 2	UAV Human	33 38	8.54 8.46	1.14 1.02	7.1 6.63	10.4 10.7	0.7600	No
9	Am-241	1 2	UAV Human	76 47	7.81 7.96	0.8 1.1	6.71 6.49	10.1 10.8	0.3795	No

α* = 0.0056, level of statistical difference for survey comparison to p-value, using equation 7 and a total of 9 tests.
n was determined based on the transect identification methodology covered in section 2.5.1.4.

Table 17. Scenario 4 Radiological Activity (kcpm) and Statistical Results for the Alpha Spectra Detector at a High Survey Altitude by Check Source and Surveyor. Radiological activities by the UAV and human were compared using the K-S test.

Check Source Number	Isotope	Survey	Surveyor	*n*	Average Activity (kcpm)	Standard Deviation (kcpm)	Minimum (kcpm)	Maximum (kcpm)	p-value	Are the Surveys Statistically Different?
1	Cs-137	12	UAV	54	1.4	0.25	1.03	1.93	0.3247	No
		4	Human	53	1.46	0.23	1.14	1.93		
2	Am-241	12	UAV	34	2.9	1.42	1.45	5.99	0.5467	No
		4	Human	30	3.39	2.02	1.27	7.2		
3	Cs-137	12	UAV	31	1.38	0.12	1.18	1.58	0.1108	No
		4	Human	27	1.33	0.11	1.18	1.52		
4	Cs-137	12	UAV	34	1.3	0.12	1.11	1.56	**0.00002**	**Yes**
		4	Human	33	1.49	0.13	1.26	1.7		
5	Co-60	12	UAV	35	1.36	0.15	1.15	1.63	**0.0008**	**Yes**
		4	Human	31	1.49	0.08	1.32	1.62		
6	Co-60	12	UAV	29	1.77	0.31	1.33	2.2	0.6456	No
		4	Human	28	1.72	0.29	1.32	2.28		
7	Am-241	12	UAV	32	2.48	0.93	1.53	4.27	0.9639	No
		4	Human	32	2.5	0.97	1.45	4.4		
8	Co-60	12	UAV	39	1.32	0.08	1.12	1.5	0.2038	No
		4	Human	32	1.35	0.09	1.19	1.55		
9	Am-241	12	UAV	58	2.05	1.06	1.1	4.72	0.3865	No
		4	Human	45	2.36	1.23	1.2	4.96		

$\alpha^* = 0.0056$, level of statistical difference for survey comparison to p-value, using equation 7 and a total of 9 tests.
n was determined based on the transect identification methodology covered in section 2.5.1.4.

4.0 Discussion

The primary research questions of interest evaluated were:

- Did observed UAV paths differ from human paths and, if so, by how much?
- Did survey path deviation affect survey results and, if so, how?
- Were radiological measurements from human and UAV surveys significantly different?

The results of the four scenarios analyzed demonstrated that the experimental design provided enough information to address the primary research questions. All the UAV and human survey paths were not statistically different with respect to the regression analysis (Table 12).

One of the concerns in the experimental design addressed in section 2.0 was whether the energy ranges of Am-241, Cs-137, and Co-60 (Table 1) could be detected by one NaI scintillation detector. The decision was made to conduct surveys with both the Ludlum and Alpha Spectra radiological detectors. There were no significant differences in the UAV and human surveys using the Ludlum radiological detector.

There were, however, considerable differences in the UAV and human surveys using the Alpha Spectra radiological detector. Out of all the paired UAV to human survey comparisons in the four scenarios (Table 14 and Table 16), only three comparisons were statistically different. The statistically different comparisons were all with the Alpha Spectra detector: Scenario 2, low altitude surveys over check source 9 (Am-241) (Table 15); and Scenario 4, high altitude surveys over check source 4 (Cs-137), and check source 5 (Co-60) (Table 17).

Appendix E includes further information on the Alpha Spectra performance. The Alpha Spectra detector is designed with a thin scintillation crystal of 0.04 in., which should be optimal for measuring the energy of Am-241. The differences between the UAV and the human surveys in scenario 2 were likely due to the velocity and paths of the detector over the check source (Table 15). Figure 17 shows the radiological counts for the UAV and human surveys over each check source. Check source 9 (Figure 17, lower right corner) has the greatest difference in the maximum radiological value (72.6 kcpm for UAV vs. 38.4 kcpm for human). Check source 9 has the greatest difference in the peak radiological measurement over the elapsed time, which is a function of the average velocity of the surveys by the UAV (0.19 m/s) and human (0.21 m/s).

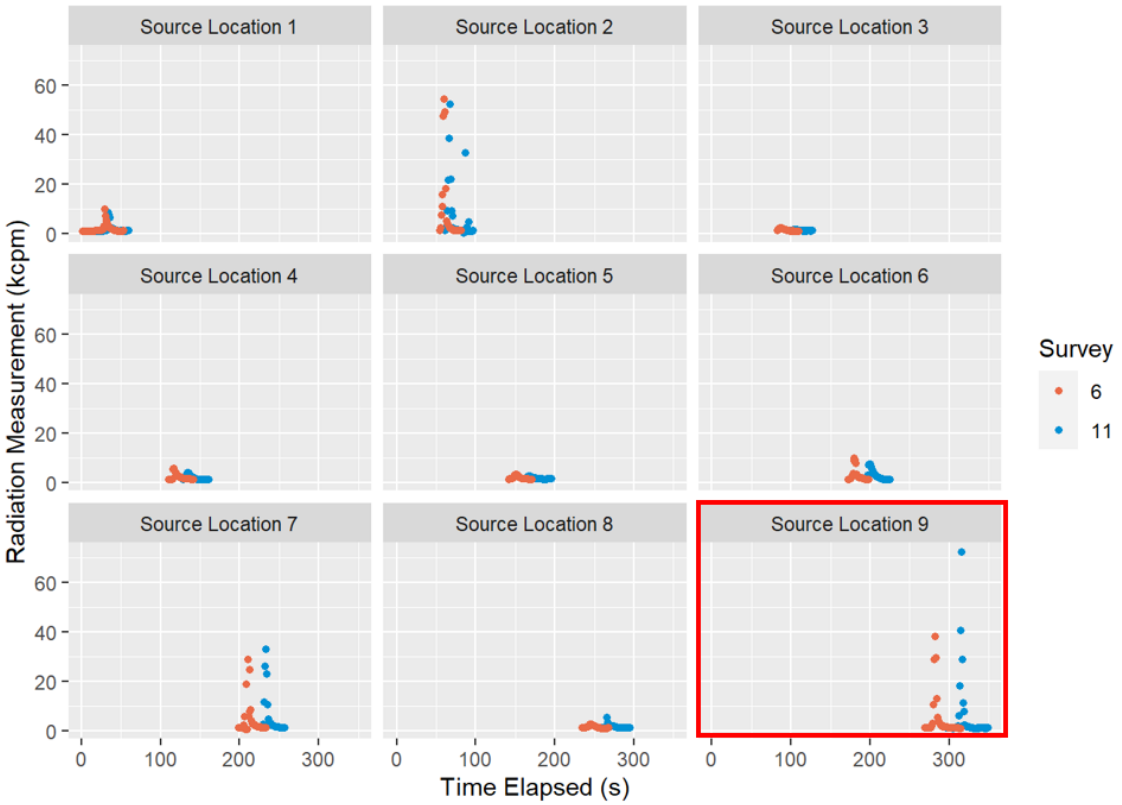

Figure 17. Comparison of Counts Rates for Scenario 2, the Alpha Spectra Radiological Detector for Surveys 6 (human) and Survey 11 (UAV), with Check Source 9 Highlighted in Red Box to Emphasize the Significant Difference in Results

The differences between the surveys in scenario 4 with respect to the Cs-137 check source 4 and Co-60 check source 5 was likely due to the high altitude and the challenge for the Alpha Spectra detector to measure their energy levels at those very low activity levels (Table 17). The regression analysis of the paths for the UAV and human surveys for Scenario 4 were not significantly different (Table 12). It must also be pointed out that the Alpha Spectra detector is not best suited for measuring high energy photons because of its limited detector thickness.

The median altitude for the UAV and human surveys for Scenario 4 were 96.6 and 105.4 cm, respectively (Table 11). Based on the MDCR evaluations, the activity of check source 4 (6.88 µCi Cs-137), 5 (5.39 µCi Co-60), and 8 (3.63 µCi Co-60) would be difficult to detect above 100 cm (Table 6).

Figure 18 illustrates the difference in the radiological activity measured for check source 4 (Cs-137) by the human (survey 4) and UAV (survey 12), as seen in the contrast of count rates for the two surveys (i.e., different shapes of the count rates by surveyor). Similarly, check source 5 (Co-60) also was significantly different during the same surveys as shown in Figure 19. While check source 8 (Co-60) could have been challenging, Figure 20 shows that the count rates for both the human and UAV surveys were much more similar and not significantly different compared to the count rates for check source 4 (Figure 18) and 5 (Figure 19).

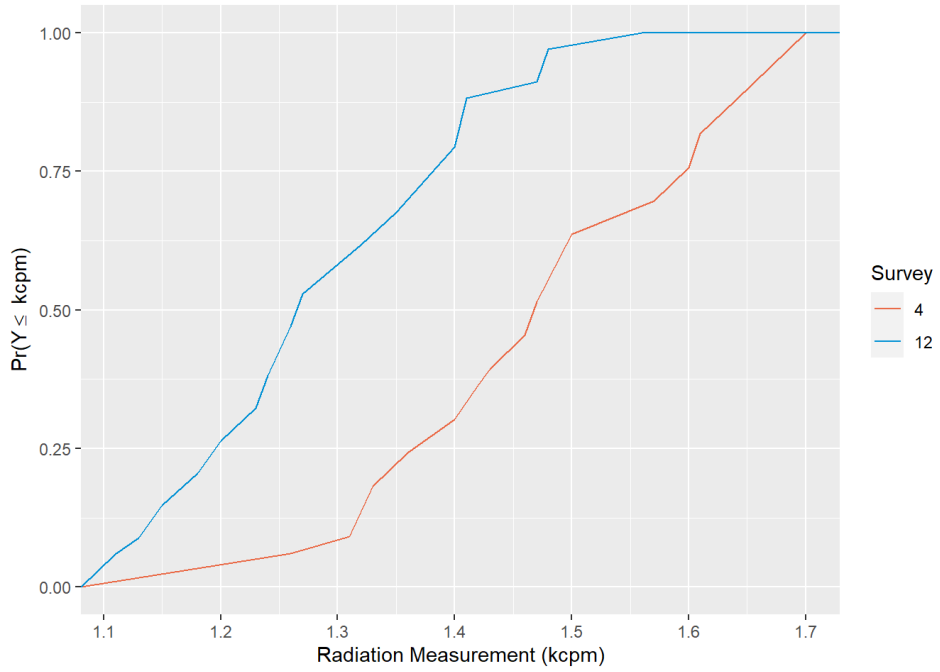

Figure 18. Empirical Cumulative Distribution Functions (eCDFs) for the Two-Sample K-S Test Showing a Significant Difference in Values (p = 0.00002) for Human (Survey 4) and UAV (Survey 12) Radiological Count Rate at Check Source 4

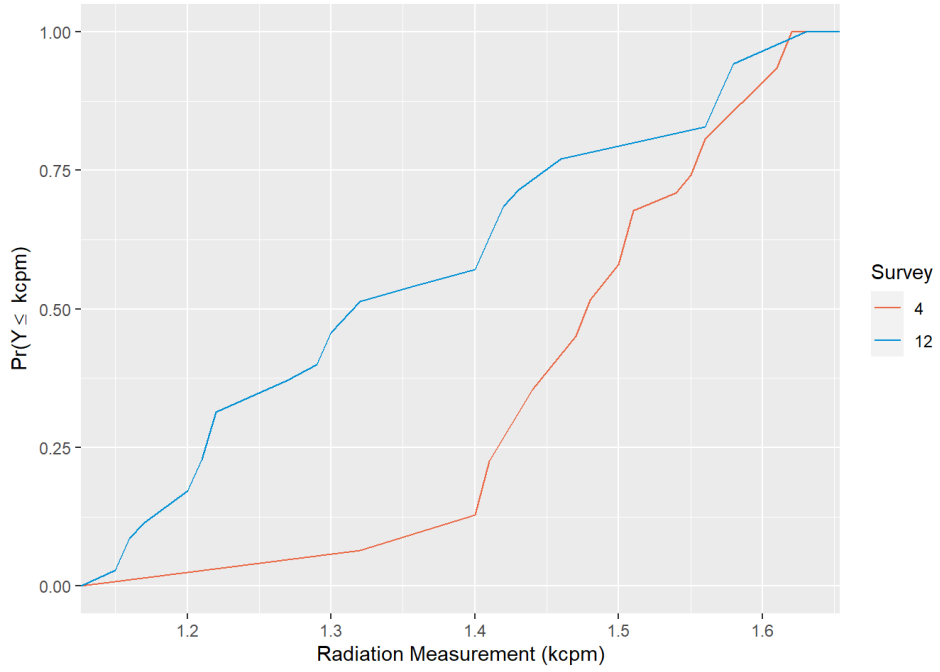

Figure 19. Empirical Cumulative Distribution Functions (eCDFs) for the Two-Sample K-S Test Showing a Significant Difference in Values (p = 0.0008) for Human (Survey 4) and UAV (Survey 12) Radiological Count Rate at Check Source 5

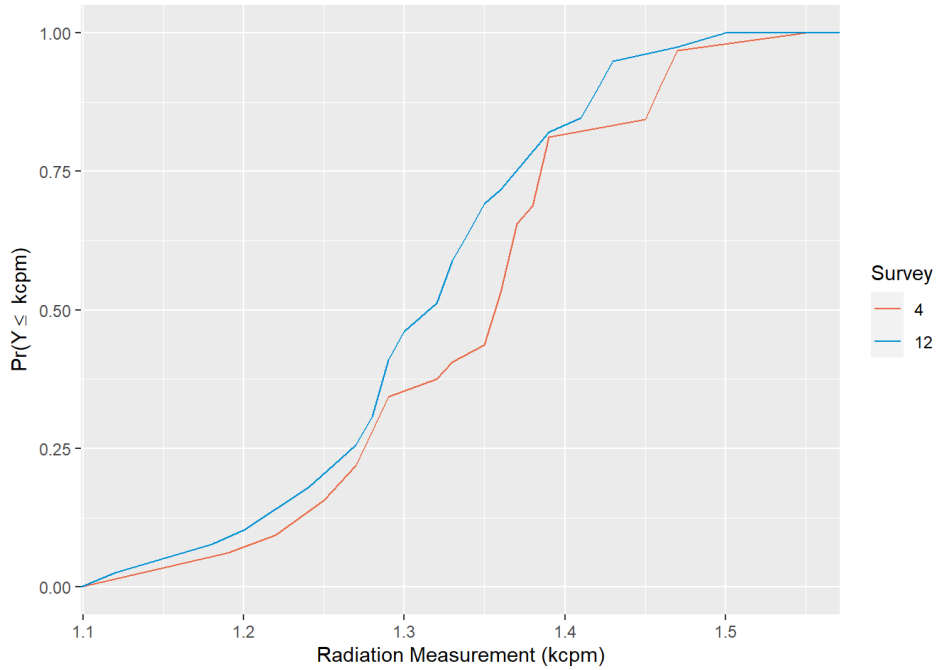

Figure 20. Empirical Cumulative Distribution Functions (eCDFs) for the Two-Sample K-S Test showing the Similarity (p = 0.2030) for Human (Survey 4) and UAV (Survey 12) Radiological Count Rate at Check Source 8

One limitation of this study was a limited scope and schedule that did not accommodate additional analyses of precision, accuracy, representativeness, and reproducibility of the measured radiological activities. Data from the background transects were not analyzed. A future study should consider additional data analysis using the existing data collected in this field study.

Evaluating MDCs and comparing the count rates from each detector to these values require further analysis and formulating assumptions to explicitly compare different units of measurements (e.g., pCi/g to kcpm). In future studies, evaluation of radiological detector performance in a stationary position and at altitudes much higher than that conducted in this field study would be informative.

5.0 Conclusion and Recommendations

The performance of the UAV and human surveys with two different detectors and two altitudes above nine check sources resulted in a robust proof-of-concept evaluation of alternative surveying techniques for decommissioning. However, the evaluation of radiological detectors with a commercially available UAV demonstrated that there are several areas of improvements before UAVs can be deployed systematically for collecting radiological measurements to support decommissioning efforts. In addition, it is worth pointing out that for this proof-of-concept study, the traditional human survey path (serpentine motion) was not followed.

Radiological detection of check sources was successfully demonstrated in this evaluation; however, the detection of dispersed radiological material or hotspots necessary for decommissioning surveys would be challenging without improvements to the radiological detectors and integration of supporting instrumentation. The areas of improvements include the configuration of radiological detectors for UAVs (especially for changing environmental conditions) and integration of instrumentation with radiation detection.

Radiation detection using UAVs has been evaluated for many uses, and commercially available systems are now available; however, detection of low radiation levels applicable to decommissioning efforts is not systematic. Several areas of improvement need to be addressed, such as:

- Altitude and velocity of the UAV compared to the response time and quality of the radiological measurements.
- Maneuverability of the UAV in changing environmental conditions.

UAV systems are challenged to fly low to the ground at slow velocities. Collision avoidance systems on UAVs are improving rapidly, to the extent that new models are available to negotiate within a facility and around furniture and infrastructure, yet these systems are small and cannot carry a payload for radiation detection. While the pilot and crew had experience with the Aurelia X6 navigation systems, difficulties were faced while flying the UAV at low altitude because of the avoidance detection algorithms for the navigation system. One consequence was the sudden rise in the UAV during a survey and the need for the pilot to reposition the UAV to the desired altitude (see the wide range of altitudes for the UAV surveys in Table 11). In an area with trees and changing vegetation, the Aurelia X6 would be challenged to maintain velocity and altitude for representative radiation measurements. More experience by the pilot and crew could improve results, yet development of new UAV systems would increase opportunities for further applications with the environmental conditions found at many sites undergoing decommissioning.

While there are numerous radiation detectors from which to choose for decommissioning activities (Appendix A), the selection of the NaI(Tl) scintillation detectors was based on professional experience. Response time is key for continuous surveying systems. Detector efficiency is directly related to response time (see DCGL and MDC calculations in Appendices B and C). Some radiation detection systems are delicate, under pressure, and/or require bulky support systems, all conditions that make the detectors difficult to accommodate on a UAV. The features of the Ludlum and Alpha Spectra NaI(Tl) scintillation detectors were adequate for the conditions evaluated in this work. It is recommended to conduct further research using various radiation detectors for UAV applications under decommissioning conditions and at field designs similar to that offered at PNNL's 3440 test track facility.

Weather is another challenge for UAV applications in radiation detection. Radiological detectors, including NaI scintillation detectors, are sensitive to moisture as well as environmental background level changes if there is rain. Current regulations by the Federal Aviation Administration (FAA) limit the flights of UAVs in high wind conditions for the obvious reason that winds can easily alter the flight path of relatively lightweight UAVs. The navigation systems for UAVs are also susceptible to weather changes. During one survey (which was not included in the evaluation of results), there was a sudden change in the barometric pressure that was not recognized in time by the lidar and navigation system, resulting in the UAV landing during a low altitude survey.

Integration of instrumentation for radiation detection is acknowledged in the most recent revision of NUREG-1507 (Abelquist et al. 2020) and becomes even more challenging for new survey options with autonomous systems. Knowing the position of radiological anomalies in a land area survey is critical to the decision for unrestricted release of a decommissioned facility. GPS and lidar systems are readily available in many configurations and sizes. The precision and accuracy of information has improved greatly over the last decade. Yet, one of the major issues for this study was ensuring the information on radiological detector position in all the surveys was collected in a representative fashion and linking the results to the output of the radiation detector. In order to use the same GPS system for both the UAV and human surveys, a cart was used to carry the Aurelia X6 during the human surveys. It must be pointed out that the cart does not perform in the same manner as a human for decommissioning surveys (King et al.2012; Abelquist 2014; Abelquist et al. 2020).

To further improve the UAV application for decommissioning, there are several next steps apparent from this proof-of-concept evaluation:

- Manufacturers can improve integration of instrumentation for both radiation detection and UAV systems that would address data collection:
  - Radiation data logging systems should be adaptable and collect information relative to the sensor. This evaluation was limited by the Ludlum 3000 data logger set to a minimum recording time of once per second.
  - GPS and lidar systems should be able to integrate with sensors, providing easier data collection. This evaluation required aligning the data from the radiological detectors and position systems by the time stamp of the independent instruments.
- Autonomous evaluations of radiation detection should be evaluated for decommissioning:
  - This evaluation only reported results by navigating the UAV with a pilot. The Aurelia X6, as well as other UAV models, can fly preset courses; however, additional safety evaluations to set up such flights was challenging for this proof-of-concept evaluation. Further opportunities to fly UAVs autonomously could improve radiation measurements at lower altitudes and slower velocities.
  - Accomplishing radiological evaluations with site conditions that are common at decommissioning sites could be achieved faster than human surveys if tandem autonomous systems were used. Tandem systems include multiple UAVs as well as UAVs with ground-based crawlers. Research in this area is ongoing, but it is not necessarily considering the low activity levels for decommissioning sites.
- Additional research to determine quality criteria of measured radiological activities. This evaluation was not able to complete the evaluation of precision, accuracy, representativeness, and reproducibility of the measured radiological activities, nor direct

comparison to DCGLs and MDCs. Such analyses would assist in determining how to optimize positioning of a radiation detector on a UAV for accurate radiological measurement results (this evaluation fixed the detector in a downward direction). In addition, the uncertainty of radiological measurements at higher altitudes and faster velocities could be assessed with determination of quality criteria.

- Once additional research and instrumentation improvements are complete, NRC could provide guidance on the compliance with UAV usage at decommissioning sites with consideration of aviation safety (FAA regulations) and security (e.g., E.O. 13981, and physical and cyber concerns).
- To demonstrate compliance with NRC's regulatory criteria for unrestricted release, additional research and a framework for UAV usage is required to be developed. Areas such as cybersecurity and data storage also need to be addressed in order to use UAVs in a field environment.

6.0 References

10 CFR 20.1402. *Code of Federal Regulations*, Title 10, Energy, Part 20, “Standards for Protection Against Radiation,” Section 1402, *Radiological Criteria for Unrestricted Use*.

10 CFR 50.82. *Code of Federal Regulations*, Title 10, Part 50, “Domestic Licensing of Production and Utilization Facilities,” Section 82, *Termination of License*.

10 CFR 50.83. *Code of Federal Regulations*, Title 10, Part 50, “Domestic Licensing of Production and Utilization Facilities,” Section 82, *Release of Part of a Power Reactor Facility or Site for Unrestricted Use*.

10 CFR Part 20, Subpart E. *Code of Federal Regulations*, Title 10, Energy, Part 20, “Standards for Protection Against Radiation,” Subpart E, Radiological Criteria for License Termination. U.S. Nuclear Regulatory Commission.

10 CFR Part 50. *Code of Federal Regulations*, Title 10, Energy, Part 50, “Domestic Licensing of Production and Utilization Facilities.” U.S. Nuclear Regulatory Commission.

Abelquist, E.W. 2014. *Decommissioning Health Physics—A Handbook for MARSSIM Users*, Second Edition, Taylor and Francis, Boca Raton, FL.

Abelquist, E.W., J.P. Clements, A.M. Huffert, D.A. King, T.J. Vitkus, and B.A. Watson. 2020. *Minimum Detectable Concentrations with Typical Radiation Survey for Instruments for Various Contaminant and Field Conditions*. NUREG-1507 Revision 1. U.S. Nuclear Regulatory Commission, Washington, D.C.

Aker, R. and C. Wood. 2005. *Maine Yankee Decommissioning Experience Report: Detailed Experiences 1997–2004*. EPRI Report ID 1011734. New Horizon Scientific, LLC. Naperville, Illinois.

Banovac, K.L., J.T. Buckley, R.L. Johnson, G.M. McCann, J.D. Parrott, D.W. Schmidt, J.C. Shepherd, T.B. Smith, P.A. Sobel, B.A. Watson, D.A. Widmayer, T.H. Youngblood. 2006. *Consolidated Decommissioning Guidance Decommissioning Process for Materials Licensees. Final Report*. NUREG-1757, Volume 1, Revision 2. U.S. Nuclear Regulatory Commission, Washington, D.C.

Barr, C.S., S. Clark, G.C. Chapman, J.P. Clements, D.W. Esh, R.W. Fedors, A.M. Huffert, L.A. Kauffman, M.M. LaFranzo, D.B. Lowman, C.A. McKenney, L.L. Parks, D.W. Schmidt, A.L. Schwartzman, and B.A. Watson. 2020. *Consolidated Decommissioning Guidance Characterization, Survey, and Determination of Radiological Criteria. Draft Report for Comment.* NUREG-1757, Volume 2, Revision 2. U.S. Nuclear Regulatory Commission, Washington, D.C.

Battelle. 2002. *Waste Characterization, Classification, and Shipping Support Technical Basis Document for Battelle Columbus Laboratories Decommissioning Project (BCLDP) West Jefferson North Facility*. Battelle, Columbus, OH.

CYAPCO. 2006. *Final Status Survey Final Report Phase IV*, Appendix A10, “Survey Unit Release Record 9106-0010, Discharge Canal.”

Daniel, W.W. 1990. *Applied Nonparametric Statistics*, 2nd edition. PWS-KENT Publishing Company, Boston, Massachusetts.

Entergy. 2014. *Vermont Yankee Nuclear Power Station: Radiological Historical Site Assessment*. Radiation Safety & Control Services, Stratham, New Hampshire.

King, D.A., N Altic, and C. Greer. 2012. "Minimum Detectable Concentration as a Function of Gamma Walkover Survey Technique." *Health Physics* 102 (Suppl 1): S22-S27. DOI: 10.1097/HP.0b013e318237e757

Lee, C. and H.R. Kim. 2019. "Optimizing UAV-based Radiation Sensor Systems for Aerial Surveys." *Journal of Environmental Radioactivity* 204: 76-85.

McGrath, R. 2006. *Connecticut Yankee Decommissioning Experience Report: Detailed Experiences 1996-2006*. EPRI, Palo Alto, CA: 2006. 1013511.

Millsap, W.J. and D.J. Brush. 2015. *Final Report on the Radiological Clearance of Land in the Southern 600 Area of the Hanford Site*. HNF-58917. Mission Support Alliance, Richland, Washington.

Naaman, M., 2021. "On the tight constant in the multivariate dvoretzky–kiefer–wolfowitz inequality." *Statistics & Probability Letters*, 173, p.109088

NRC. 2000. *Multi-agency Radiation Survey and Site Investigation Manual (MARSSIM)*. NUREG-1575, Revision 1. Washington, D.C.

O'Malley, K. and A. Bunn. 2021. *Key elements of a field study for the comparison of human and UAV radiological surveys for decommissioning radiological facilities*. PNNL-31808. Richland, WA: Pacific Northwest National Laboratory.

R Core Team (2021). R: A language and environment for statistical computing. R Foundation for Statistical Computing, Vienna, Austria. https://www.R-project.org/.

Ramos Pinto, L., A. Vale, Y. Brouwer, J. Borbina, J. Corisco, R. Ventura, A.M. Silva, A. Mourato, G. Marques, Y. Romanets, S. Sarento, and B. Goncalves. 2021. "Radiological Scouting, Monitoring and Inspection Using Drones." *Sensors* 21:3143- 3174. https://doi.org/10.3390/s21093143.

U.S. Army Corps of Engineers. 2006. Gamma Walkover Survey Plan for the Former Guterl Specialty Steel Corporation Lockport, New York.

Yankee Atomic Electric Co. 2004. *Yankee Nuclear Power Plant Site, Historical Site Assessment*. Volume 1. Rowe, Massachusetts. ML042510589.

Appendix A – Radiation Detector Evaluation

Gas-based detectors, solid-state detectors, and scintillation detectors were initially considered for this work (Glenn F Knoll 2010). However, scintillation detectors, specifically sodium iodide detectors, were determined to be the most appropriate for the initial unoccupied aerial vehicle (UAV) testing application.

A.1 Gas-based Detectors

Gas-based scintillators are one of the earliest forms of radiation detectors. These detectors generally feature an anode metallic wire in the center. A voltage potential is applied across the wire, and the external surface acts in the capacity of the cathode. The detector tube is filled with an ionizable gas like argon, neon, or helium, this gas acts in the capacity of a detection medium. Depending on the voltage potential subjected across the anode and cathode, this detector can act as either an ionization, proportional, or Geiger counter. It must, however, be noted that for detecting high energy photons, a gas medium is not the best option, owing to its low interaction cross section. Other variations of the gas-based systems are available that employ pressurized gas, resulting in an increase in the detection efficiency. The challenge in using this approach is that, from a safety standpoint, a hard landing of the drone or any unforeseen event might result in the loss of integrity of the high-pressure detection system and cause potential injury/harm to people/property in the area.

Although gas-based detectors can be manufactured in large sizes and their efficiency can also be increased by subjecting them to pressure, these systems have a slow response time compared to scintillators, and there is always a potential for physical damage to the detection system.

A.2 Solid-state Detectors

The next radiation detection technology is solid-state detectors. These detectors use a semiconductor media to detect radiation. The most prominent form of solid-state detectors are high purity germanium detectors (HPGe). These detectors have sub 0.5% energy resolution for the 662 keV peak but suffer from poor detection efficiency and require a continuous cooling mechanism. Other semiconductor technologies like Cadmium Zinc Telluride (CZT) are being widely used and are well known to achieve an energy resolution under 2% at room temperature operation. Growing these crystals in large sizes without significant defects is a challenging process and is relatively expensive compared to conventional scintillation detectors. Moreover, for this application, it is desirable to use a relatively large sized detector to increase the overall detection efficiency.

It was decided that semiconductor detection technology was not ideal for our application because most of the semiconductors can’t be grown in sizes comparable to traditional scintillation crystals, and moreover, with the current state-of-the-art technologies, semiconductors still prove to be expensive. The small size of the crystals and low detection efficiency is a challenge that is required to be overcome for application in decommissioning purposes. It must, however, be noted that with improvements in crystal growth/detector development technologies, it might be possible to use gas or semiconductor-based technologies for this purpose in the future.

A.3 Scintillation Detectors

Scintillators are a class of radiation detectors that emit photons in the optical/near-UV range of the spectrum upon interaction with ionizing radiation. Sodium iodide (NaI) or cesium iodide (CsI) are some of the most widely used radiation detectors. Several other scintillation media have been developed over the years, like strontium iodide (SrI_2), barium fluoride (BaF_2), lanthanum bromide ($LaBr_3$), and cadmium tungstate ($CdWO_4$), but they have not been widely adopted. Scintillators generally require a mechanism to convert the optical photons into measurable electrical signals; this task is accomplished using photomultiplier tubes (PMTs) or silicon photomultiplier (SiPMs). Traditional scintillators like NaI or CsI can be grown in large sizes and are easily available. These types of detectors have also been used for many decades and are very reliable. Although these detection media are brittle and must be handled with appropriate casing, several crystals and PMT housings are available that allow for safe operation of these devices under various environments. It is worth mentioning that organic scintillators were not used in this work because of their relatively low interaction cross section compared to inorganic scintillators.

A.4 Summary

The opportunities for using new detection media are quickly evolving. The selection of the NaI scintillation detectors for this evaluation was influenced by conversations with leading radiation detector manufacturers at the 66th Annual Meeting of The Health Physics Society, held between July 25 and July 29, 2021. PNNL radiation detector experts discussed with the manufacturers the conditions of the UAV flight and suitable detectors that might meet these conditions. The discussions considered:

- Robustness of the detector if the UAV were to strike an object.
- Safety considerations, e.g., whether detectors that are under high pressure could meet worker health and safety concerns.
- Weight of the detector, especially with those requiring bulky support systems.
- Response time and detector efficiencies.

Collectively, the discussions led to the decision to use the typical NaI scintillation detectors that are commonly used now for decommissioning surveys.

A.5 References

Glenn F Knoll. 2010. *Radiation Detection and Measurement*. John Wiley & Sons, Inc.

Appendix B – Activity of Radioactive Point Sources

B.1 Introduction

In this evaluation of the feasibility of using unoccupied aerial vehicles (UAVs) for performing external radiation surface surveys for decommissioning, calculations were made to determine what activity was needed to simulate external dose or exposure rates from large areas of soil with residual radioactivity in the surface layer (15 cm) representing the derived concentration guideline levels (DCGLs) or authorized limits for clearance. DCGLs are concentrations of residual radionuclides in soil that result in a selected annual dose from a particular exposure scenario. The radionuclides of interest for this project are gamma emitters Am-241, Cs-137, and Co-60, and beta-emitter Sr-90.

B.2 DCGLs/Authorized Limits

DCGLs are authorized limits for an annual dose of 25 mrem/year that were determined using the approach for the clearance of the Research Technology Laboratory (RTL) site on the Pacific Northwest National Laboratory (PNNL) campus (Ikenberry 2016), which used the RESRAD-ONSITE code, version 7.2 (ANL 2016). Of the radionuclides of interest for this work, only Co-60 had an authorized limit previously developed for RTL clearance. DCGLs or authorized limits were needed to be developed for Am-241, Cs-137, and Sr-90. Co-60 was first analyzed using RTL parameters to verify that the same value could be calculated. Unit dose factors (mrem/year per pCi/g) for the limiting suburban scenario and more complex agricultural scenario were verified to be within 0.1 mrem of the authorized limits calculated for RTL. Slight differences seemed to be from minor changes in the external dose conversion factors between the code versions used.

Unit dose factors and DCGLs were calculated for both suburban and agricultural scenarios, shown in Table B.1. The agricultural scenario is typically the most limiting, particularly for more soluble radionuclides. Radionuclides were assumed to be present in the upper 15 cm of soil, providing mechanisms of exposure to suburban and agricultural residents.

Table B.1. Derived Concentration Guideline Levels or Authorized Limits for the Radionuclides of Interest

	Unit dose factors (mrem/yr per pCi/g)		DCGL/Authorized Limit (pCi/g)	
Radionuclide	**Suburban**	**Agricultural**	**Suburban**	**Agricultural**
Co-60	6.64	6.65	3.8 (3.77)	3.8 (3.76)
Cs-137	1.82	1.86	14 (13.7)	13 (13.4)
Am-241	0.045	0.068	560 (556)	370 (368)
Sr-90	0.126	0.491	200 (198)	50 (51)

B.3 External Radiation Levels at the DCGL in Soil

Radionuclides were assumed to be in the upper 15 cm of soil over a large enough area (4,800 m^2, 1.2 acres) that could be modeled as an infinite slab using MicroShield™ Version 9.06 (Grove Software, Inc. 2013). This represented a uniform concentration of residual radionuclides in the soil at the DCGL. The external exposure rates (mR/hr) were determined at 30 cm,

100 cm, and 200 cm (1 to 6.5 feet) above the soil surface for unit concentrations of 1 pCi/g. Soil density was set to 1.6 g/cm^3. MicroShield™ can determine exposure rates from gamma-emitting radionuclides, so Sr-90, a beta-emitting radionuclide, was not included.

External exposure rates from radionuclides (Table B.2) at the DCGLs range from 5 to 7 µR/hr. If a normal external background exposure rate is in the range of 8–10 µR/hr, these levels represent a 50 to 90% increase in the external radiation level. In areas where background exposure rates could be higher, the relative increase above background would be lower and more difficult to distinguish. Characterizing the site-specific background is an important consideration in this work.

Table B.2. External Exposure Rates from Residual Radionuclides in Soil at the Respective DCGL

		External Exposure Rate, µR/hr (with buildup)		
Radionuclide	**DCGL (pCi/g)**	**30 cm**	**100 cm**	**200 cm**
Co-60	3.8	6.9	6.8	6.7
Cs-137	13	6.4	6.3	6.2
Am-241	370	5.8	5.6	5.4

Alternate method for Sr-90. Unlike the gamma-emitting radionuclides, the external exposure pathway represents only about 5% of the dose from the agricultural resident scenario for Sr-90. A beta version of RESRAD-BUILD (version 3.8.7.0) acquired from Argonne National Laboratory was used to estimate the external dose rate from Sr-90/Y-90 in surface soil. At 30 cm, the dose rate was estimated to be 1.3×10^{-4} µrem/hr per pCi/g, or 6.6×10^{-3} µrem/hr at the agricultural resident DCGL of 50 pCi/g. This level, about 1,000 lower than the gamma emitters in Table B.2, would be indistinguishable from detector background.

B.4 Determining Point Source Activity

MicroShield™ was run for 1 pCi point source activities of Co-60, Cs-137, and Am-241. The ratio was then determined for the 1 pCi/g infinite slab exposure rate to a 1 pCi point source exposure rate at distances of 30 cm, 100 cm, and 200 cm from each source. The infinite slab exposure rate is on the order of a million times higher than point source activity for the same unit activity (pCi/g and pCi). Table B.3 shows the exposure rate ratios at the limiting DCGLs for each radionuclide and the point source activity to simulate residual radioactivity in soil.

Table B.3. Ratio of External Exposure Rates from Residual Radionuclides in Soil Using a Plane and Point Source at the Respective DCGL

		Ratio of Exposure Rates Infinite Plane/Point Source			Point Source Activity (µCi)		
Radionuclide	**DCGL (pCi/g)**	**30 cm**	**100 cm**	**200 cm**	**30 cm**	**100 cm**	**200 cm**
Co-60	3.8	4.8 E5	5.2 E6	2.1 E7	0.5	5	20
Cs-137	13	1.7 E6	1.9 E7	7.5 E7	2	20	75
Am-241	370	2.6 E6	3.1 E7	1.4 E8	3	30	140

Figure B.1 shows the data in Table B.3 plotted graphically, with trendlines and equations to interpolate or extrapolate point source activities at distances different from the distances selected. These data and curves are directly dependent upon the selected soil concentration (DCGL), so changes in soil concentration would require re-calculations of point source activity. The infinite slab exposure rates do not vary much over these distances, but the point source exposure rates change significantly, varying as the inverse square law ($1/d^2$). In field application, the ground to drone distance would not be critical for large area sources, but it would be important during testing with point source.

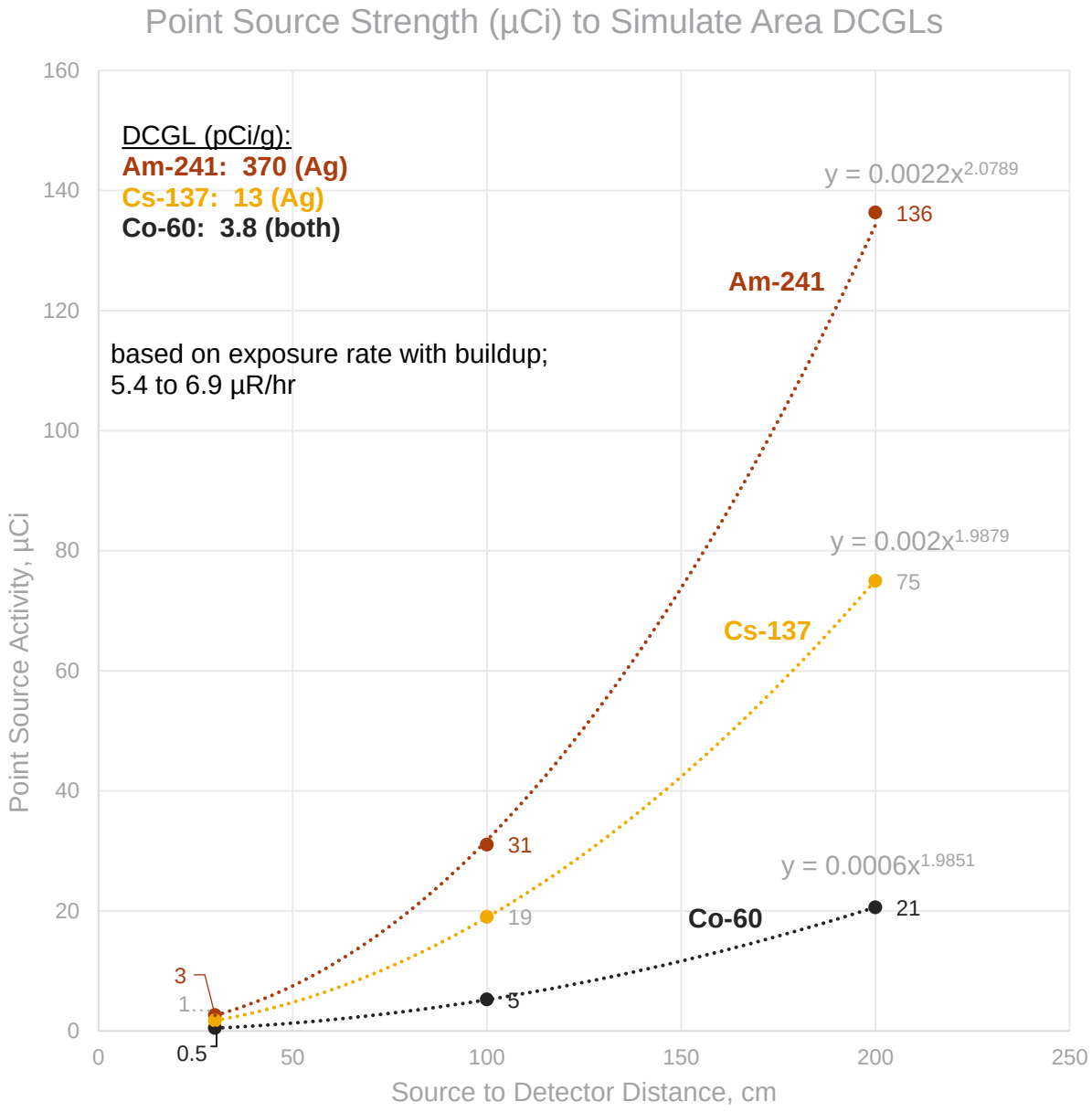

Figure B.1. Point Source Activity Simulating Exposure Rates from Residual Soil Activity at Specific DCGLs

B.5 References

Argonne National Laboratory (ANL). 2016. RESRAD-ONSITE for Windows. Version 7.2, July 20, 2016.

Argonne National Laboratory (ANL). RESRAD-BUILD for Windows. Version 3.8.7.0 Beta. Email from Jing-Jy Cheng, ANL, to Tracy Ikenberry, PNNL, July 19, 2021.

Grove Software, Inc. (2013). MicroShield™. Version 9.06. Radiationsoftware.com.

Ikenberry, TA. 2016. *Authorized Limits for Radiological Clearance of the Research Technology Laboratory (RTL) Site*. DMA-TR-063. Dade Moeller & Associates, Inc., Richland, WA for PNNL.

Ikenberry, TA. 2016. *Supplement: RESRAD Version 7.2 Summary Output Files for Authorized Limits for Radiological Clearance of the Research Technology Laboratory (RTL) Site*. DMA-TR-063S. Dade Moeller & Associates, Inc., Richland, WA for PNNL.

Appendix C – Radionuclide Exposure Rate-to-Concentration Ratios

C.1 Introduction

Determining the a priori minimum detectable concentration (MDC) is an important prerequisite for testing the feasibility of unoccupied aerial vehicles (UAVs) to conduct radiological surveys for decommissioning. An important parameter in the MDC equation is the exposure rate-to concentration ratio (ERC).[1] The results and method for determining the ERC for Cs-137, Co-60, and Am-241 are presented here, as well as similar results for check sources containing the same total activity as the soil column used to determine the ERC values.

C.2 Methods

The basis for the method of determining ERC is found in section 6.2.5 "*A Priori* Scan MDCs for Land Areas" of NUREG-1507 (Abelquist et al. 2020). Radionuclides were assumed to be uniformly distributed at a concentration of 1 pCi/g in a cylinder of soil 15 cm thick with end area of 0.25 m^2 (radius = 28.21 cm). The exposure rates at distances of 10, 20, 30, 60, and 100 cm above the center and at the edges of the cylinder were modeled using MicroShield™ Version 9.06 (Grove Software, Inc., 2013). Figure C.1 shows a representation of the soil column modeling geometry. Soil density of 1.6 g/cm^3 was used,[2] resulting in a required code input of 1.6 pCi/cm^3. Calculations were performed separately for Cs-137 (Ba-137m), Co-60, and Am-241. Total activity in the soil column (3.75×10^4 cm^3) was about 0.06 µCi.

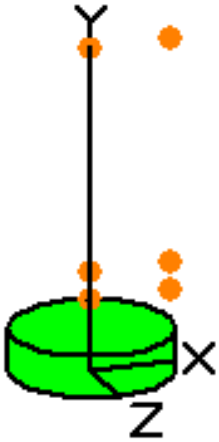

Figure C.1. Geometric Representation of Exposure Points above the Center and Edge of a Soil Column

Similar modeling and calculations were done using check sources to be used in the initial testing of the drone survey capabilities. Check sources were also assumed to be a cylinder geometry, 0.02 cm thick with a radius of 0.1 cm. Density was set at 1.6 g/cm^3. Calculations were performed separately for Cs-137 (Ba-137m), Co-60, and Am-241. Total activity in each case

[1] The ERC is exposure rate-to-concentration ratio (units of µR/hr per pCi/g), defined for a specific distance, source geometry and gamma-emitting radionuclide.
[2] NUREG-1507, Revision 1 used concrete as the medium; there was no difference in results with soil at 1.6 g/cm^3.

was the same as for the soil column, 0.06 µCi. Figure C.2 shows a representation of the check source modeling geometry. Exposure points were 10, 20, 30, 60, and 100 cm directly above and 28 cm offset from the center, providing direct comparison to the soil column results.

Figure C.2. Geometric Representation of Exposure Points above the Check Source

C.3 Results

ERC values for soil columns (ERC_{soil}) and check sources (ERC_{check}) were determined for Cs-137, Co-60, and Am-241. These results are presented in the following sections.

C.3.1 Cesium-137

Values for Cs-137 are presented in Table C.1 and Table C.2, calculated at points directly above the center of the soil column and check source, and at a point at the edge of the soil column (28 cm from the center). The calculated value for ERC_{soil} at 10 cm elevation is identical to the value presented in NUREG-1507 (Abelquist et al. 2020), providing qualitative verification of the result and method for Cs-137 and other radionuclides.

Table C.1. Cs-137 ERC_{soil} Values at Variable Heights Above the Soil Column (0.06 µCi Total Activity)

Vertical Distance (cm)	ERC at Center (µR/hr per pCi/g)	Vertical Decrease	ERC at Edge (µR/hr per pCi/g)	Change from Center to Edge (28 cm)
10	*0.248*[a]	-	0.137	55%
20	0.142	57%	0.092	64%
30	0.089	36%	0.063	72%
60	0.032	13%	0.027	86%
100	0.013	5%	0.012	93%

[a]Same as value reported in NUREG-1507 (Abelquist et al. 2020).

Table C.2. Cs-137 ERC_{check} Values at Variable Heights above the Check Source (0.06 µCi Activity)

Vertical Distance (cm)	ERC at Center (µR/hr per pCi/g)	Vertical Decrease	ERC at edge (µR/hr per pCi/g)	Change from Center to Edge (28 cm)
10	2.00	-	0.23	11%
20	0.50	25%	0.17	34%
30	0.22	11%	0.12	53%
60	0.06	2.8%	0.05	82%
100	0.02	1.0%	0.02	93%

Table C.3 shows the ratios between the Cs-137 ERC_{check} and ERC_{soil} values for easier application during testing. Figure C.3 shows graphically how the Cs-137 ERC_{check} and ERC_{soil} values change as a function of distance.

Table C.3. Ratios between Cs-137 ERC_{check} and ERC_{soil} Values at the Center and at the Edge (28 cm)

Vertical Distance (cm)	Check Source/ Soil Column Ratio in Center	Check Source/ Soil Column Ratio at Edge
10	8.1	1.7
20	3.5	1.9
30	2.5	1.9
60	1.8	1.7
100	1.5	1.5

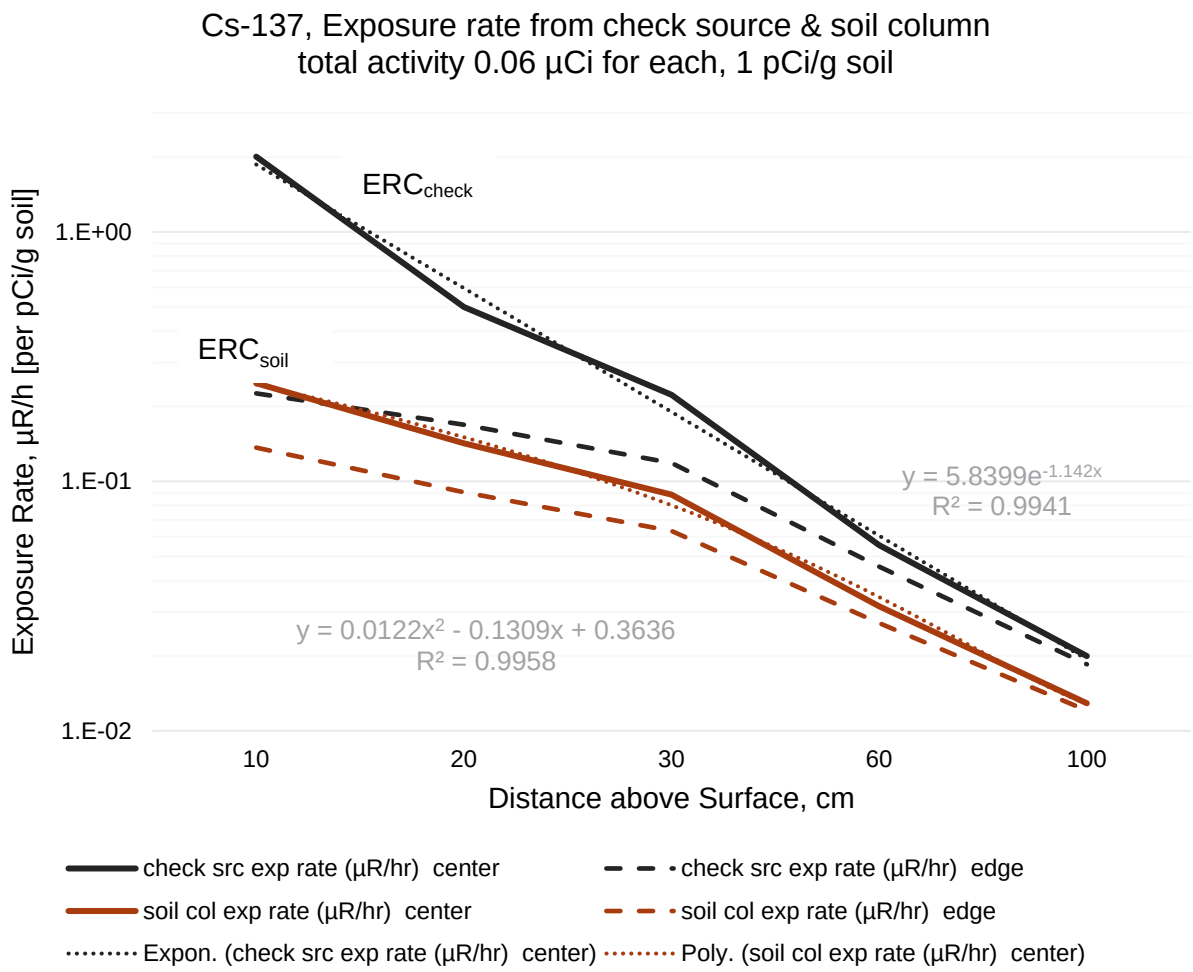

Figure C.3. Visual Representation of the Cs-137 ERC_{check} and ERC_{soil} as a Function of Distance

C.3.2 Cobalt-60

Values for Co-60 are presented in Tables C.4 and C.5; these are calculated at points directly above the center of the soil column and check source, and represent a point at the edge of the soil column 28 cm from the center.

Table C.4. Co-60 ERC_{soil} Values at Variable Heights above the Soil Column (0.06 µCi Total Activity)

Vertical Distance (cm)	ERC at center (µR/hr per pCi/g)	Vertical Decrease	ERC at Edge (µR/hr per pCi/g)	Change from Center to Edge (28 cm)
10	1.01	-	0.57	56%
20	0.58	57%	0.37	64%
30	0.36	35%	0.26	72%
60	0.13	13%	0.11	86%
100	0.052	5.2%	0.049	94%

Table C.5. Co-60 ERC_{check} Values at Variable Heights above the Check Source (0.06 µCi Activity)

Vertical Distance (cm)	ERC at center (µR/hr per pCi/g)	Vertical Decrease	ERC at Edge (µR/hr per pCi/g)	Change from Center to Edge (28 cm)
10	7.8	-	0.88	11%
20	1.9	25%	0.66	34%
30	0.88	11%	0.46	53%
60	0.22	2.8%	0.18	82%
100	0.078	1.0%	0.072	93%

Table C.6 shows the ratios between the Co-60 ERC_{check} and ERC_{soil} values for easier application during testing. Figure C.4 shows graphically how the Co-60 ERC_{check} and ERC_{soil} values change as a function of distance.

Table C.6. Ratios between Co-60 ERC_{check} and ERC_{soil} Values at the Center and at the Edge (28 cm)

Vertical Distance (cm)	Check source/Soil column ratio in center	Check source/Soil column ratio at edge
10	7.7	1.5
20	3.4	1.8
30	2.4	1.8
60	1.7	1.6
100	1.5	1.5

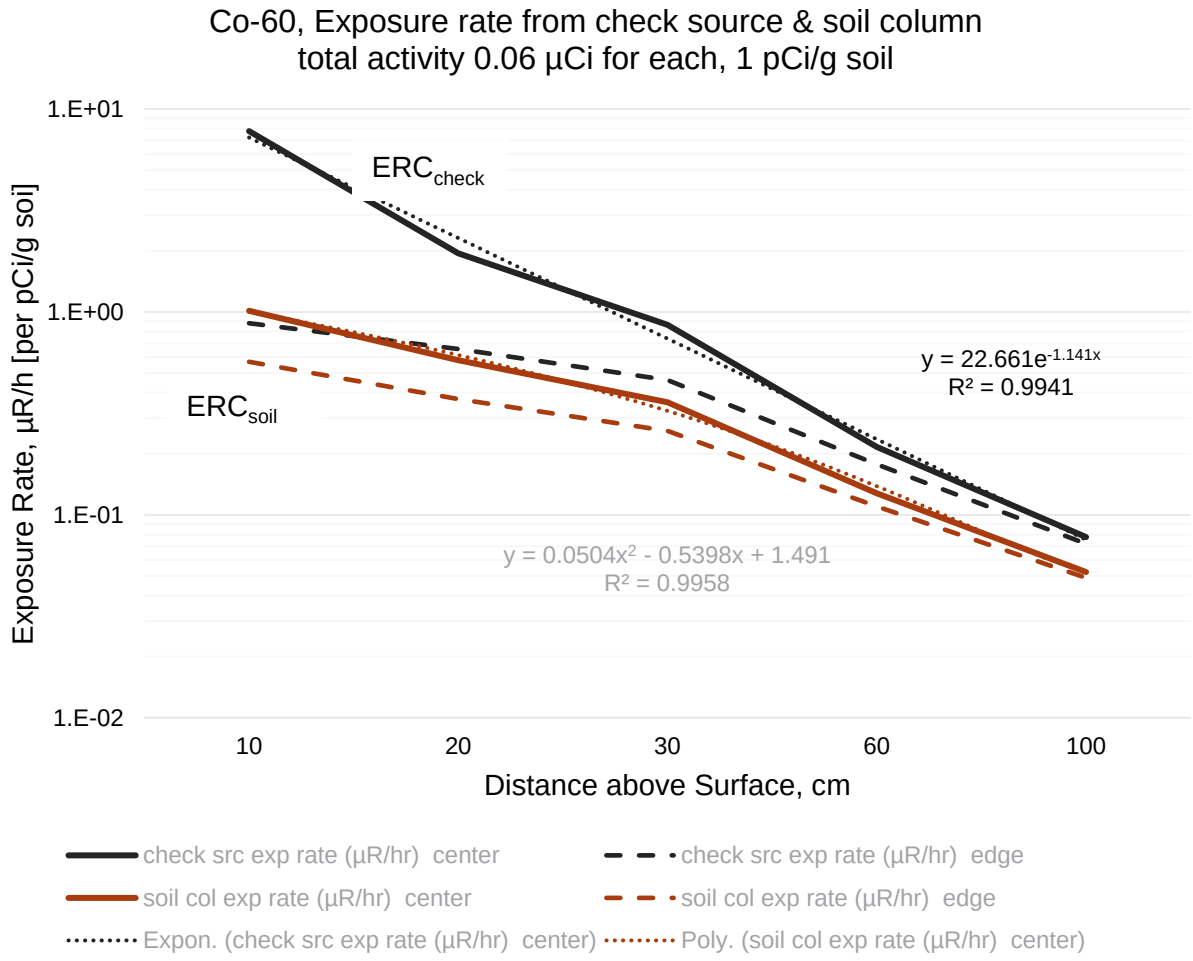

Figure C.4. Visual Representation of the Co-60 ERC_{check} and ERC_{soil} as a Function of Distance

C.3.3 Americium-241

Values for Am-241 are presented in Tables C.7 and C.8, calculated at points directly above the center of the soil column and check source, and representing a point at the edge of the soil column 28 cm from the center. ERC_{soil} values for Am-241 in soil are much lower than for Cs-137 and Co-60 because of attenuation of the low energy gamma rays within the soil column.

Table C.7. Am-241 ERC_{soil} Values at Variable Heights above the Soil Column (0.06 µCi Total Activity)

Vertical Distance (cm)	ERC at Center (µR/hr per pCi/g)	Vertical Decrease	ERC at Edge (µR/hr per pCi/g)	Change from Center to Edge (28 cm)
10	4.7E-03	-	2.0E-03	42%
20	2.9E-03	62%	1.4E-03	49%
30	1.8E-03	39%	1.0E-03	56%
60	6.4E-04	14%	4.6E-04	73%
100	2.5E-04	5.4%	2.1E-04	83%

Table C.8. Am-241 ERC_{check} Values at Variable Heights above the Check Source (0.06 µCi activity)

Vertical Distance (cm)	ERC at Center (µR/hr)	Vertical Decrease	ERC at Edge (µR/hr)	Change from Center to Edge (28 cm)
10	1.07	-	0.098	9.1%
20	0.26	25%	0.081	31%
30	0.12	11%	0.058	51%
60	0.028	2.6%	0.022	81%
100	0.0093	0.9%	0.0086	92%

Table C.9 shows the ratios between the Am-241 ERC_{check} and ERC_{soil} values for easier application during testing. Figure C.5 shows graphically how the Am-241 ERC_{check} and ERC_{soil} values change as a function of distance. Because of the much lower gamma energies of Am-241 and attenuation in the soil column, the comparison between soil column and check source is not nearly as close as for Cs-137 and Co-60.

Table C.9. Ratios between Am-241 ERC_{check} and ERC_{soil} Values at the Center and at the Edge (28 cm)

Vertical Distance (cm)	Check Source/Soil Column Ratio in Center	Check Source/Soil Column Ratio at Edge
10	230	50
20	92	58
30	63	57
60	43	48
100	37	41

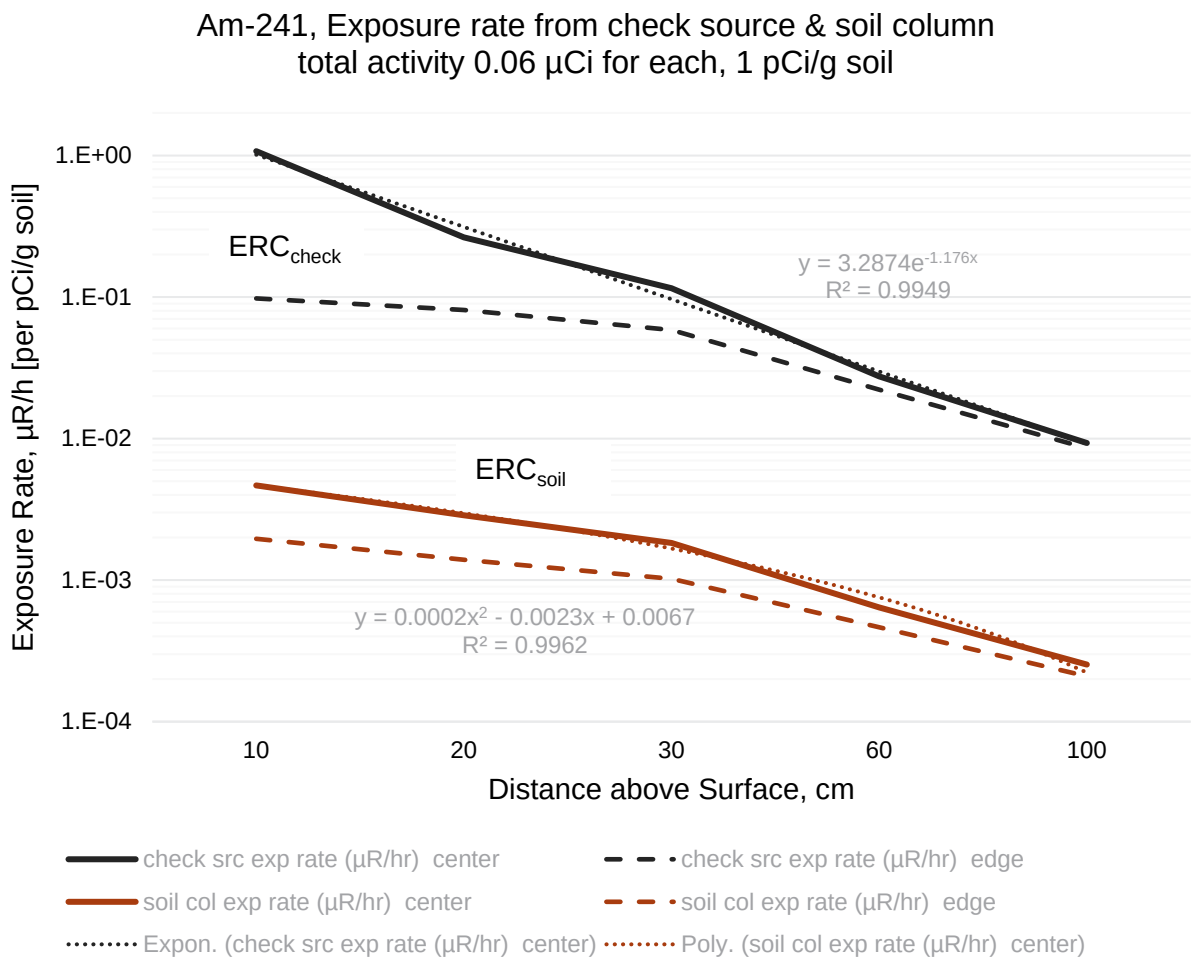

Figure C.5. Visual Representation of the Am-241 ERC_{check} and ERC_{soil} as a Function of Distance

C.4 Summary

ERC values have been calculated for Cs-137, Co-60, and Am-241 to assist in determining the minimum detectable concentrations (MDC) for scanning in testing of drones for external radiation scanning survey capability. Unit concentrations of 1 pCi/g were used to determine ERCs in µR/hr. ERC values were also determined for check sources of these radionuclides using the same method and the same total activity.

C.5 References

Grove Software, Inc. 2013. MicroShield™. Version 9.06. https://www.radiationsoftware.com.

Abelquist, E.W., J.P. Clements, A.M. Huffert, D.A. King, T.J. Vitkus, and B.A. Watson. 2020. *Minimum Detectable Concentrations with Typical Radiation Survey for Instruments for Various Contaminant and Field Conditions*. NUREG-1507 Revision 1. U.S. Nuclear Regulatory Commission, Washington, D.C.

Appendix D – Background Measurements and Calculations

Testing of the radiation detectors was performed prior to conducting surveys. In addition, background radiological measurements were also collected.

D.1 Lab Testing

The Ludlum and the Alpha Spectra detectors were characterized in an indoor lab facility. Am-241 and Co-60 sources were used to perform this initial characterization. The data logger was also tested in the lab environment to understand the various functionalities. End-to-end tests were performed involving the following steps:

- Connecting the cable and turning on the detector.
- Observing the initial background count rate.
- Turning on the data logging functionality.
- After a set amount of time, turning off the recording functionality.
- Powering down the detection system.
- Connecting the data logger to the laptop/PC and transferring the log file.
- Checking if the appropriate data was written in the log file.

Repeating these steps several times helped to establish the robustness of the detector and the data logger. This was followed by collecting lab level background data and source detector response as a function of distance. The background data collected using the Ludlum and the Alpha Spectra detectors as a function of distance from the benchtop are presented in Table D.1.

Table D.1. Background Count Rate as a Function of Distance for the 2 in. × 2 in. Ludlum and 2 in. × 0.04 in. Alpha Spectra Detectors

NaI(Tl) Detector	Distance from benchtop (cm)	counts per minute (cpm)
Ludlum	10	6210
Alpha Spectra	10	701
Ludlum	20	6380
Alpha Spectra	20	742
Ludlum	50	6860
Alpha Spectra	50	990

It was noted that a consistent increase in count rate was observed as the distance between the benchtop and the detector was increased. Since this lab space was surrounded by high activity cesium and californium wells that were active, some portion of the background counts can be attributed to these sources.

D.2 Field Testing

After successfully performing measurements at an indoor location, field testing was conducted to record the background data. This testing was conducted at variable locations at PNNL's 3440

test track. Data was collected for a period of 15 minutes at each location using both the Ludlum and the Alpha Spectra detectors. The locations where data was collected is presented in Figure D.1.

Figure D.1. Locations Where Data was Collected at the PNNL's 3440 Test Track

The background data was collected at the center of the test facility using both detectors (Ludlum and Alpha Spectra) at 20 and 50 cm height from the ground. At the other four locations, background data was collected using both detectors at 50 cm height. An adjustable lab support ring was used to change the height of the detector from the ground. The averaged background count rate data in terms of cpm at each location is presented in Table D.2.

Table D.2. Background Count Rates as a Function of Distance at Various Locations

NaI(Tl) Detector	Location	Height (cm)	Count rate (kcpm)
Ludlum (2 in x 2 in)	Center	20	7.80
Alpha Spectra (2 in x 0.04 in)	Center	20	1.29
Ludlum (2 in x 2 in)	Center	50	7.87
Alpha Spectra (2 in x 0.04 in)	Center	50	1.29
Ludlum (2 in x 2 in)	North	50	7.82
Alpha Spectra (2 in x 0.04 in)	North	50	1.22
Ludlum (2 in x 2 in)	East	50	6.81
Alpha Spectra (2 in x 0.04 in)	East	50	1.06
Ludlum (2 in x 2 in)	South	50	6.84
Alpha Spectra (2 in x 0.04 in)	South	50	1.02
Ludlum (2 in x 2 in)	West	50	6.73
Alpha Spectra (2 in x 0.04 in)	West	50	1.03

Appendix E – Statistical Results

This appendix provides the detailed data analysis figures for each survey scenario. The K-S test results have an α* value of 0.0056 for comparison to the p-values for each of the results for check sources by survey.

E.1 Summary of Radiation Measurements for all Experimental Surveys

The following figures show the experiment data from the data logger without data processing as discussed in section 2.5.1. Radiation measurements (as expressed on the y-axis in kcpm) may include the high activity response from the reference check source at the beginning and end of the recording for that survey. Only the surveys with the green borders were used further in analyses.

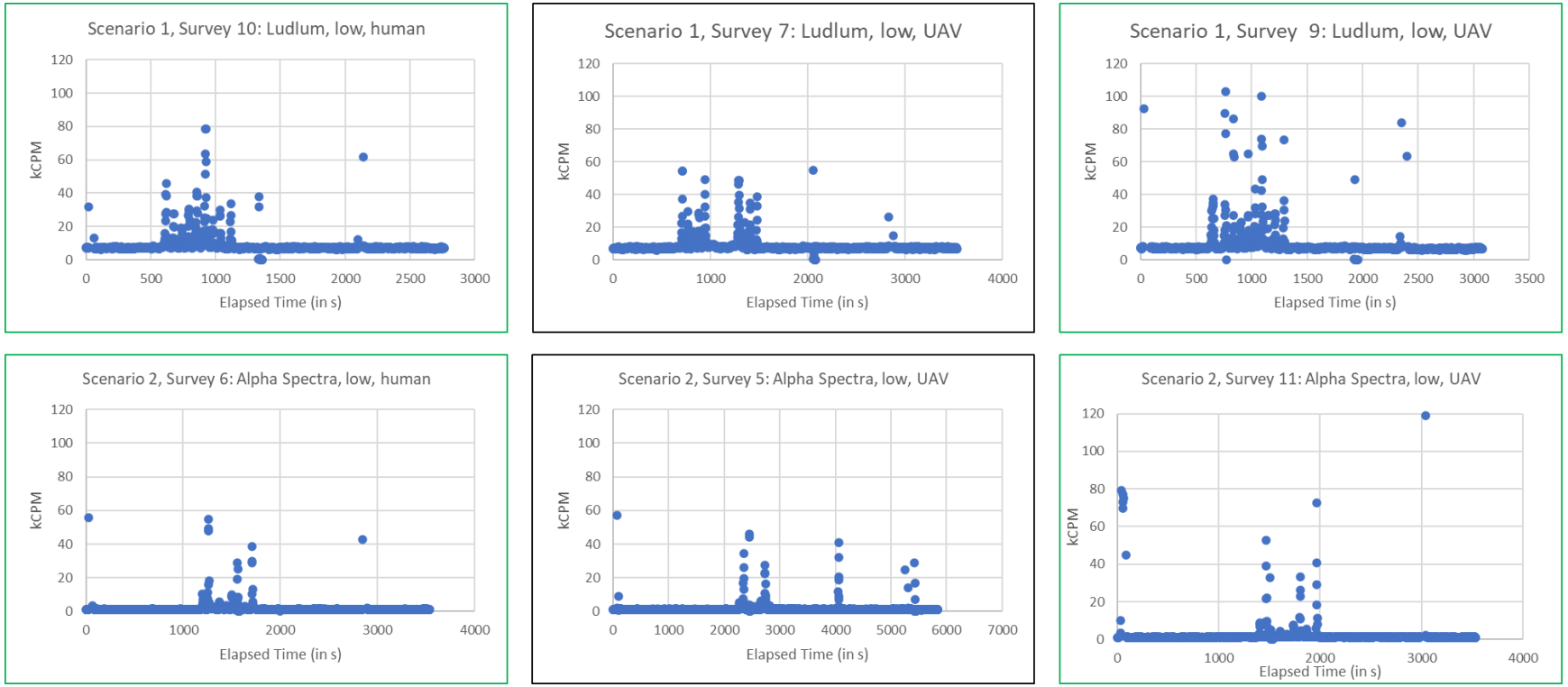

Figure E.1. Radiation Measurements vs. Elapsed time for Scenarios 1 and 2, from Start to End of Data Logging and without Data Processing

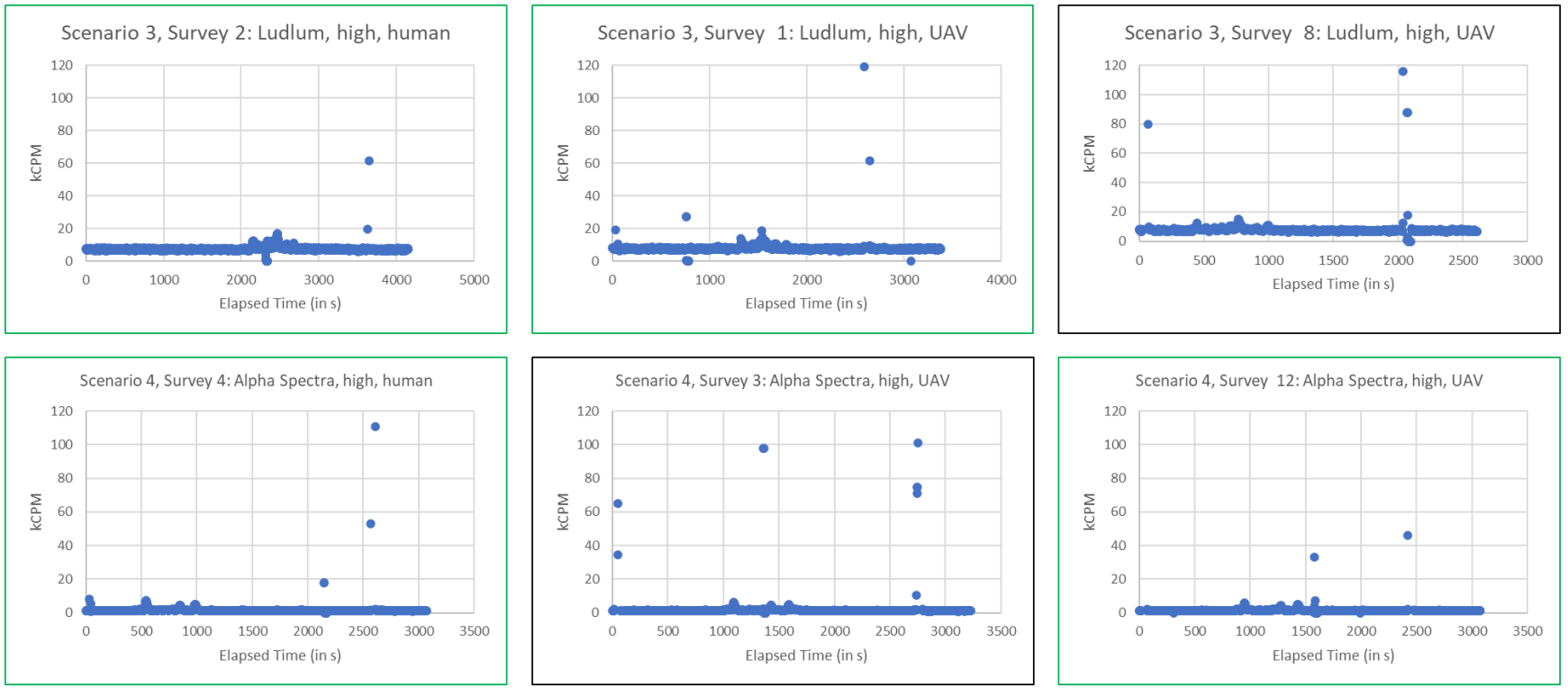

Figure E.2. Radiation Measurements vs. Elapsed Time for Scenarios 3 and 4, from Start to End of Data Logging and Without Data Processing

E.2 Scenario 1 – Ludlum Detector at Low Survey Altitude (Surveys 9 and 10)

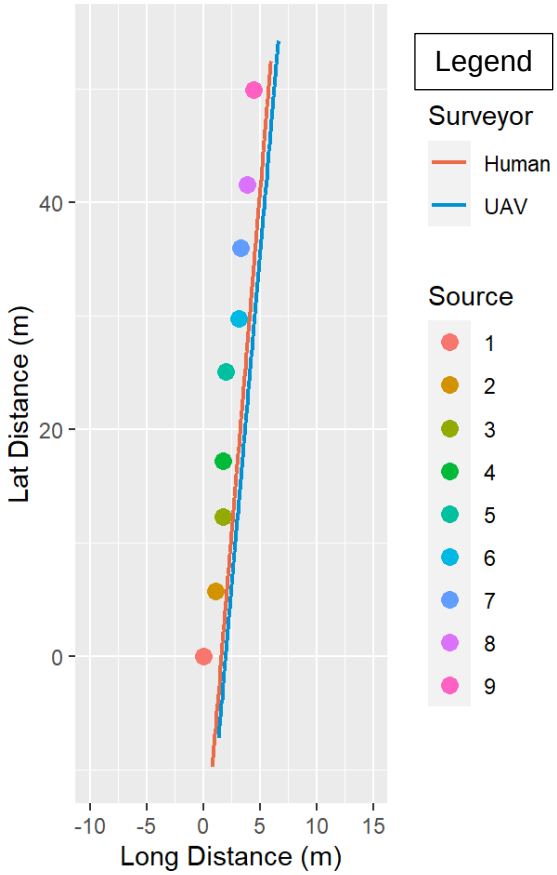

Figure E.3. Check Source Sample Locations and Survey Paths for Surveys 9 and 10

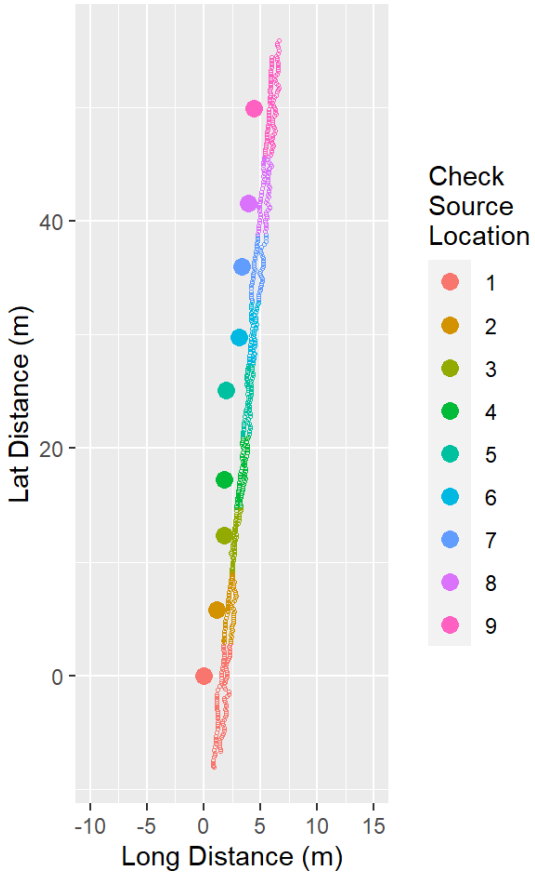

Figure E.4. Survey Transects for Surveys 9 and 10. Source division of the transects is color coded.

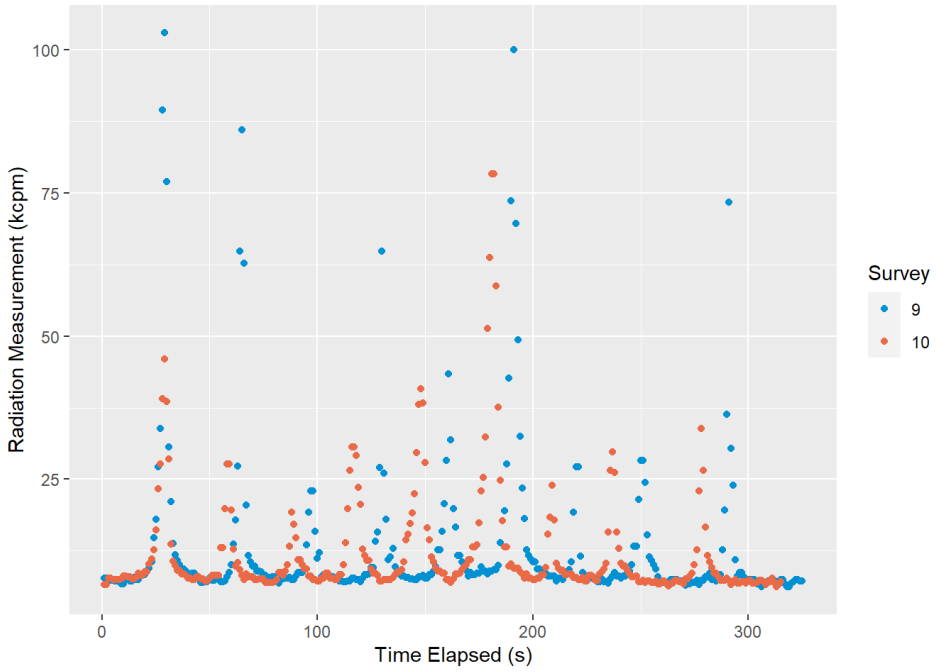

Figure E.5. Count Rate (kcpm) for Surveys 9 and 10 Over Time (s)

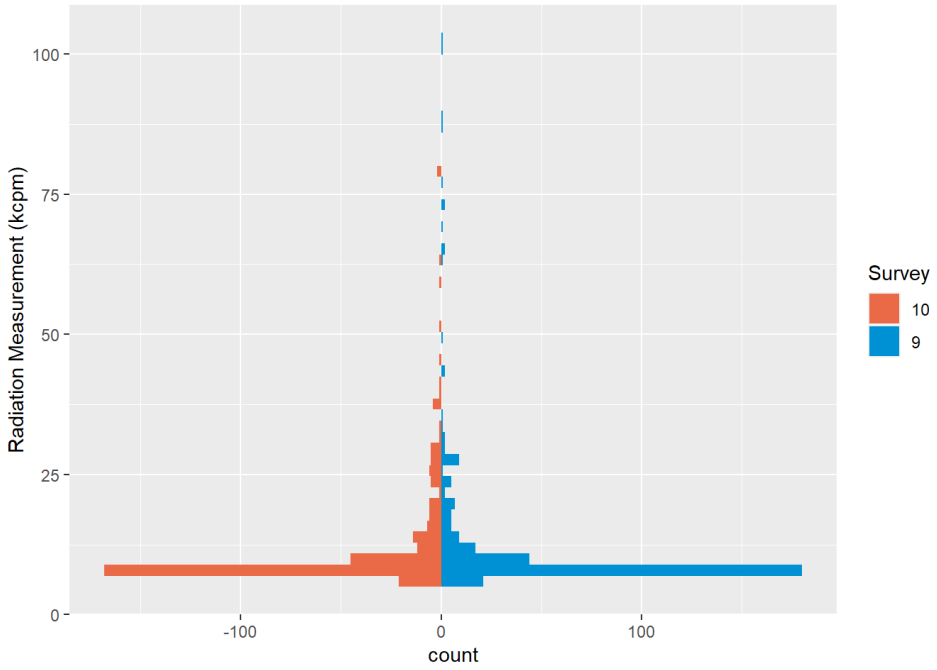

Figure E.6. Histogram of Count Rates (kcpm) for Surveys 9 and 10

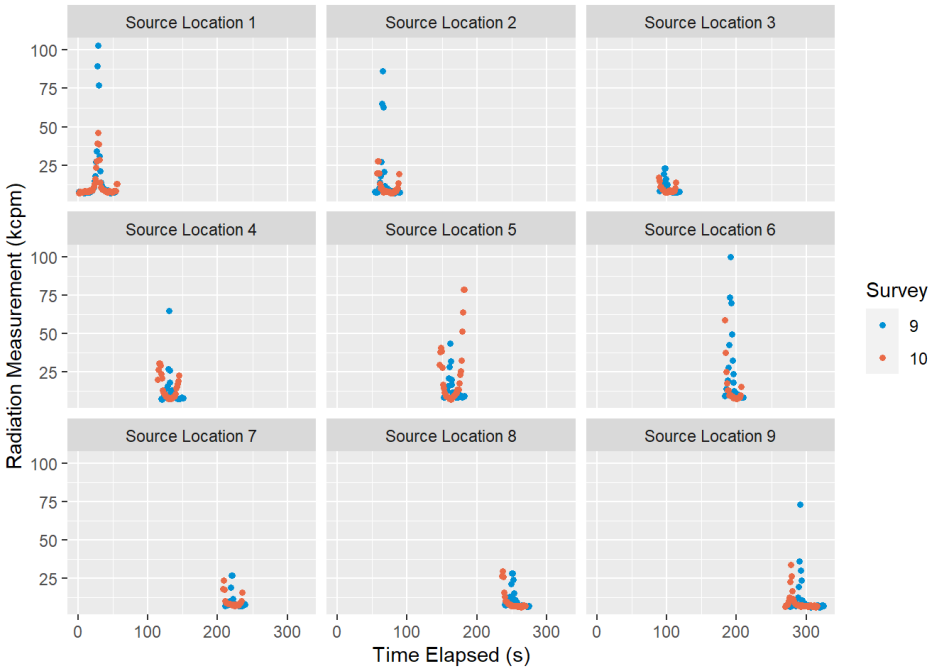

Figure E.7. Count Rate (kcpm) per Check Source Location for Surveys 9 and 10

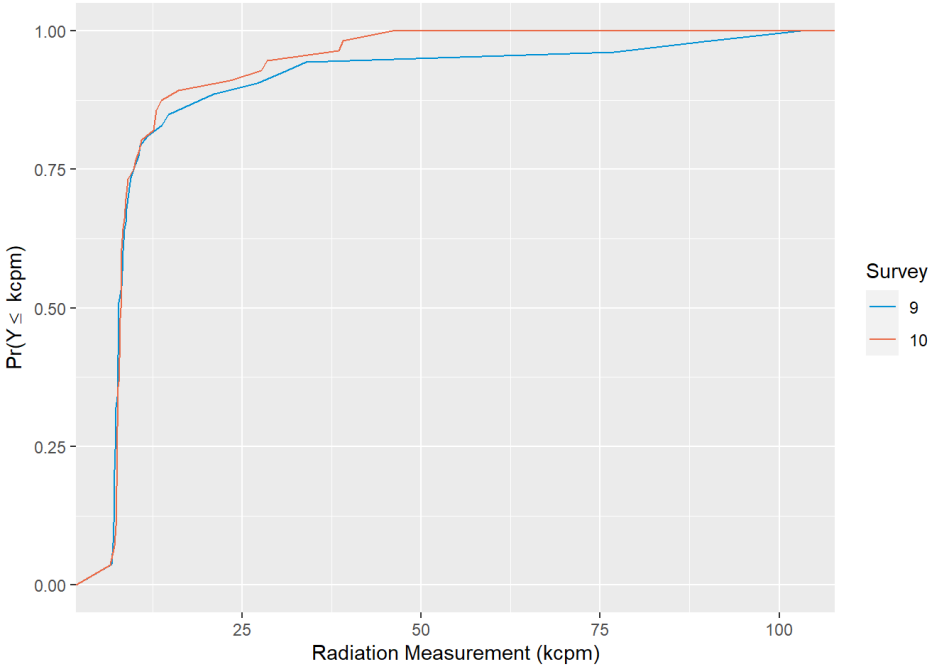

Figure E.8. eCDF Plots for Two-Sample K-S Test for Count Rate at Check Source Location 1 for Surveys 9 and 10. Count rates were not significantly different (p = 0.06773) between the human (survey 10) and UAV (survey 9).

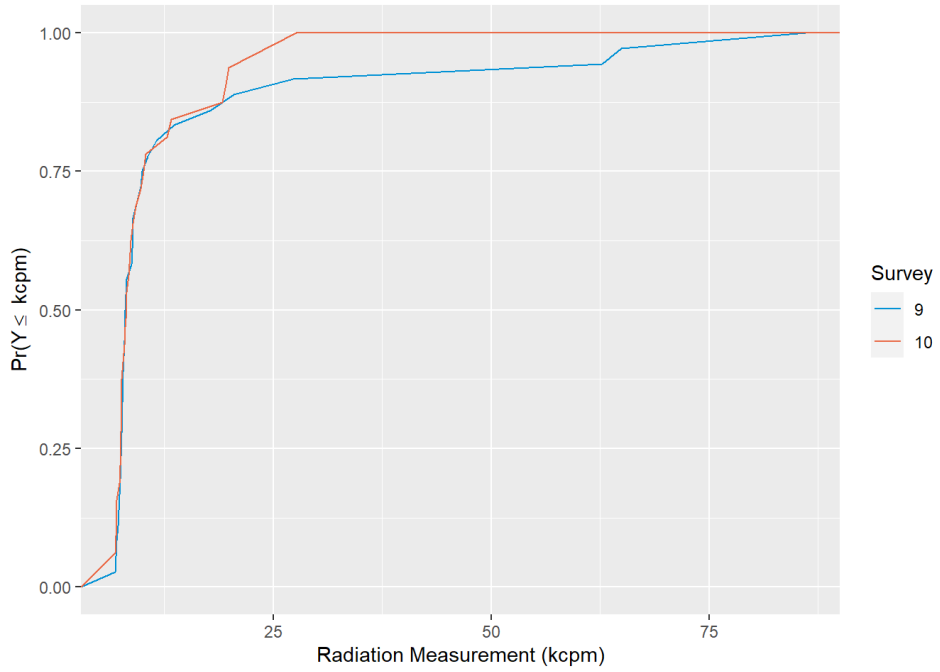

Figure E.9. eCDF Plots for Two-Sample K-S Test for Count Rate at Check Source Location 2 for Surveys 9 and 10. Count rates were not significantly different (p = 0.9972) between the human (survey 10) and UAV (survey 9).

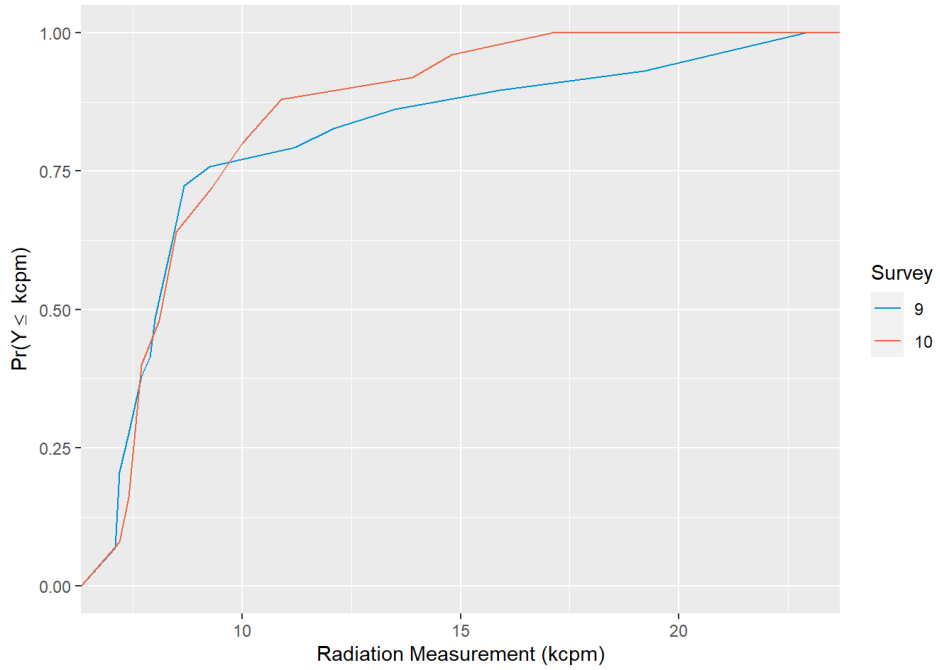

Figure E.10. eCDF Plots for Two-Sample K-S Test for Count Rate at Check Source Location 3 for Surveys 9 and 10. Count rates were not significantly different (p = 0.9821) between the human (survey 10) and UAV (survey 9).

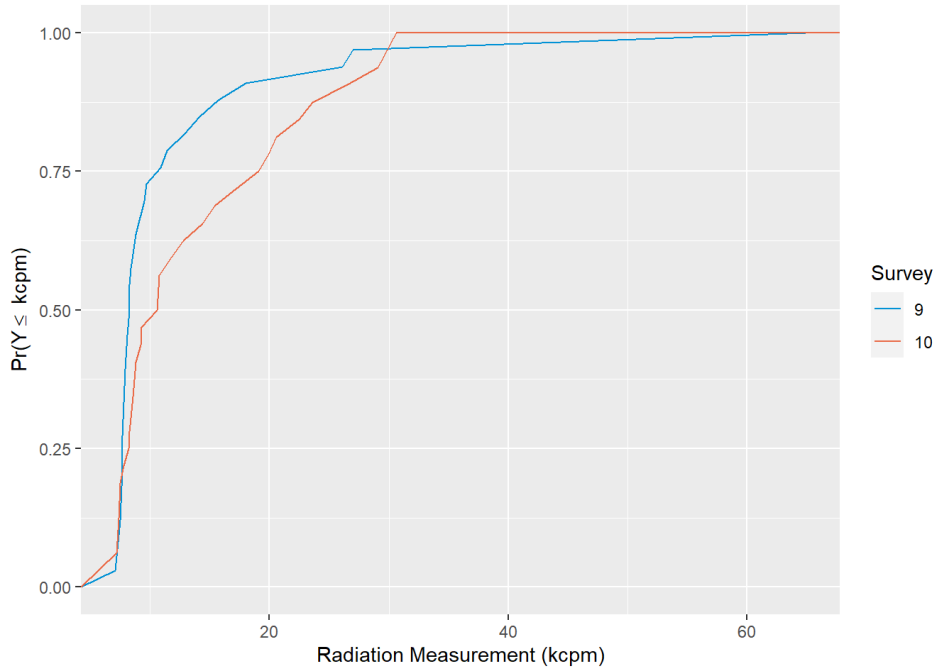

Figure E.11. eCDF Plots for Two-Sample K-S Test for Count Rate at Check Source Location 4 for Surveys 9 and 10. Count rates were not significantly different (p = 0.1194) between the human (survey 10) and UAV (survey 9).

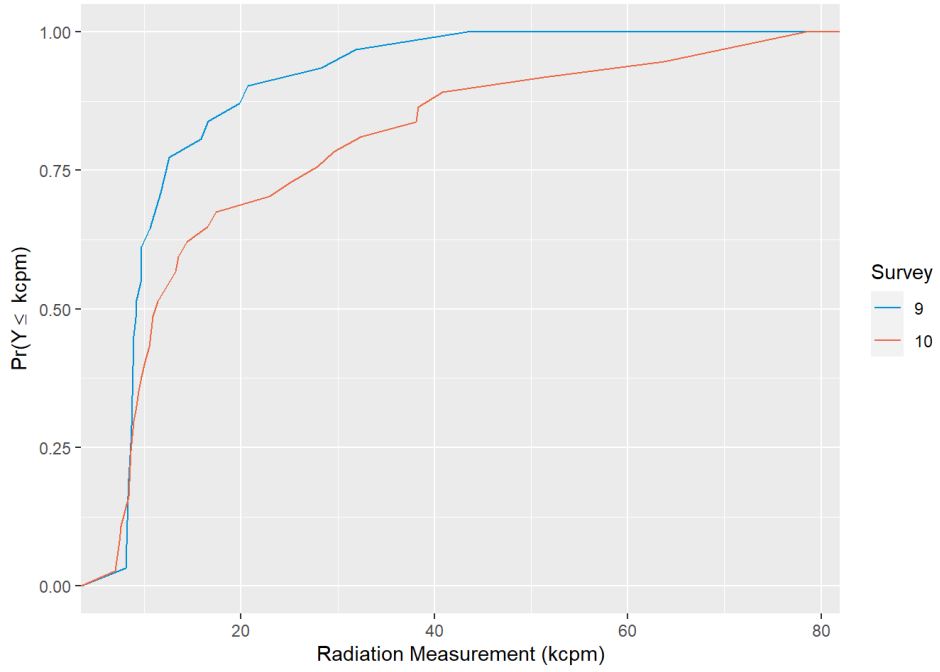

Figure E.12. eCDF Plots for Two-Sample K-S Test for Count Rate at Check Source Location 5 for Surveys 9 and 10. Count rates were not significantly different (p = 0.2018) between the human (survey 10) and UAV (survey 9).

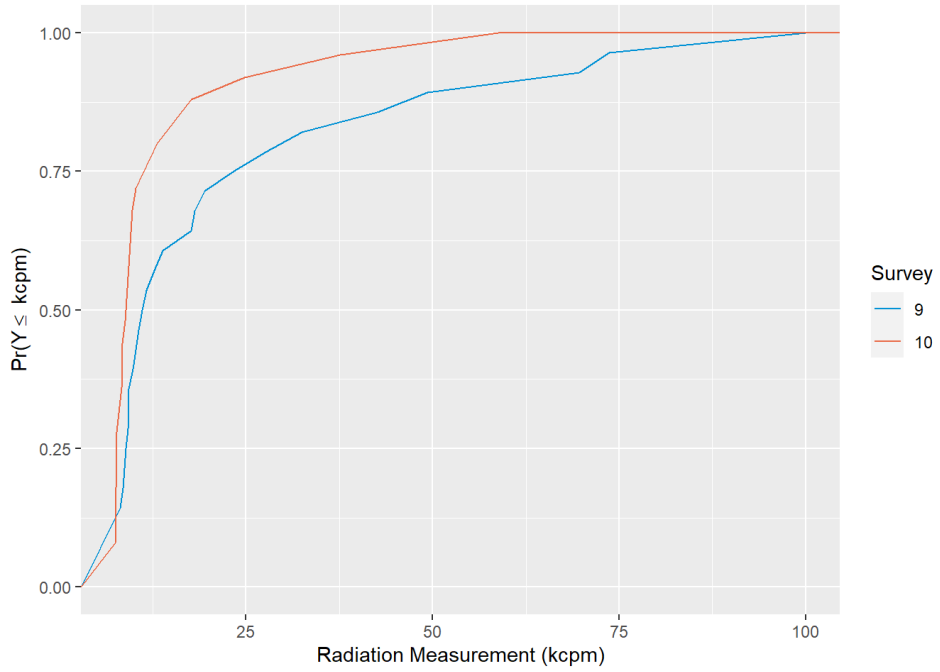

Figure E.13. eCDF Plots for Two-Sample K-S Test for Count Rate at Check Source Location 6 for Surveys 9 and 10. Count rates were not significantly different (p = 0.1184) between the human (survey 10) and UAV (survey 9).

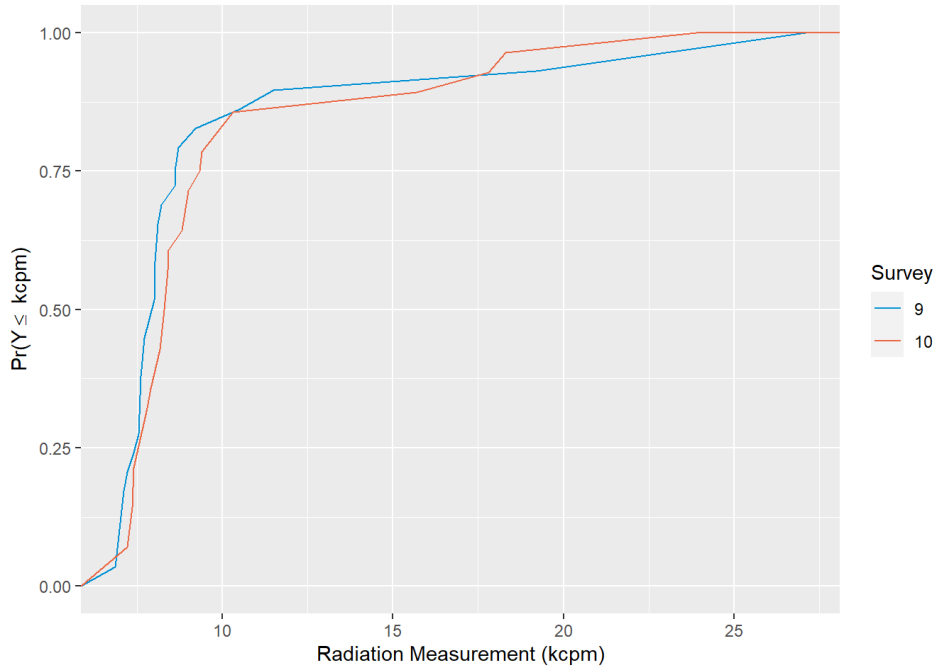

Figure E.14. eCDF Plots for Two-Sample K-S Test for Count Rate at Check Source Location 7 for Surveys 9 and 10. Count rates were not significantly different (p = 0.1591) between the human (survey 10) and UAV (survey 9).

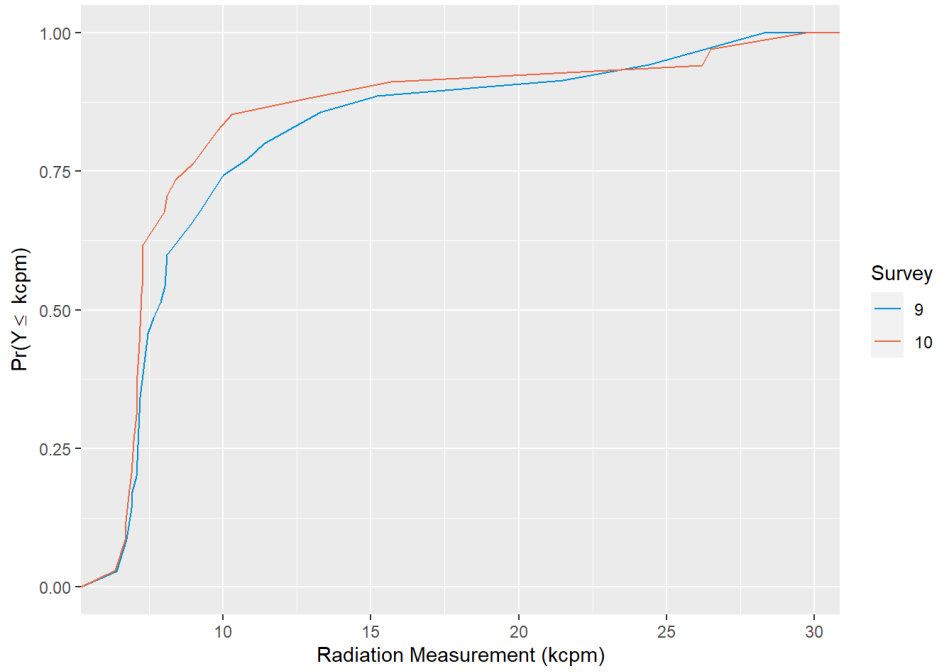

Figure E.15. eCDF Plots for Two-Sample K-S Test for Count Rate at Check Source Location 8 for Surveys 9 and 10. Count rates were not significantly different (p = 0.1478) between the human (survey 10) and UAV (survey 9).

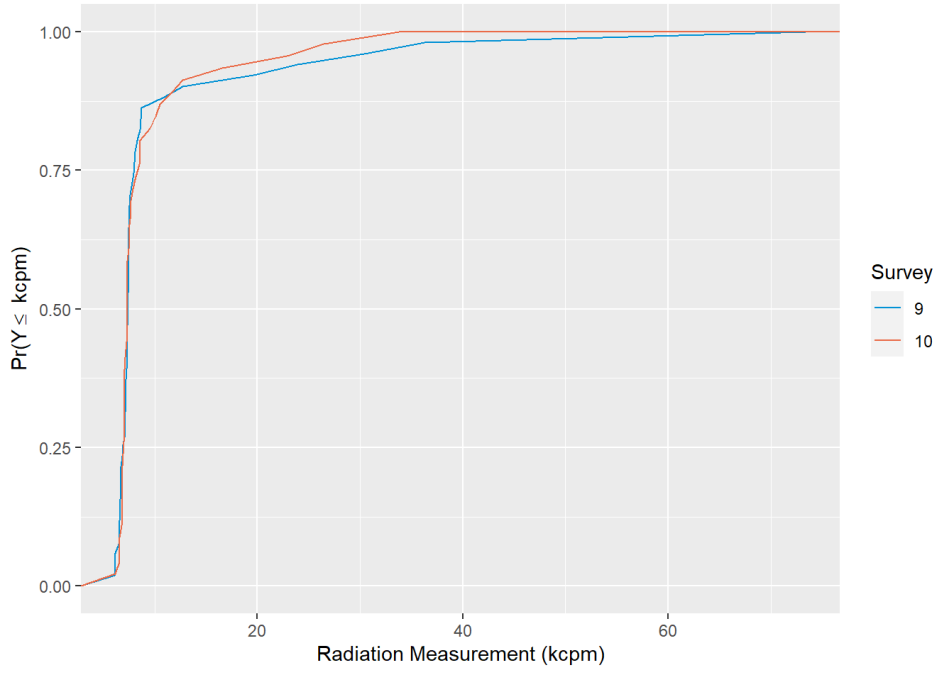

Figure E.16. eCDF Plots for Two-Sample K-S Test for Count Rate at Check Source Location 9 for Surveys 9 and 10. Count rates were not significantly different (p = 0.7421) between the human (survey 10) and UAV (survey 9).

E.3 Scenario 2 – Alpha Spectra Detector at Low Survey Altitude (Survey 11 and 6)

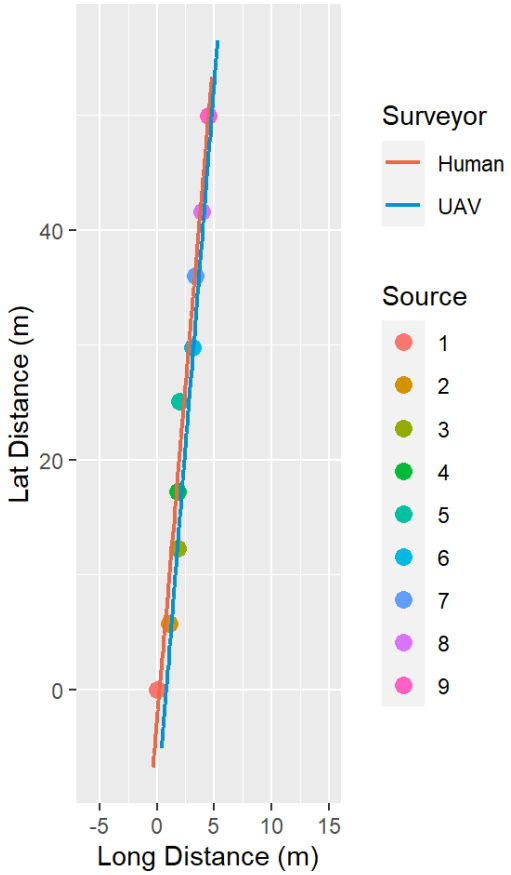

Figure E.17. Check Source Sample Locations and Survey Paths for Surveys 6 and 11

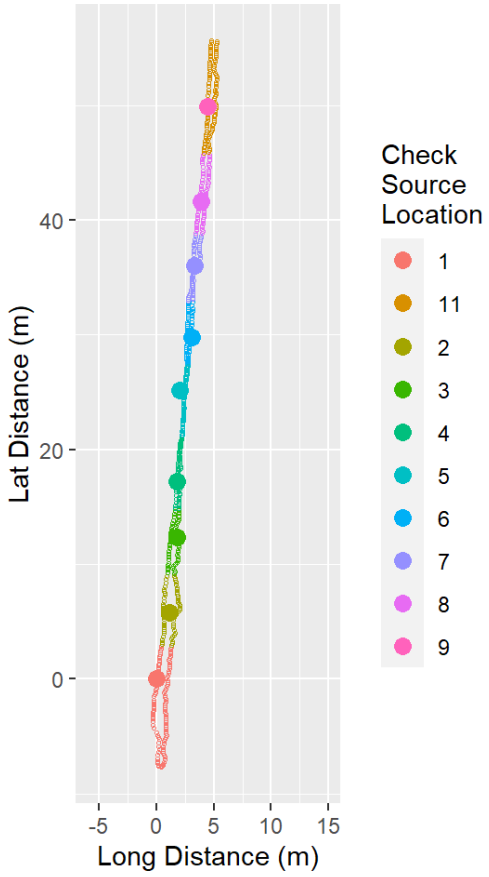

Figure E.18. Survey Transects for Surveys 6 and 11. Source division of the transects is color coded.

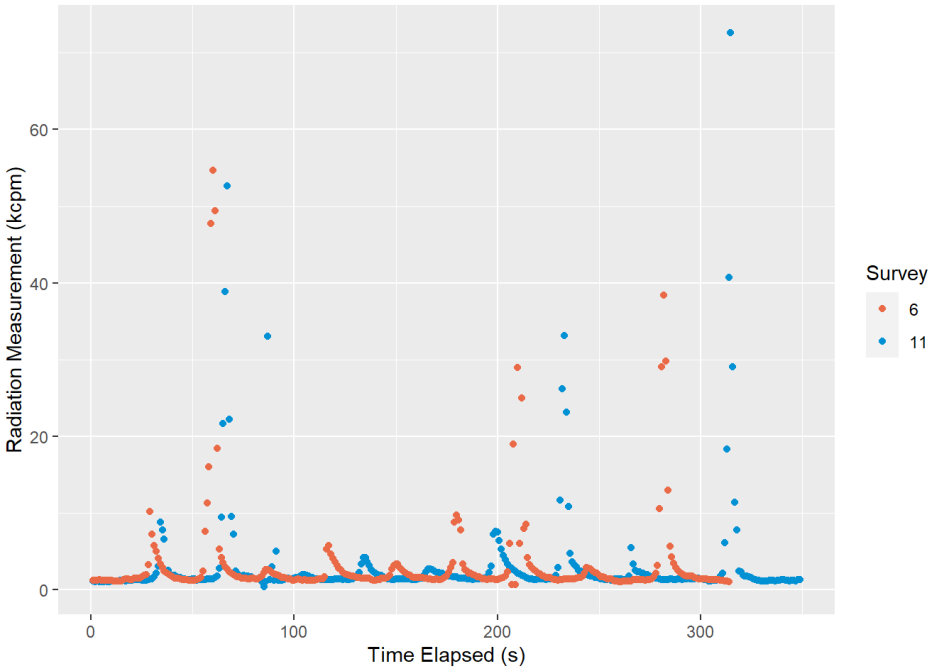

Figure E.19. Count Rates (kcpm) for Surveys 6 and 11 Over Time (s)

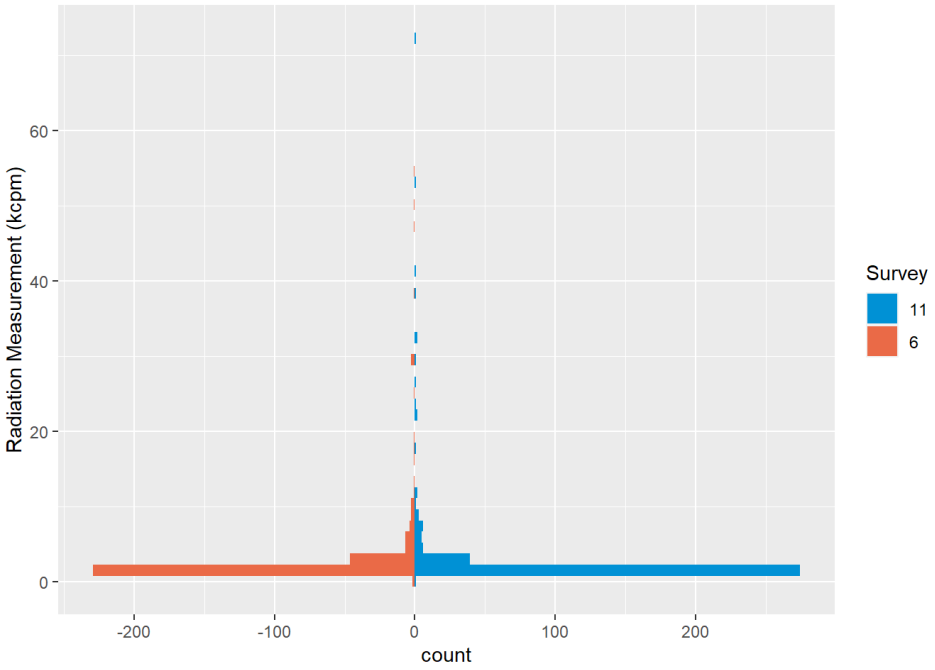

Figure E.20. Histogram of Count Rates (kcpm) for Surveys 6 and 11

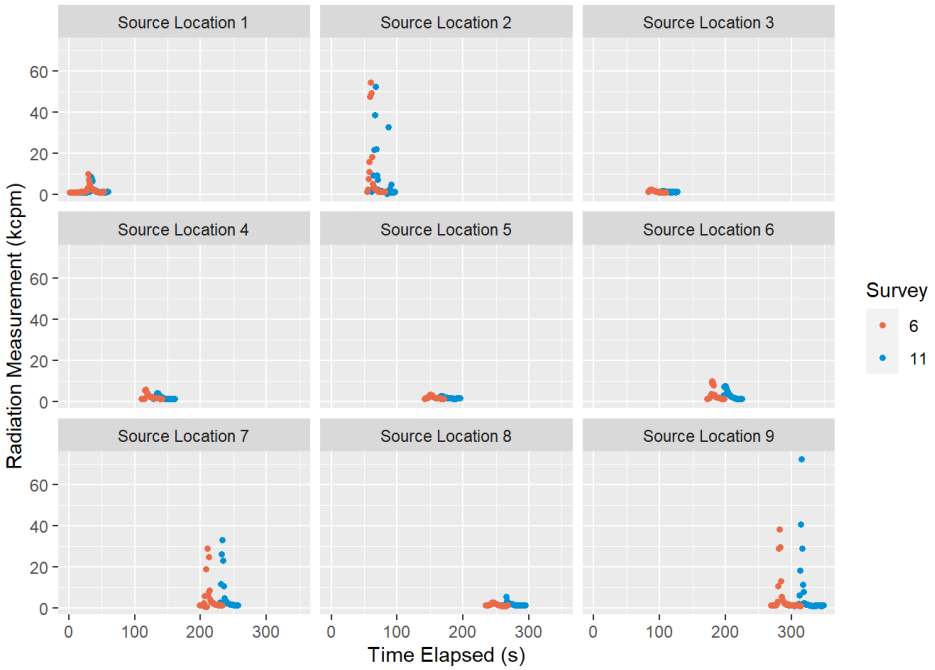

Figure E.21. Count Rate (kcpm) by Check Source Location for Surveys 6 and 11.

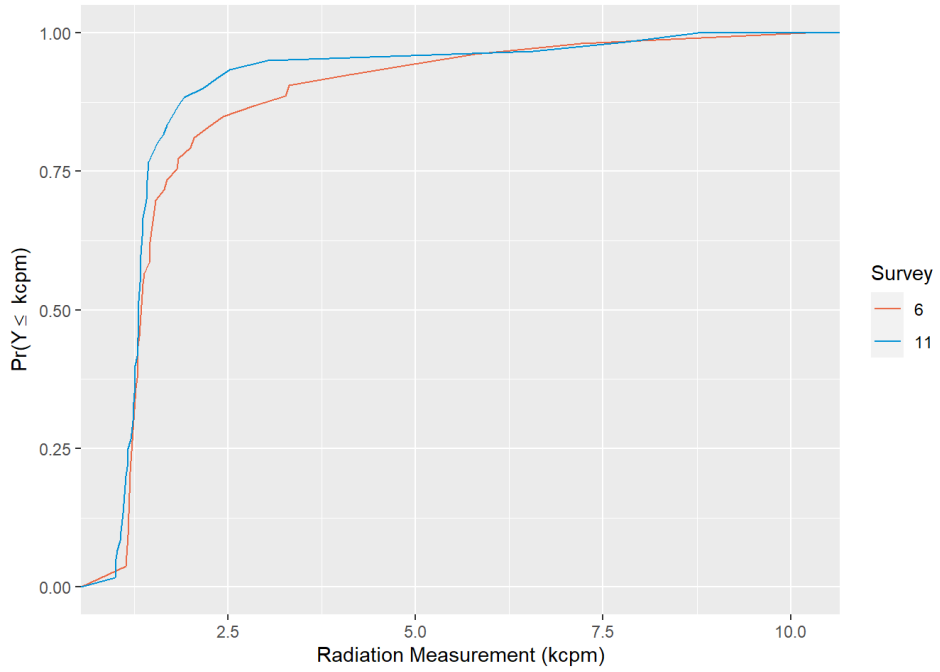

Figure E.22. eCDF Plots for Two-Sample K-S Test for Count Rate at Check Source Location 1 for Surveys 6 and 11. Count rates were not significantly different (p = 0.2073) between the human (survey 6) and UAV (survey 11).

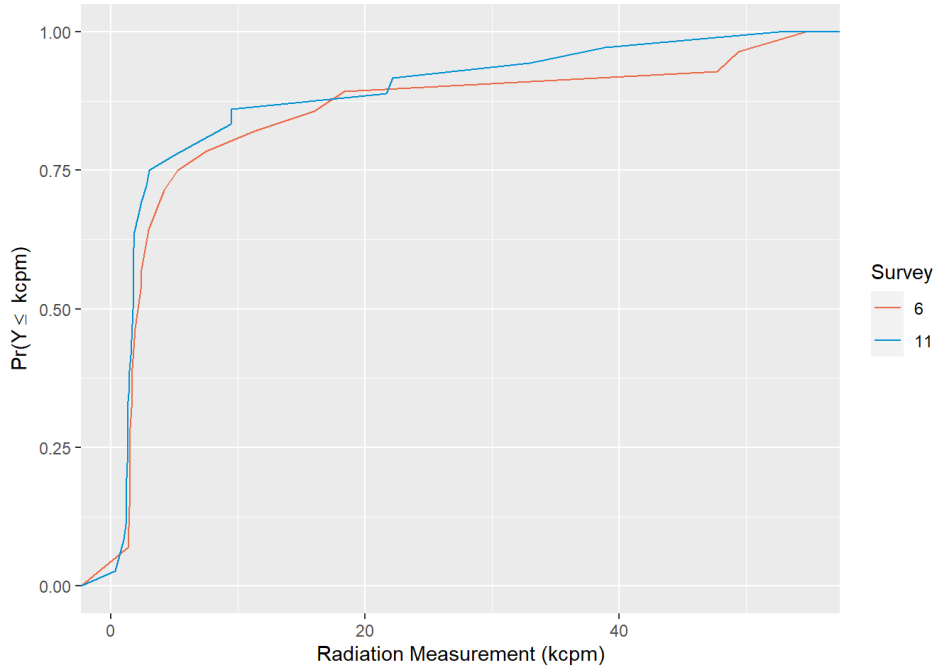

Figure E.23. eCDF Plots for Two-Sample K-S Test for Count Rate at Check Source Location 2 for Surveys 6 and 11. Count rates were not significantly different (p = 0.06039) between the human (survey 6) and UAV (survey 11).

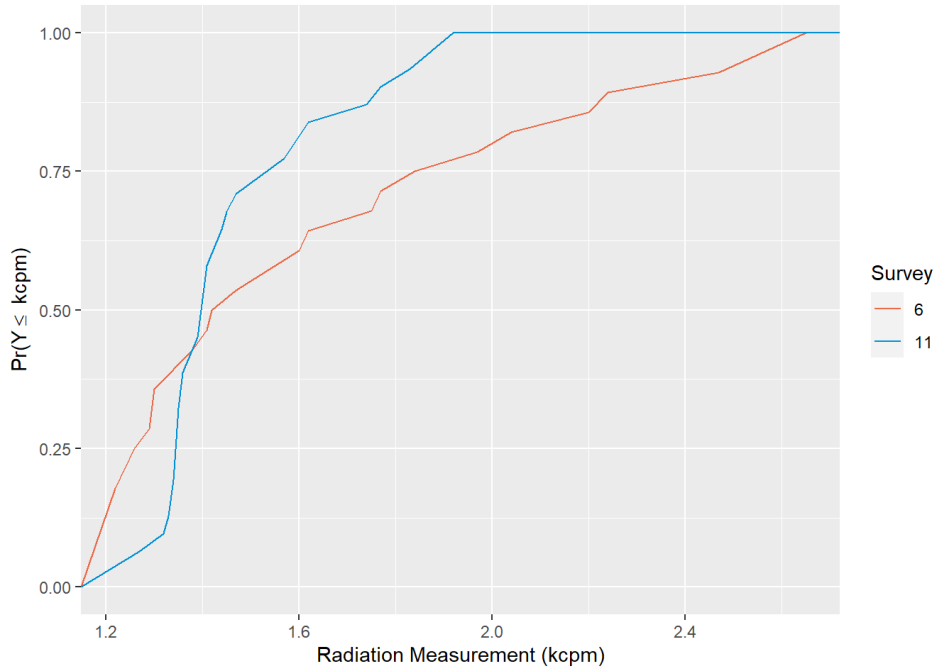

Figure E.24. eCDF Plots for Two-Sample K-S Test for Count Rate at Check Source Location 3 for Surveys 6 and 11. Count rates were not significantly different (p = 0.1609) between the human (survey 6) and UAV (survey 11).

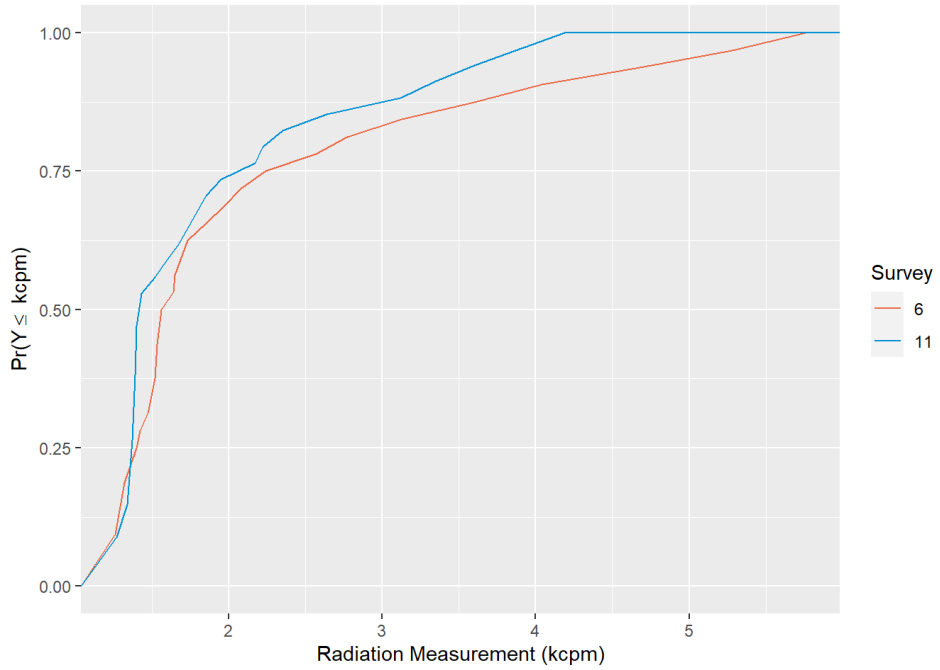

Figure E.25. eCDF Plots for Two-Sample K-S Test for Count Rate at Check Source Location 4 for Surveys 6 and 11. Count rates were not significantly different (p = 0.262) between the human (survey 6) and UAV (survey 11).

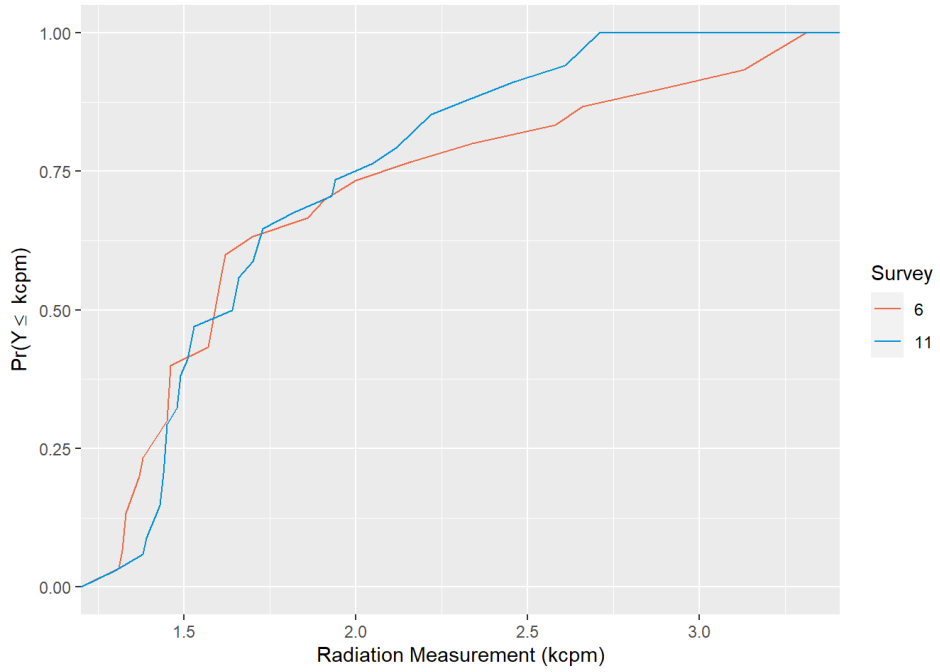

Figure E.26. eCDF Plots for Two-Sample K-S Test for Count Rate at Check Source Location 5 for Surveys 6 and 11. Count rates were not significantly different (p = 0.7168) between the human (survey 6) and UAV (survey 11).

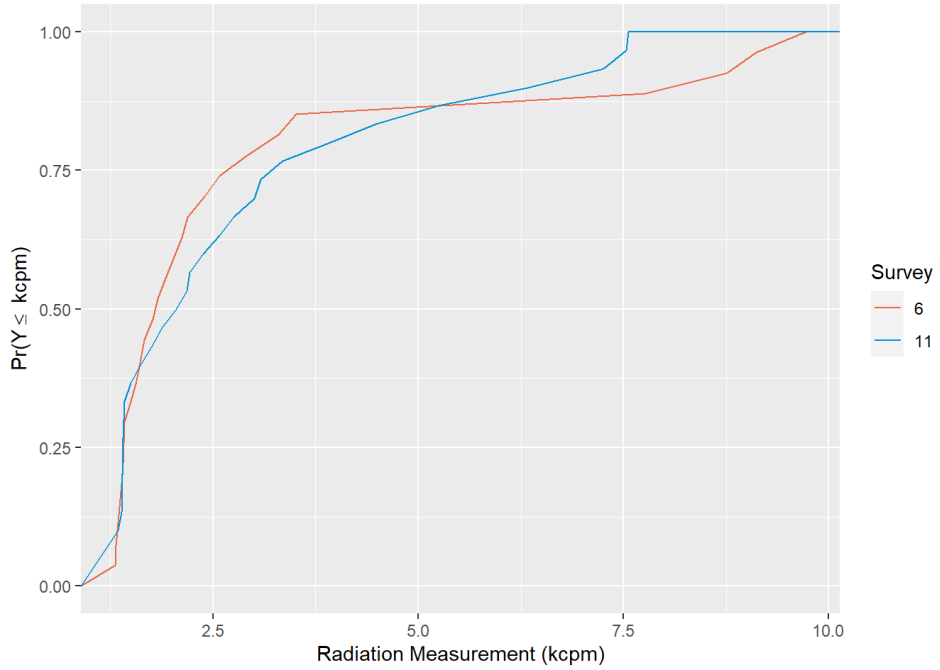

Figure E.27. eCDF plots for two-sample K-S test for count rate at check source location 6 for surveys 6 and 11. Count rates were not significantly different (p = 0.9141) between the human (survey 6) and UAV (survey 11).

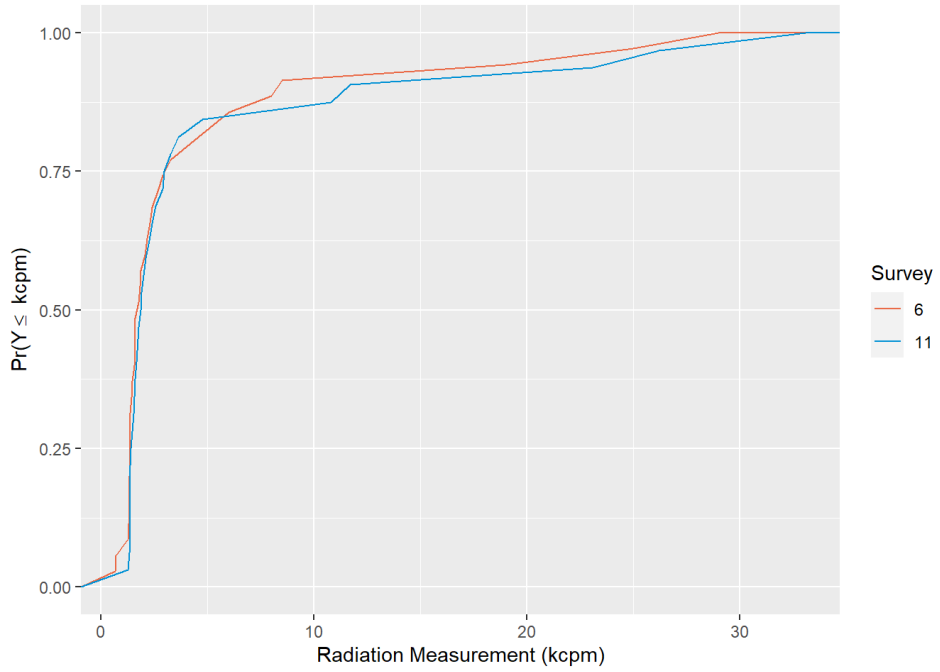

Figure E.28. eCDF Plots for Two-Sample K-S Test for Count Rate at Check Source Location 7 for Surveys 6 and 11. Count rates were not significantly different (p = 0.7809) between the human (survey 6) and UAV (survey 11).

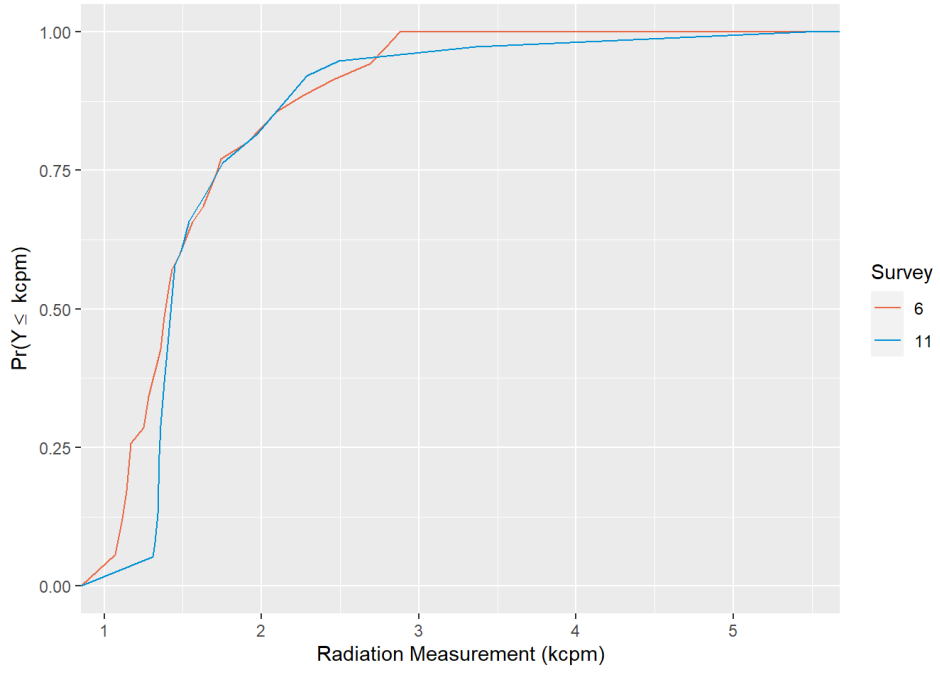

Figure E.29. eCDF Plots for Two-Sample K-S Test for Count Rate at Check Source Location 8 for Surveys 6 and 11. Count rates were not significantly different (p = 0.02759) between the human (survey 6) and UAV (survey 11).

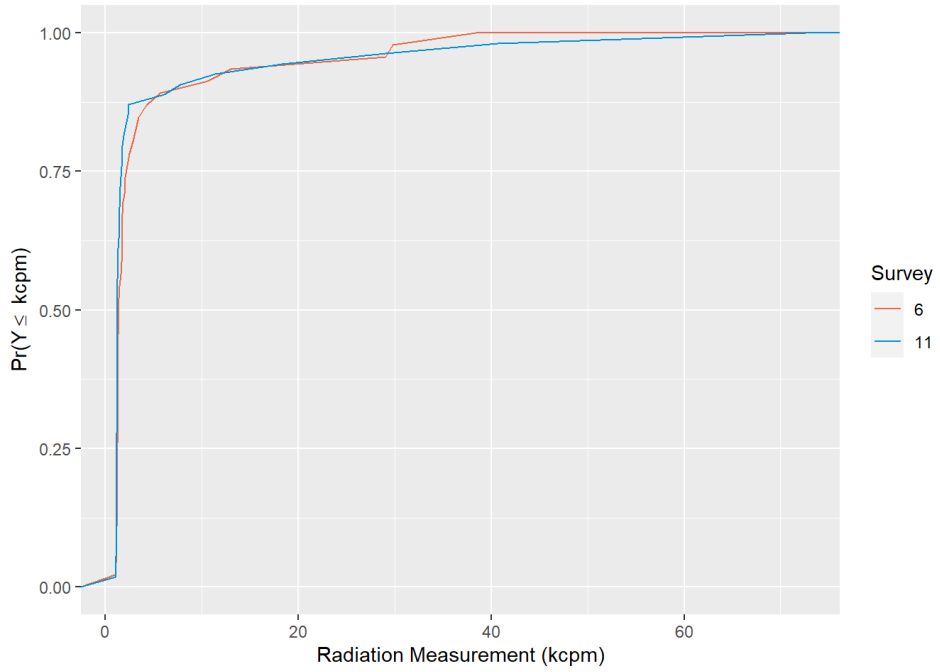

Figure E.30. eCDF Plots for Two-Sample K-S Test for Count Rate at Check Source Location 9 for Surveys 6 and 11. Count rates were significantly different (p = 0.00144) between the human (survey 6) and UAV (survey 11).

E.4 Scenario 3 – Ludlum Detector at High Survey Altitude (Survey 1 and 2)

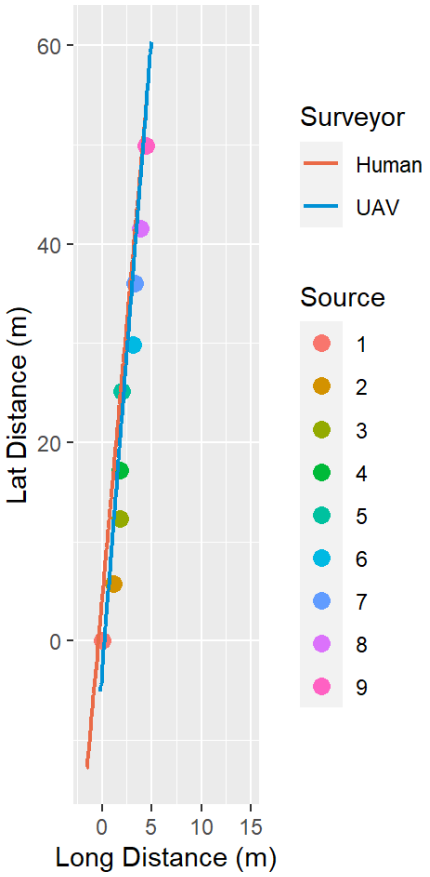

Figure E.31. Check Source Sample Locations and Survey Paths for Surveys 1 and 2

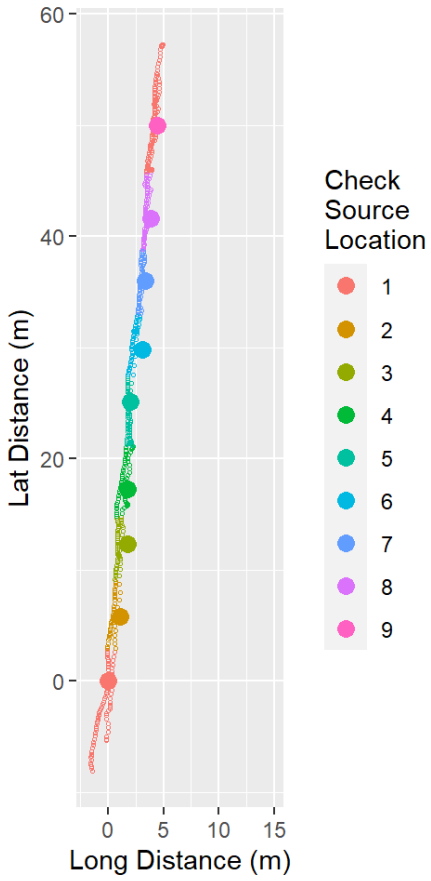

Figure E.32. Survey Transects for Surveys 1 and 2. Source division of the transects is color coded.

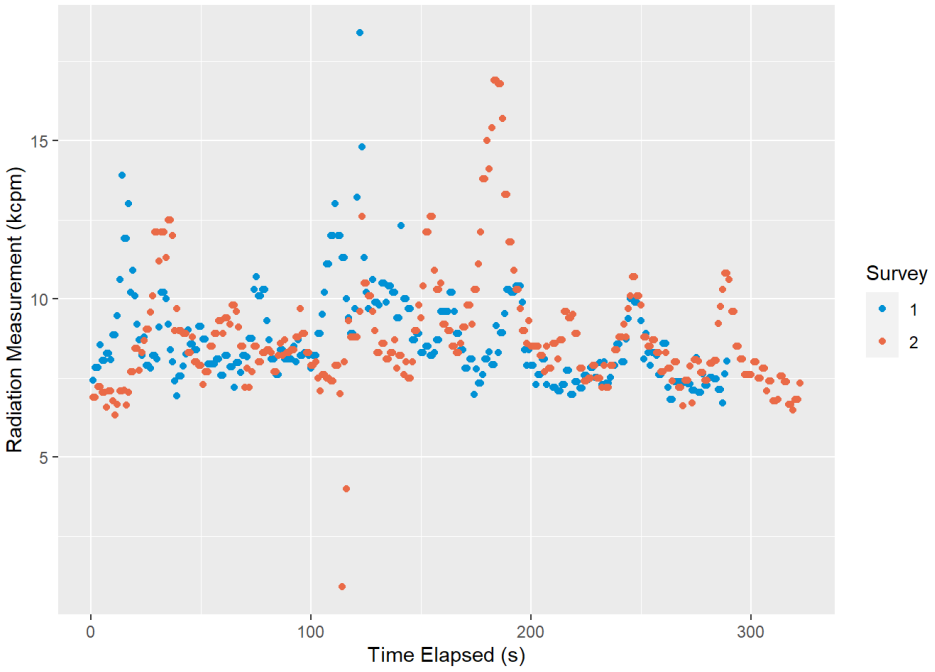

Figure E.33. Count Rates (kcpm) for Surveys 1 and 2 Over Time (s)

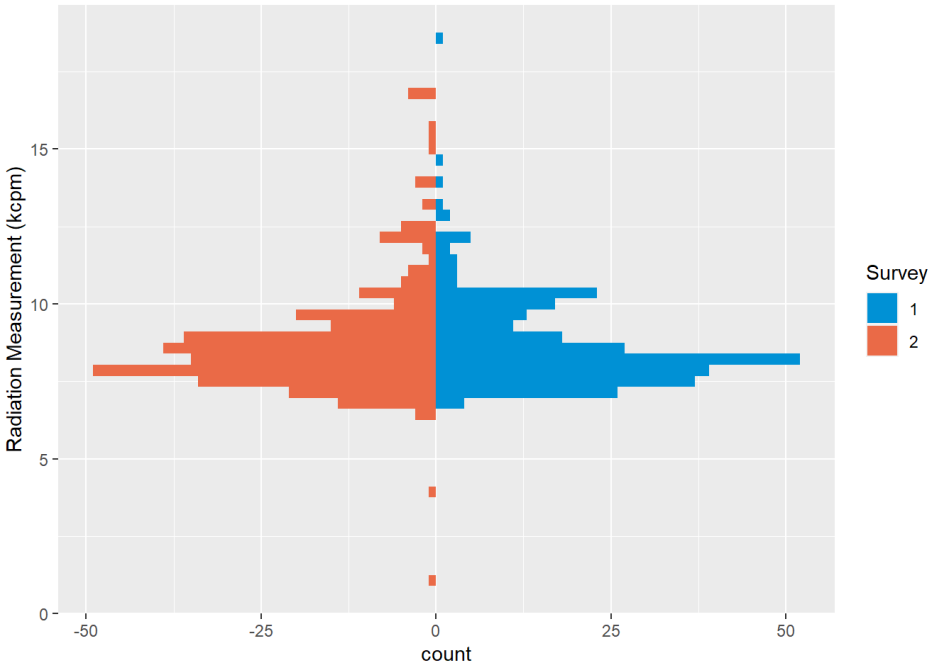

Figure E.34. Histogram of Count Rates (kcpm) for Surveys 1 and 2

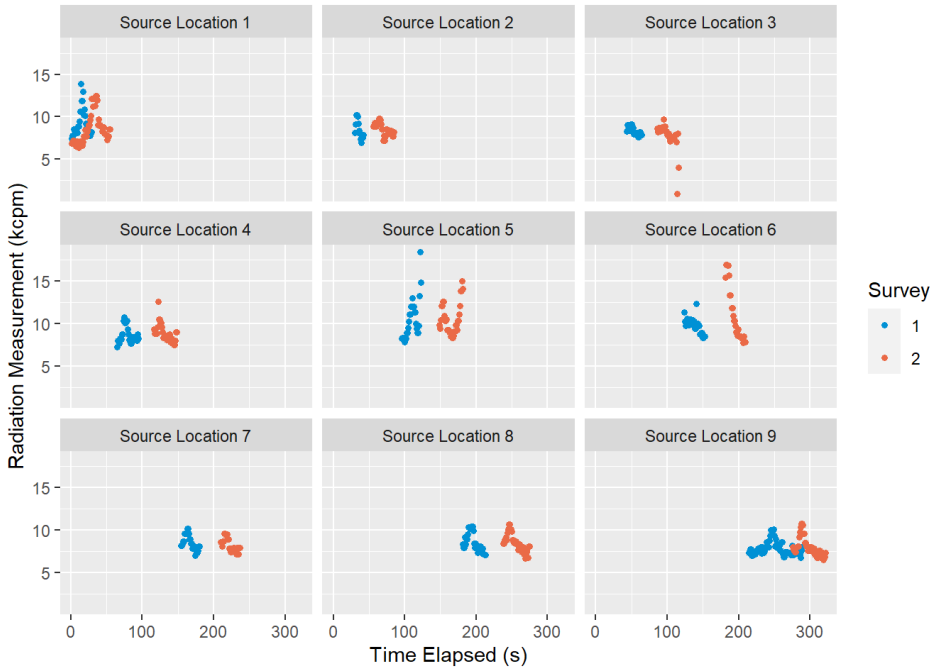

Figure E.35. Count rate (kcpm) by Source Location for Surveys 1 and 2

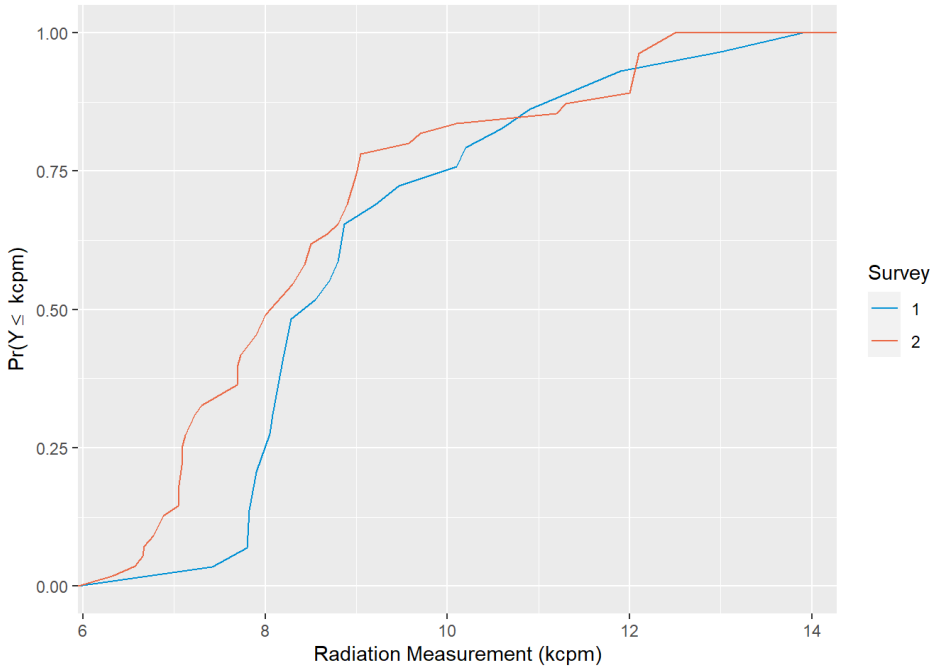

Figure E.36. eCDF Plots for Two-Sample K-S Test for Count Rate at Check Source Location 1 for Surveys 1 and 2. Count rates were not significantly different (p = 0.007462) between the human (survey 2) and UAV (survey 1).

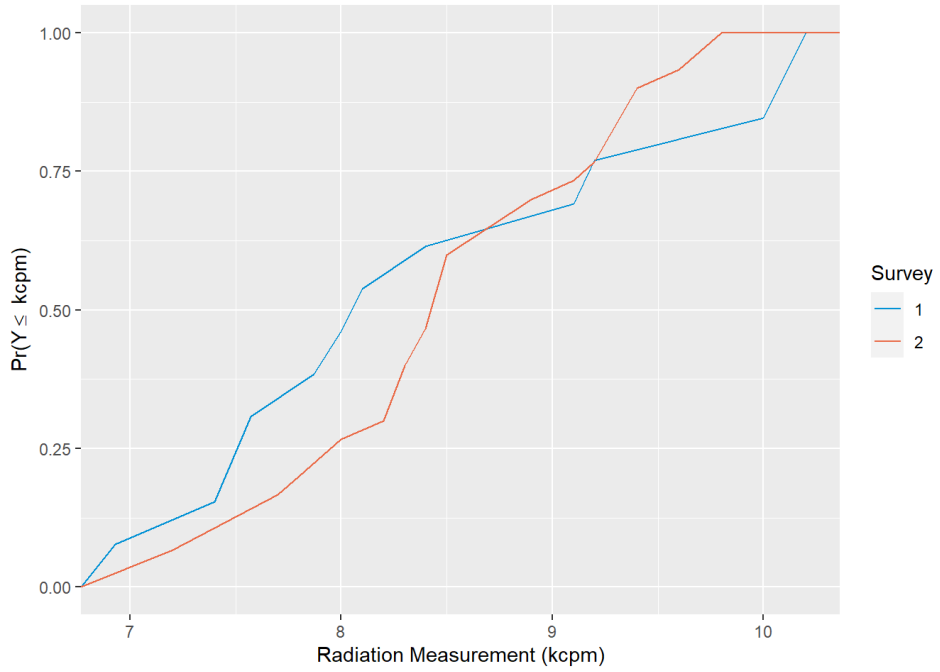

Figure E.37. eCDF Plots for Two-Sample K-S Test for Count Rate at Check Source Location 2 for Surveys 1 and 2. Count rates were not significantly different (p = 0.5143) between the human (survey 2) and UAV (survey 1).

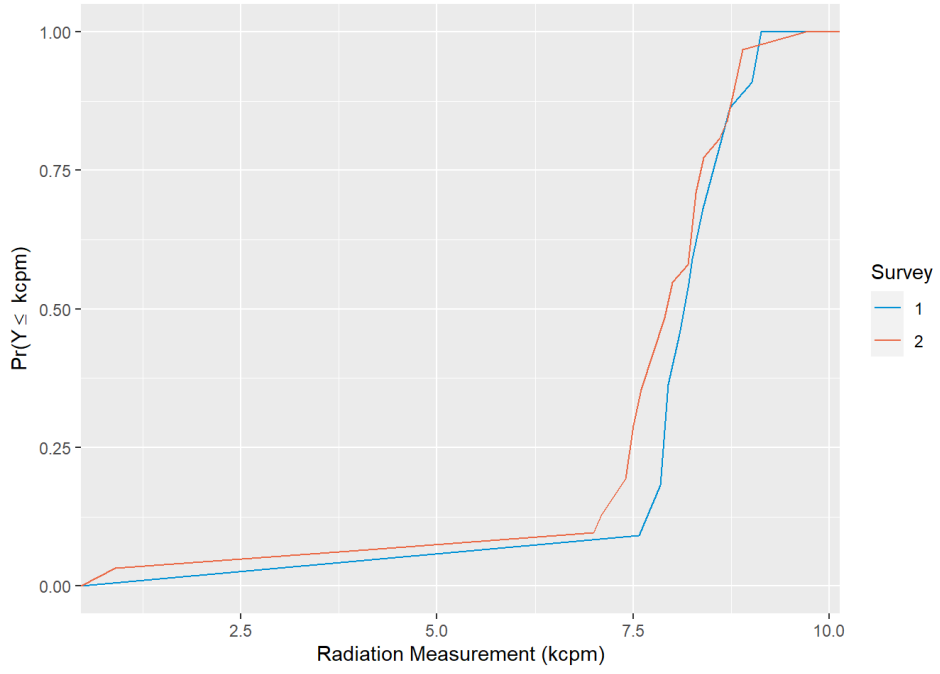

Figure E.38. eCDF Plots for Two-Sample K-S Test for Count Rate at Check Source Location 3 for Surveys 1 and 2. Count rates were not significantly different (p = 0.1909) between the human (survey 2) and UAV (survey 1).

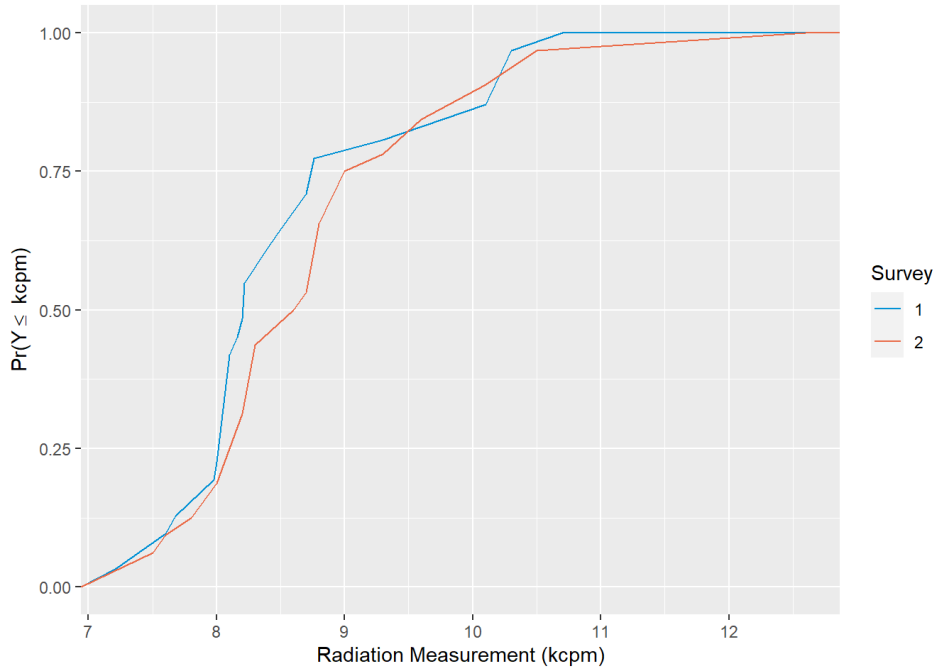

Figure E.39. eCDF Plots for Two-Sample K-S Test for Count Rate at Check Source Location 4 for Surveys 1 and 2. Count rates were not significantly different (p = 0.3106) between the human (survey 2) and UAV (survey 1).

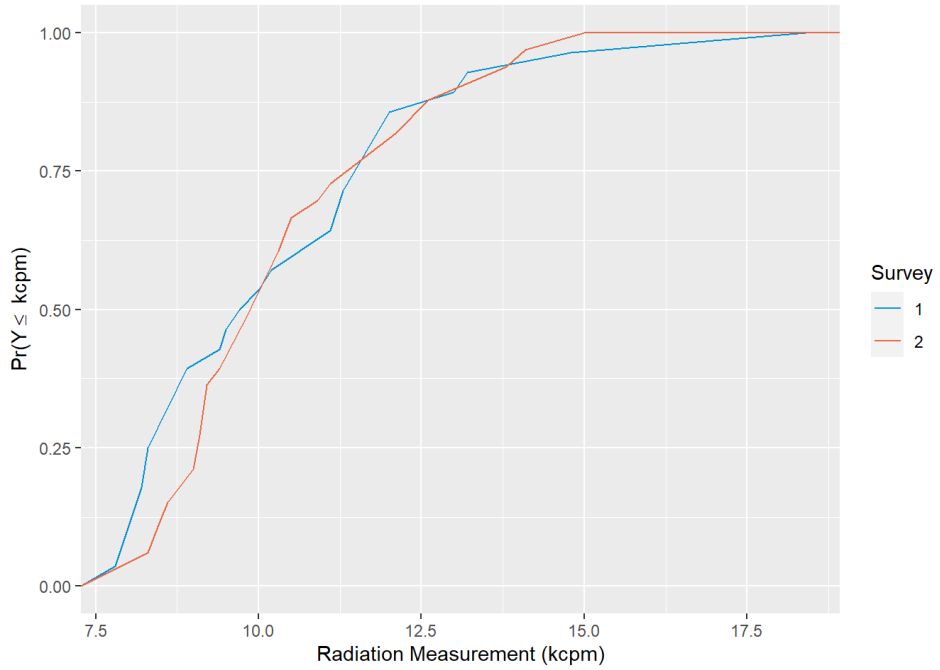

Figure E.40. eCDF Plots for Two-Sample K-S Test for Count Rate at Check Source Location 5 for Surveys 1 and 2. Count rates were not significantly different (p = 0.3408) between the human (survey 2) and UAV (survey 1).

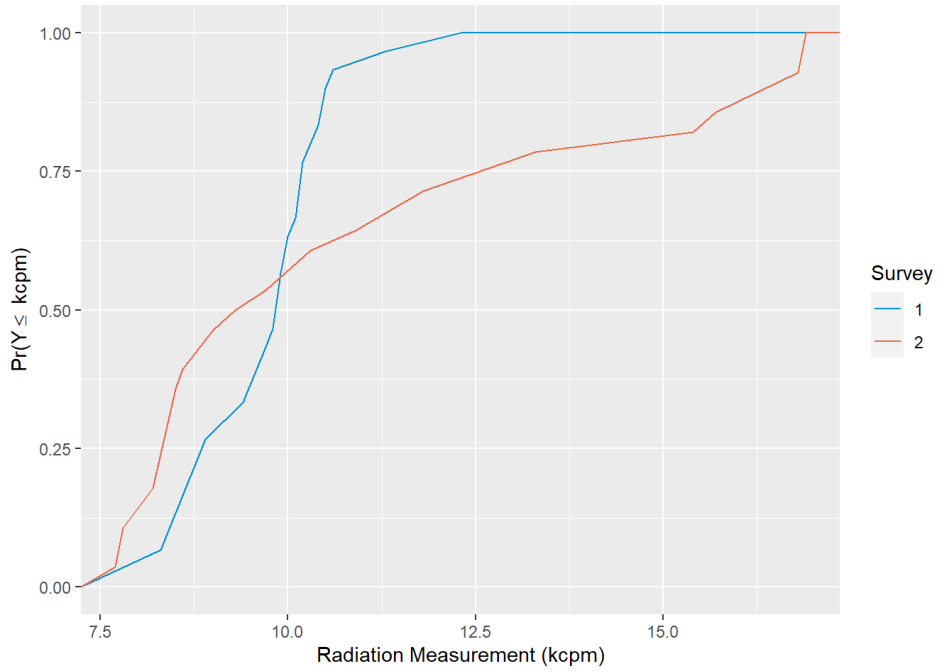

Figure E.41. eCDF Plots for Two-Sample K-S Test for Count Rate at Check Source Location 6 for Surveys 1 and 2. Count rates were not significantly different (p = 0.09173) between the human (survey 2) and UAV (survey 1).

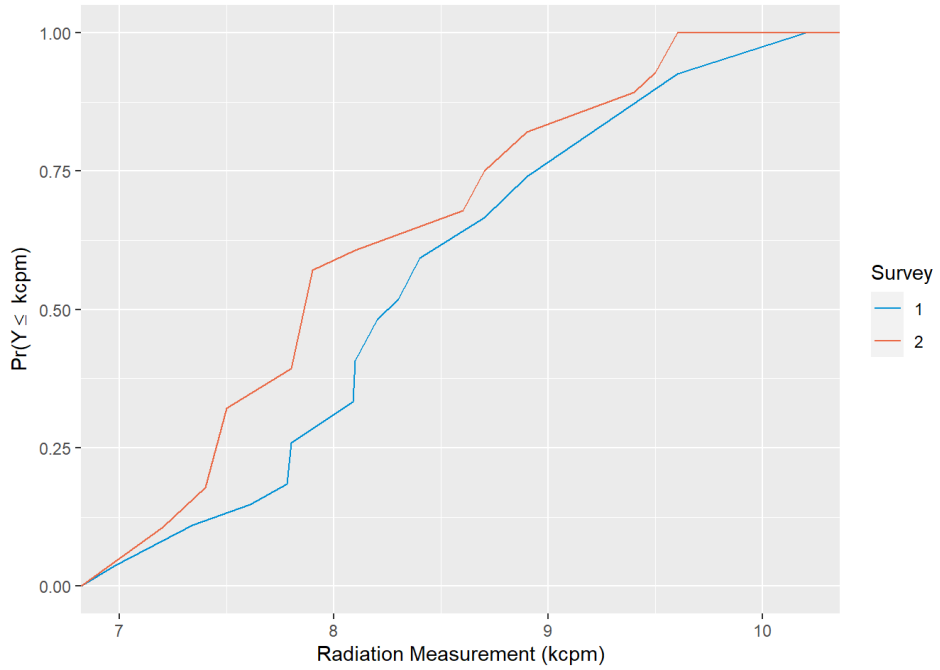

Figure E.42. eCDF Plots for Two-Sample K-S Test for Count Rate at Check Source Location 7 for Surveys 1 and 2. Count rates were not significantly different (p = 0.1372) between the human (survey 2) and UAV (survey 1).

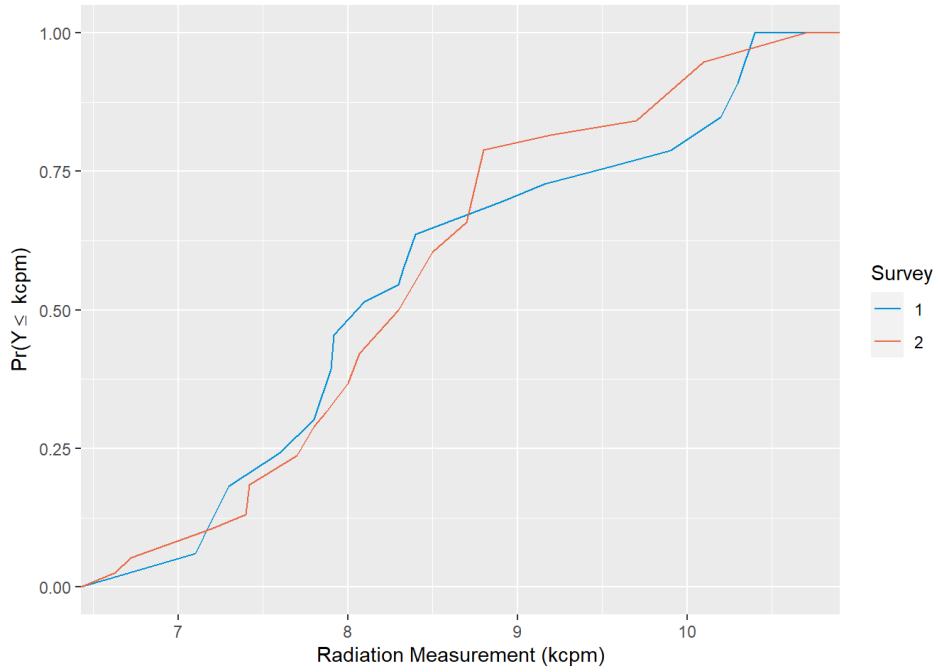

Figure E.43. eCDF Plots for Two-Sample K-S Test for Count Rate at Check Source Location 8 for Surveys 1 and 2. Count rates were not significantly different (p = 0.76) between the human (survey 2) and UAV (survey 1).

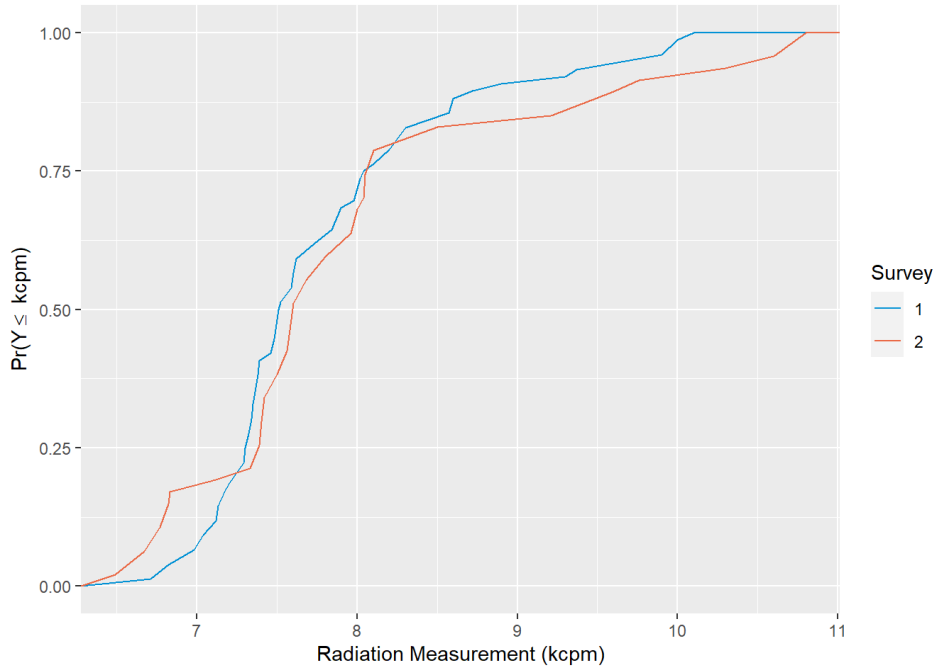

Figure E.44. eCDF Plots for Two-Sample K-S Test for Count Rate at Check Source Location 9 for Surveys 1 and 2. Count rates were not significantly different (p = 0.3795) between the human (survey 2) and UAV (survey 1).

E.5 Scenario 4 – Alpha Spectra Detector at High Survey Altitude (Survey 12 and 4)

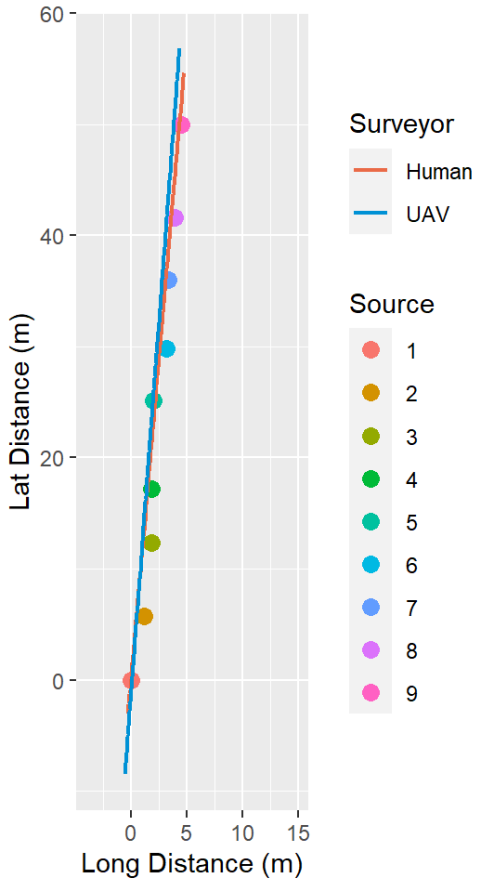

Figure E.45. Check Source Sample Locations and Survey Paths for Surveys 4 and 12

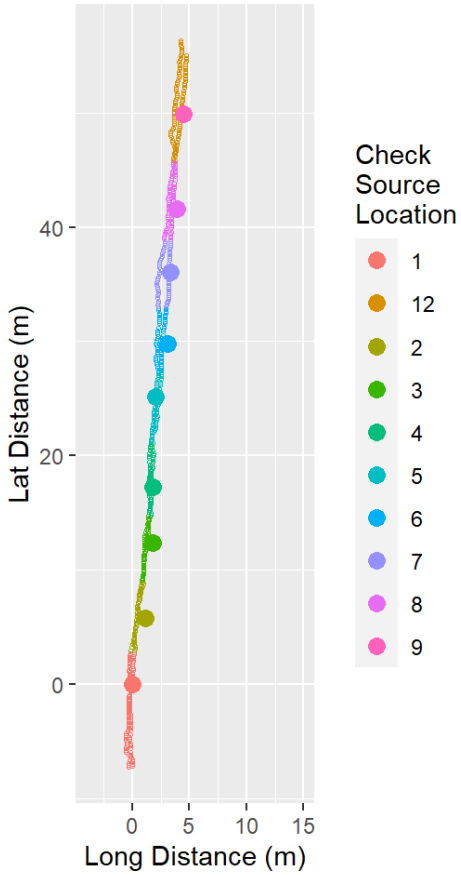

Figure E.46. Survey Transects for Surveys 4 and 12. Source division of the transects is color coded.

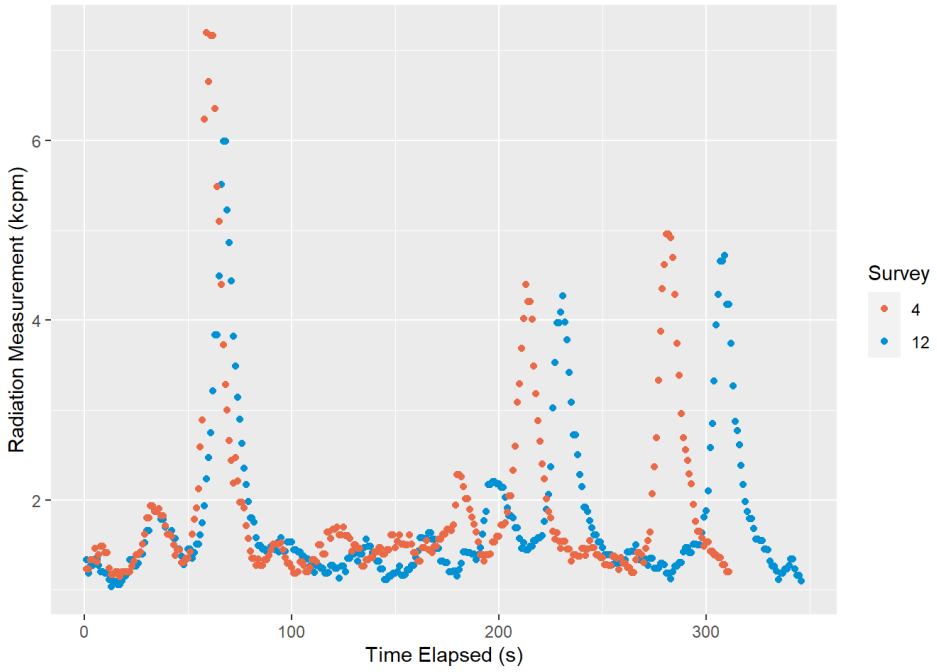

Figure E.47. Count Rate (kcpm) for Surveys 4 and 12 Over Time (s)

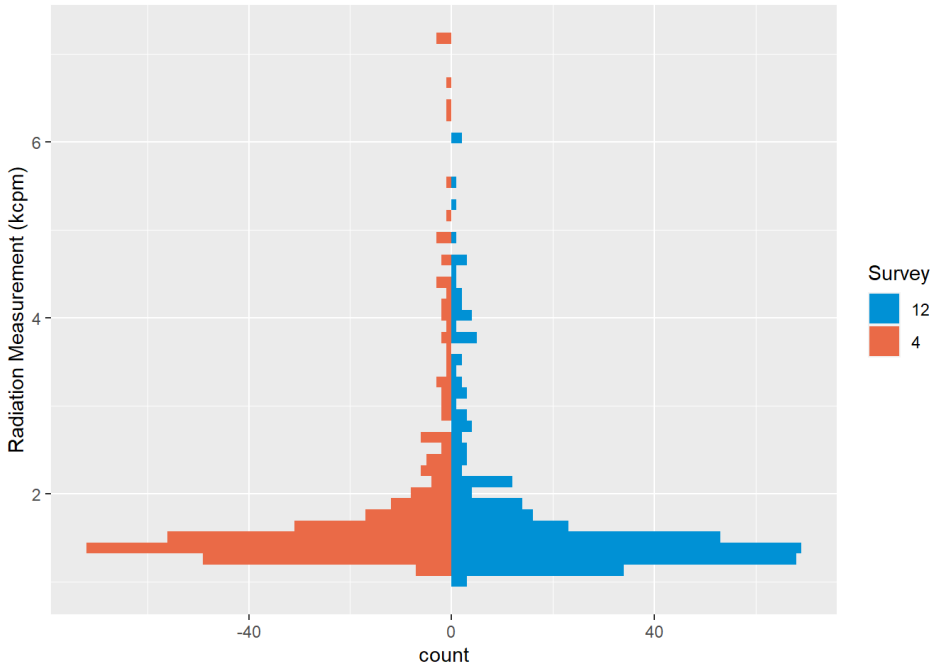

Figure E.48. Histogram of Count Rates (kcpm) for Surveys 4 and 12

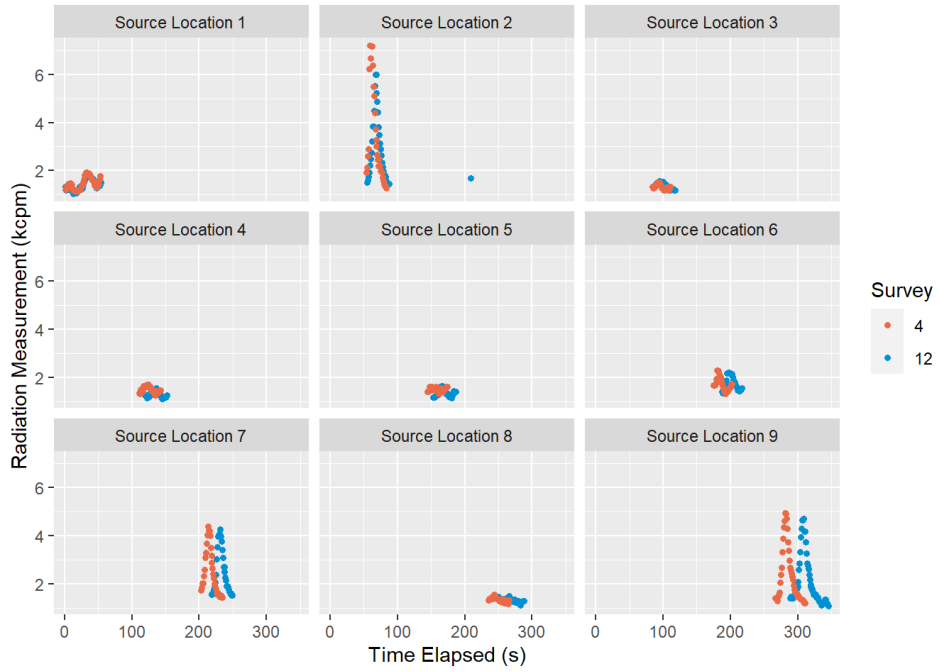

Figure E.49. Count Rate (kcpm) by Source Location for Surveys 4 and 12.

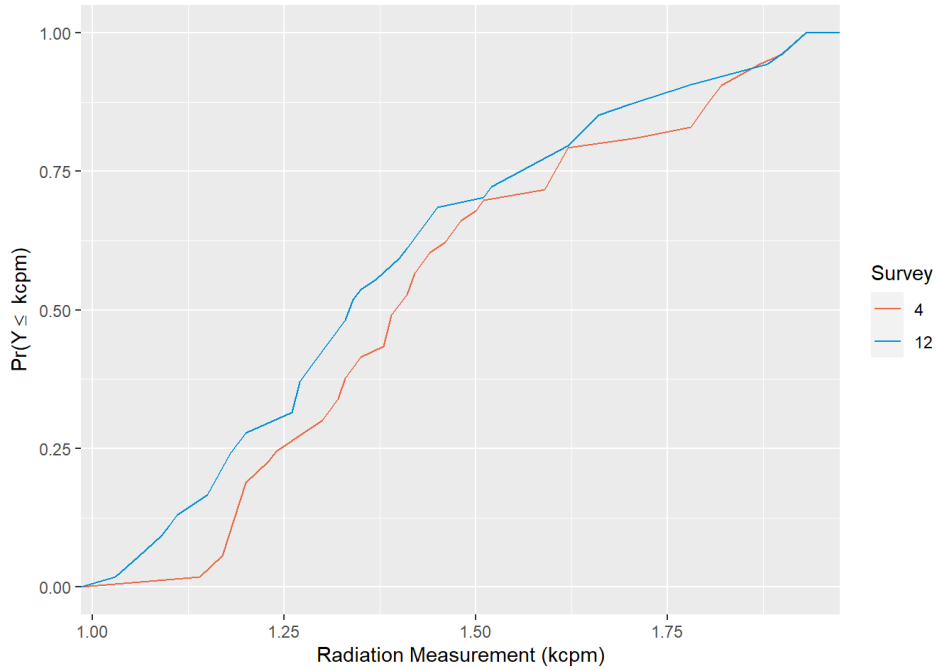

Figure E.50. eCDF Plots for Two-Sample K-S Test for Count Rate at Check Source Location 1 for Surveys 4 and 12. Count rates were not significantly different (p = 0.3247) between the human (survey 4) and UAV (survey 12).

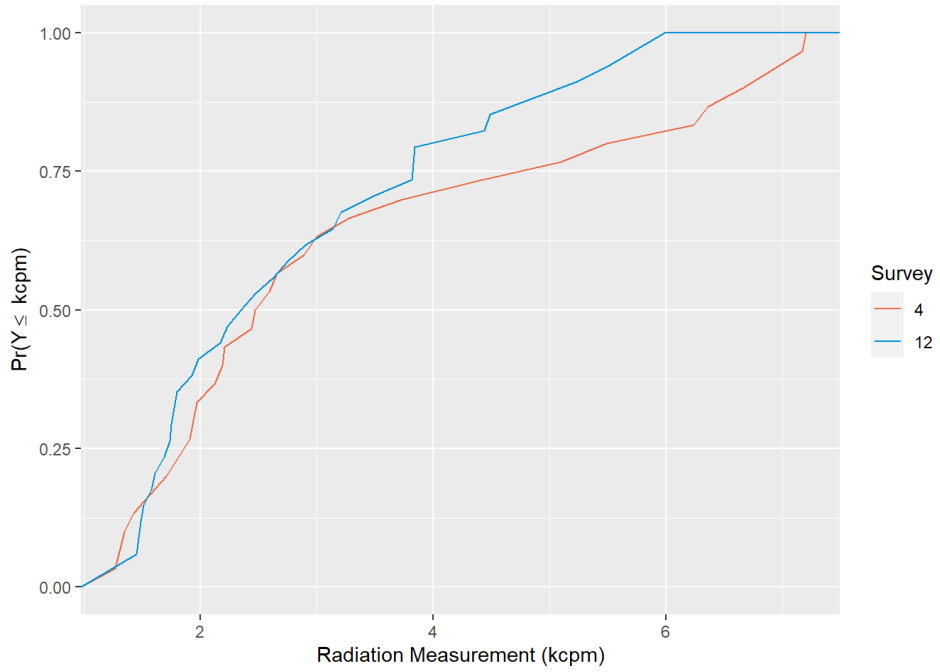

Figure E.51. eCDF Plots for Two-Sample K-S Test for Count Rate at Check Source Location 2 for Surveys 4 and 12. Count rates were not significantly different (p = 0.5467) between the human (survey 4) and UAV (survey 12).

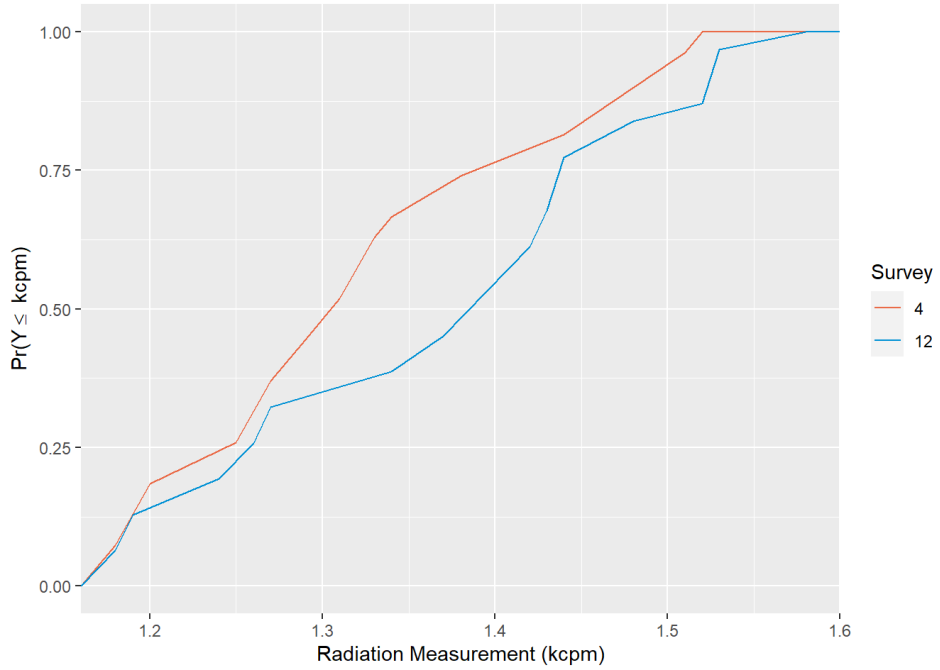

Figure E.52. eCDF Plots for Two-Sample K-S Test for Count Rate at Check Source Location 3 for surveys 4 and 12. Count rates were not significantly different (p = 0.1108) between the human (survey 4) and UAV (survey 12).

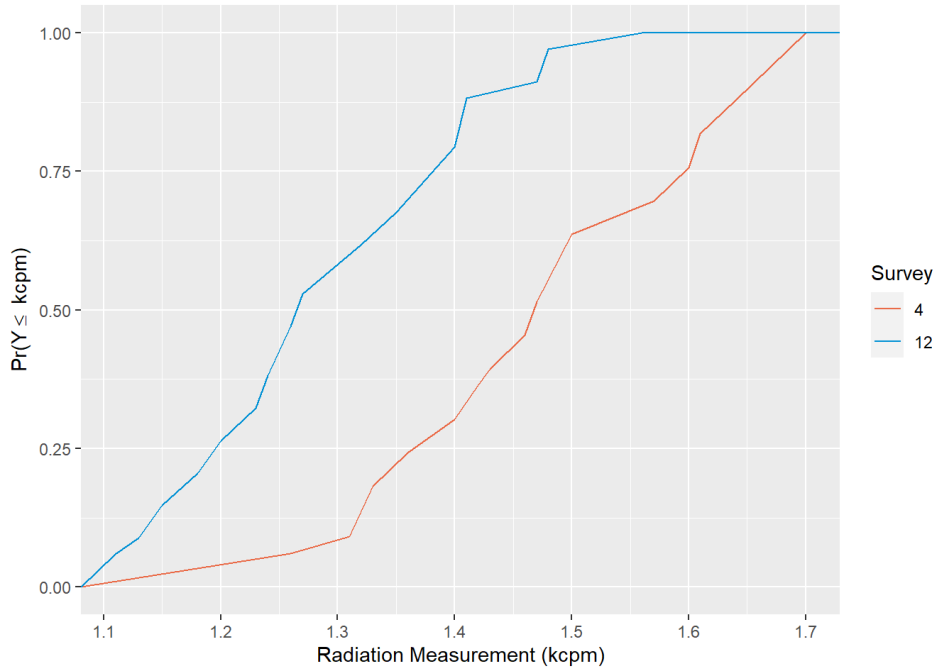

Figure E.53. eCDF Plots for Two-Sample K-S Test for Count Rate at Check Source Location 4 for Surveys 4 and 12. Count rates were significantly different (p = 0.00002626) between the human (survey 4) and UAV (survey 12).

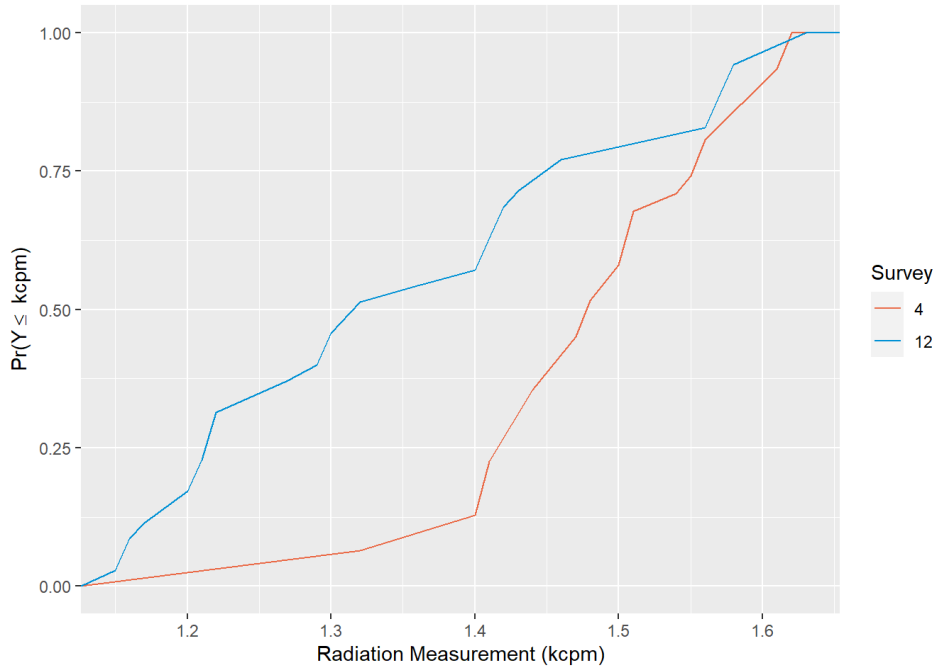

Figure E.54. eCDF Plots for Two-Sample K-S Test for Count Rate at Check Source Location 5 for Surveys 4 and 12. Count rates were significantly different (p = 0.0007832) between the human (survey 4) and UAV (survey 12).

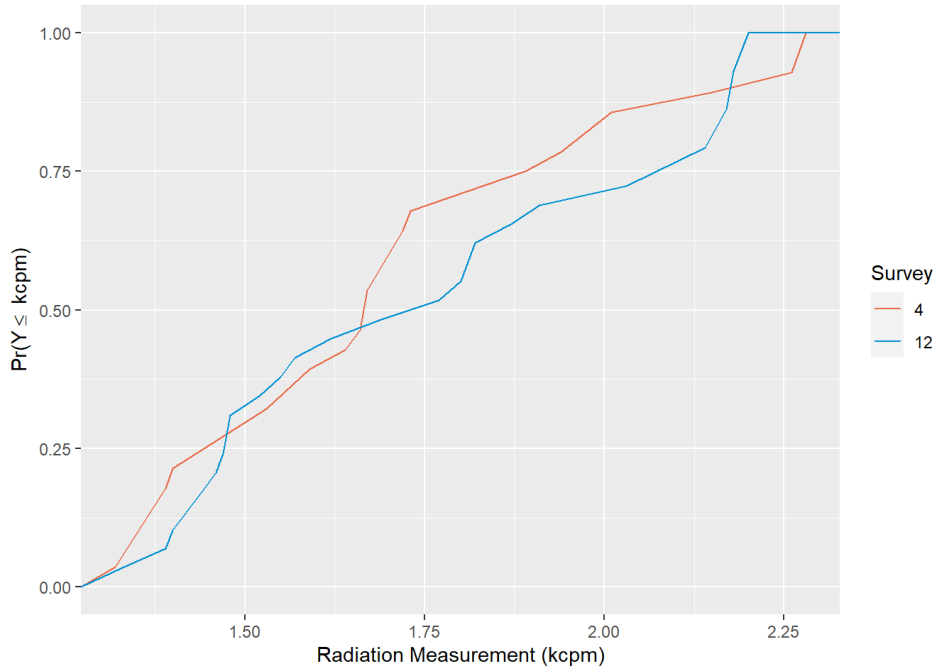

Figure E.55. eCDF Plots for Two-Sample K-S Test for Count Rate at Check Source Location 6 for Surveys 4 and 12. Count rates were not significantly different (p = 0.6456) between the human (survey 4) and UAV (survey 12).

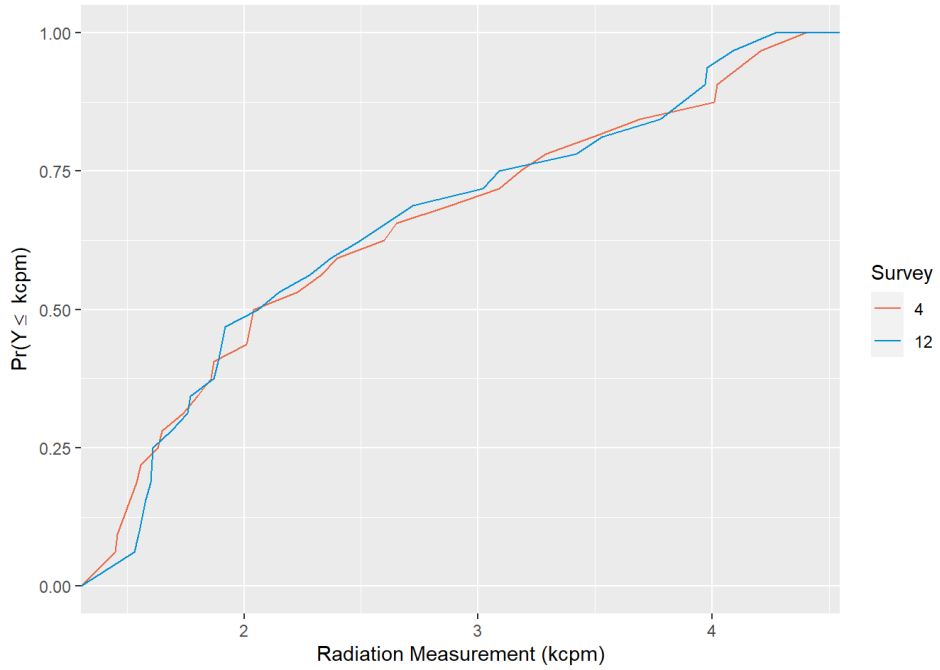

Figure E.56. eCDF Plots for Two-Sample K-S Test for Count Rate at Check Source Location 7 for Surveys 4 and 12. Count rates were not significantly different (p = 0.9639) between the human (survey 4) and UAV (survey 12).

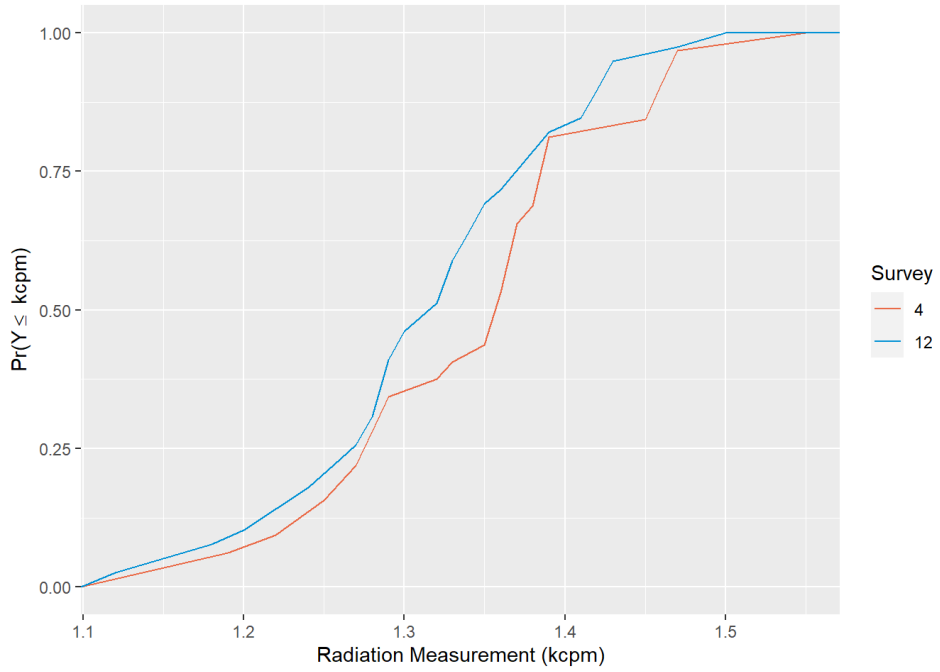

Figure E.57. eCDF Plots for Two-Sample K-S Test for Count Rate at Check Source Location 8 for Surveys 4 and 12. Count rates were not significantly different (p = 0.2038) between the human (survey 4) and UAV (survey 12).

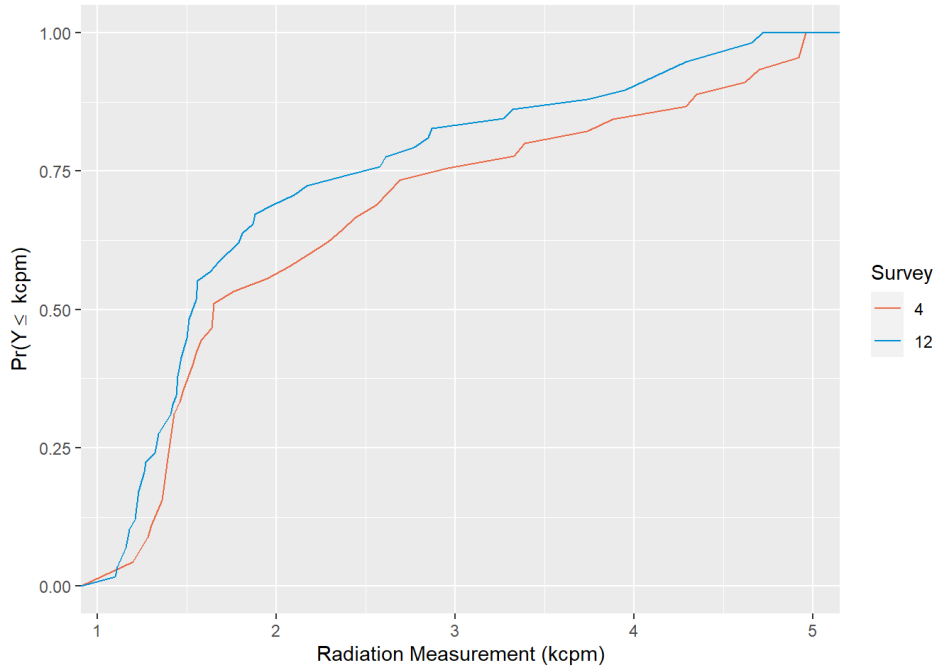

Figure E.58. eCDF Plots for Two-Sample K-S Test for Count Rate at Check Source Location 9 for Surveys 4 and 12. Count rates were not significantly different (p = 0.3865) between the human (survey 4) and UAV (survey 12).

Appendix F – List of Project Staff

Several staff members were involved in this project to design and integrate radiation detection systems with an unoccupied aerial vehicle (UAV).

Staff	Area of Expertise/Project Responsibilities
Tara O'Neil	Project Manager
Katie Wagner	Deputy Project Manager
Amoret Bunn	Principle Investigator
Emily Arredondo	Science Undergraduate Laboratory Intern (SULI)
Eric Becker	Radiation Detection Advisor
Elliot "Dutch" Dutcher	Radiation Detection Subject Matter Expert (SME)
Deb Fagan	Lead Data Analyst
Brianna Friedman	UAV SME and Lead Visual Observer (Post-Masters Research Assistant)
Harish Gadey	Lead Radiation Detection SME and Human Surveyor (Post-Doctorate Research Assistant)
Tracy Ikenberry	Decommissioning SME
Kevin Litke	PNNL 3440 Cognitive Space Manager
Steve Maheras	Decommissioning SME
Adam Mangel	UAV SME
Kameron Markham	UAV SME (Undergraduate Intern)
Jayson Martinez	UAV Pilot
Moses Obiri	Data Analyst
Kelly O'Malley	SULI
Luke Placzek	UAV SME (Undergraduate Intern)
Jon Ray	PNNL Aviation Safety Point of Contact
John "Jes" Smart	UAV SME
Josh Torgeson	Payload Specialist

Pacific Northwest National Laboratory

902 Battelle Boulevard
P.O. Box 999
Richland, WA 99354
1-888-375-PNNL (7665)

www.pnnl.gov* | *www.nrc.gov